AUTOMATIC NUMERICAL SOLUTION OF ELASTICITY PROBLEMS BY A LOCAL MESH-FREE MULTI-OBJECTIVE OPTIMIZATION FRAMEWORK

WILBER HUMBERTO VÉLEZ GÓMEZ

DOCTOR THESIS IN STRUCTURES AND CIVIL CONSTRUCTION

DEPARTMENT OF ENVIRONMENTAL AND CIVIL ENGINEERING

FACULTY OF TECHNOLOGY

UNIVERSITY OF BRASÍLIA

UNIVERSITY OF BRASÍLIA
FACULTY OF TECHNOLOGY
DEPARTMENT OF ENVIRONMENTAL AND CIVIL ENGINEERING

AUTOMATIC NUMERICAL SOLUTION OF ELASTICITY PROBLEMS BY A LOCAL MESH-FREE MULTI-OBJECTIVE OPTIMIZATION FRAMEWORK

WILBER HUMBERTO VÉLEZ GÓMEZ

SUPERVISOR: ARTUR ANTÓNIO DE ALMEIDA PORTELA, PhD.

BRASÍLIA/DF: 6th DECEMBER - 2019

UNIVERSITY OF BRASÍLIA

FACULTY OF TECHNOLOGY

DEPARTMENT OF ENVIRONMENTAL AND CIVIL ENGINEERING

NUMERICAL SOLUTION OF ELASTICITY PROBLEMS BY A LOCAL MESH-FREE MULTI-OBJECTIVE OPTIMIZATION FRAMEWORK

WILBER HUMBERTO VÉLEZ GÓMEZ

DOCTOR THESIS SUBMITTED TO THE DEPARTMENT OF ENVIRONMENTAL AND CIVIL ENGINEERING OF THE FACULTY OF TECHNOLOGY OF THE UNIVERSITY OF BRASÍLIA AS PART OF THE REQUIREMENTS REQUIRED FOR OBTAINING THE DOCTOR DEGREE IN STRUCTURES AND CIVIL CONSTRUCTION.

APPROVED BY:

_____

Prof. Artur António de Almeida Portela, PhD. (ENC-UnB)
(Supervisor)

_____

Prof. Luciano Mendez Bezerra, PhD. (ENC-UnB)
(Internal examiner)

_____

Prof. Luis Alejandro Perez Peña, PhD. (FAU-UnB)
(External examiner)

_____

Prof. Luiz Carlos Wrobel, PhD. (CIV-PUC RIO)
(External examiner)

BRASÍLIA/DF, 6th DECEMBER - 2019

FICHA CATALOGRÁFICA

GÓMEZ, WILBER HUMBERTO VÉLEZ
Numerical solution of elasticity problems by a local mesh-free multi-objective optimization method [Distrito Federal] 2019.

xx, 100p., 210 x 297 mm (ENC/FT/UnB, Doutor, Estruturas e Construção Civil, 2019). Tese de doutorado – Universidade de Brasília. Faculdade de Tecnologia.
Departamento de Engenharia Civil e Ambiental.

1.Método sem malha local	3.Optimização Multi-Objetivo
2.Teorema do Trabalho Local	4.Algoritmo genetico
I.ENC/FT/UnB	II.Título (Doutor)

REFERÊNCIA BIBLIOGRÁFICA

GÓMEZ, W. H. V. (2019). Numerical solution of elasticity problems by a local mesh-free multi-objetive optimization framework. Tese de doutorado em Estruturas e Construção Civil, Publicação E.TD-14A/19, Departamento de Engenharia Civil e Ambiental, Universidade de Brasília, Brasília, DF, 100p.

CESSÃO DE DIREITOS

AUTOR: Wilber Humberto Vélez Gómez.
TÍTULO: Numerical solution of elasticity problems by a local mesh-free multi-objetive optimization framework.

GRAU: Doutor ANO: 2019

Wilber Humberto Vélez Gómez
SHC/N CL QD. 406 BL B, Asa Norte
70.847-520. Brasília – DF – Brasil.
wilbervelez@hotmail.com

Acknowledgments

First of all I'd to thank God for helping me in this great and important project, opening paths and allowing me to meet wonderful people who made this great adventure so much better.

I thank my family, my parents Genny Gomez and Humberto Velez, my sisters Julieth and Claudia and my nephew Samuel Osorio. Also, my grandmother, uncles and cousins. Thank you all for your support and encouragement on this journey.

The CNPQ for the economic support. To the professors of the Graduate Program in Structures and Construction at the University of Brasilia (UnB) for the new learning and the opportunity to acquire new experiences. To my advisor Artur Portela for his help, dedication and motivation, my Mesh-free UnB friends Tiago, Flavio, Elvis, Fernando, Amanda and Thiago.

My gratitude to all the staff of UnB employees who contribute daily so that we can develop our research. I am very grateful to those who have done this work best for their help and friendship. Iarly, Gabriel, Jerfson, Henrique, Pedro, Luciano (lulu), Nasser, Rodolfo, Thiago, Nataniel, Gelson, Wilson, Juliana, Renan, Amir Mahdi, Matheus, Ana, Mara, Divino, Erica, Myrelle, Wilson, Nathaly, Jaime, Daniela, Pipe, Yuri, John Kennedy, and others who have supported me from before with their company Jader, Cristina, Leydi and Damaris.

To the brothers Enilton and Eliana Victor who accepted me at their home as part of the family, the Gravina family for their company and great help in this process, the and the other friends and brothers of the Assembleia de Deus of Brasilia.

But we have this wealth in vessels of earth, so that it may be seen that the power comes not from us but from God.

Troubles are round us on every side, but we are not shut in; things are hard for us, but we see a way out of them.

We are cruelly attacked, but not without hope; we are made low, but we are not without help.

II Corinthians 4: 7 - 9

AUTOMATIC NUMERICAL SOLUTION OF ELASTICITY PROBLEMS BY A LOCAL MESH-FREE MULTI-OBJECTIVE OPTIMIZATION FRAMEWORK

Author: Wilber Humberto Vélez Gómez
Supervisor: Artur António de Almeida Portela
Postgraduate Program in Structures and Civil Construction
Brasília, December 6, 2019

ABSTRACT

Project automation, whatever its nature, is a highly relevant study, as it generally speeds up the processes involved by increasing productivity. Regarding structural design automation, a common problem is the discretization used in structural element analysis by numerical methods. Thus, the automation of this process brings great advantages and increased productivity in accomplishing this task. Since the automatic use of the optimization of the numerical analysis is always fast and highly accurate, without the need for user intervention, facilitating the execution of structural design.

The concern of this work is the numerical solution of two-dimensional problems of linear elasticity, carried out with an automatic implementation of a mesh free numerical analysis, through a multi-objective optimization process. The goal of this automation strategy of analysis is to simultaneously improving the accuracy, efficiency, stability, and conditioning of the numerical solver of the mesh free method, with minimal effort of the designer. The mesh free method is based in a local formulation and therefore, uses a node-by-node process to generate the global system of equilibrium equations of a nodal discretization. Furthermore, in the local domain of integration of each node, the respective equilibrium equations are generated with a reduced numerical integration, which improves the accuracy of results.

The novelty of the thesis is the complete automation of the mesh free numerical analysis. Hence, the location coordinates and the sizes of, respectively the compact support and the local integration domain, of each node of the discretization, are automatically defined by means of a robust evolutionary multi-objective optimization process, based on genetic algorithms. Benchmark problems were analyzed to assess the accuracy and efficiency of presented techniques. The results shown in this work are in perfect agreement with those of

analytical solutions and thus, make quite reliable this strategy of automatic local mesh free numerical analysis, carried out with a multi-objective optimization process.

Keywords: *Local formulation*; *Local mesh-free method*; *Reduced numerical integration*; *Multi-objective optimization*; *Genetic algorithms*.

SOLUÇÃO NUMÉRICA AUTOMÁTICA DE PROBLEMAS DE ELASTICIDADE COM OTIMIZAÇÃO MULTI-OBJETIVO DE METODOS SEM MALHA LOCAIS

Autor: Wilber Humberto Vélez Gómez
Orientador: Artur António de Almeida Portela
Programa de Pos-graduação em Estruturas e Construção Civil
Brasília, 6 de Dezembro, 2019

RESUMO

A automação de projetos, seja ele de qualquer natureza, é um estudo altamente relevante, visto que de maneira geral ela acelera os processos envolvidos aumentando a produtividade. A respeito da automação de projetos estruturais, um problema comum é a discretização usadas na análise de elemento estruturais por via de métodos numéricos. Dessa maneira, a automação desse processo traz grandes vantagens e aumento da produtividade na realização dessa tarefa. Visto que, o uso automático da otimização da análise numérica, é sempre rápida e altamente precisa, sem a necessidade de intervenção do usuário, facilitando a execução do projeto estrutural.

O objetivo deste trabalho é a solução numérica de problemas bidimensionais de elasticidade linear. Para isso, é realizada a implementação automática de uma análise numérica sem malha, através de um processo multiobjetivo de otimização. O objetivo desta estratégia de análise de automação é melhorar simultaneamente a precisão, eficiência, estabilidade e condicionamento do solucionador numérico do método sem malha, com o mínimo esforço do projetista. O método sem malha é baseado em uma formulação local e, portanto, utiliza um processo nó por nó para gerar o sistema global de equações de equilíbrio de uma discretização nodal. Além disso, no domínio local de integração de cada nó, as respectivas equações de equilíbrio são geradas com uma integração numérica reduzida, o que melhora a precisão dos resultados.

A novidade da tese é a automação completa da análise numérica sem malha. Portanto, as coordenadas de localização e o tamanho do suporte compacto e o domínio de integração local, de cada nó da discretização, são definidos automaticamente por meio de um processo robusto e otimizado por funções multiobjetivo, baseado em algoritmos genéticos. Problemas de benchmark foram analisados para avaliar a precisão e eficiência das técnicas apresentadas. Os resultados apresentados neste trabalho estão em perfeita concordância com os das soluções analíticas e, portanto, tornam bastante confiável essa estratégia de análise numérica automática de métodos sem malha local, realizada com um processo de otimização multiobjetivo.

Palavras chave: *Formulação local*; *Método sem malha local*; *Integração númerica reduzida*; *Optimização Multi-objectivo*; *Algoritmo genetico*.

CONTENTS

LIST OF FIGURES

LIST OF SYMBOLS, NOMENCLATURES AND ABBREVIATIONS

Abbreviations

ANN Artificial Neural Networks

CAD Computer Aided Design

Dbc Displacement boundary condition

DEM Diffuse Element Method

EFG Element Free Galerkin

FEM Finite Element Method

GA Genetic Algorithms

GFEM Generalized Finite Element Method

ILMF Local Mesh-Free Method whit reduced integration

LMFM Local Mesh-Free Method

LPIM Local Point Interpolation Method

LRPIM Local Radial Point Interpolation Method

MLBIE Mesh-Free Local Boundary Integral Equation

MLPG Mesh-Free Local Petrov-Galerkin

MLS Moving least Squares

PSO Particle Swarm Optimization

PUFEM Partition of Unity Finite Element Method

RKPM Reproducing Kernel Particle Method

SA Simulated Annealing

SOS Symbiotic Organisms Search

SPH Smoothed Particle Hydrodynamics

Tbc Traction boundary condition

Greek Alphabet Symbols

(r, θ) Polar coordinates

a_q Parameter size of the local integration domain

a_s Parameter size of the compact support domain

$\boldsymbol{\varepsilon}$ Strain field

$\boldsymbol{\varepsilon}^*$ Kinematecally-admissible strain field

Γ Global domain boundary

Γ_{Qi} Interior local boundary associated with the node Q

Γ_Q Local boundary associated with the node Q

Γ_t Static boundary

Γ_u Kinematic boundary

$\|\boldsymbol{\varepsilon}\|$ Error energy norm

υ Poisson's ratio

Ω Global domain

$\Omega_{\mathbf{x}}$ Definition domain of MLS approximation of the sampling point $\mathbf{x}$

Ω_P Local compact support associated with the node $\mathbf{x}_P$

Ω_Q Local compact support associated with the node $\mathbf{x}_Q$

Ω_R Local compact support associated with the node $\mathbf{x}_R$

Φ Shape functions matrix

$\varphi(i)$ Shape function of the MLS approximation for a node i

σ Statically-admissible stress field

Latin Alphabet Symbols

$\hat{\mathbf{u}}$ Unknown nodal parameters

$\|\mathbf{u}\|$ Error displacement norm

$\mathbf{F}_Q$ Unknown nodal parameters ssociated with the field node Q

$\mathbf{K}_Q$ Nodal stiffness matrix associated with the field node Q

$\mathbf{x}_i$ Spatial coordinate of the node i

a Dimension radius

A_i Constant

b Dimension modeled section of the plate with a circular hole

B_i Constant

C Compliance

C_i Distance of the node i to the nearest neighbouring node

c_n Parameter of nodal irregularity

D Depth cantilever beam

d Distance function

E Young's modulus

$H(d)$ Heaviside step function

I Moment of inertia

k Condition Number

L Length cantilever beam

N Number of nodes

P Shear force

S Area S of local domain Ω_Q

$w(i)$ Weight function of the MLS approximation for a node i

B Matrix of linear operators

b Body forces

c Vector constant

K Vector global forces

L Matrix differential operator

$\mathbf{n}$ Matrix of the components of the unit outward normal

$\mathbf{t}$ Vector of the tration components

$\mathbf{u}$ Displacements

$\mathbf{W}_{\Gamma}$ Arbitrary weight function defined in Γ

$\mathbf{W}_{\Omega}$ Arbitrary weight function defined in Ω

$\bar{\mathbf{t}}$ Vector of the prescribed tractions

$\bar{\mathbf{u}}^*$ Strain field generated by continuos displacements

$\bar{\mathbf{u}}_k$ Specified nodal displacement component

1 - INTRODUCTION

Mesh free numerical methods achieved a remarkable progress over the past few years. The essential feature of these methods is that they perform the discretization of the problem domain and boundaries with a set of scattered field nodes that do not require any mesh for the approximation of the field variables. Historically, most of published mesh free methods rely on background cells for the integration of the weighted residual weak form over the global domain, in the process of the generation of the system of algebraic equations and therefore, they cannot be considered truly mesh free methods.

Local mesh free methods, based on weighted residual local weak forms, have been developed to avoid the background mesh generation in cells. The most popular of these methods is the Meshless Local Petrov-Galerkin (MLPG) method, that is based on the well known moving least-squares (MLS) approximation. The main feature of this method is that local weak forms are used for integration on regular-shaped local regions instead of global weak forms and therefore, the method does not require to use a global background mesh, but only a local background mesh.

The accuracy and efficiency of local mesh free methods is determined by two discretization parameters. They are, respectively the size of the local compact support domain (a_s) of each node, that is primarily linked to the accuracy of the model through the total number of nodes used to build the shape functions of the local node stiffness and, the size of the local integration domain (a_q) of each node where the work theorem is numerically integrated, that is primarily linked to the efficiency of the model.

The optimization problem of mesh free discretization parameters involves two different sorts of difficulty, which are multiple conflicting objectives and a highly complex search space. In the first case, competing goals give rise to a set of compromise solutions known as Pareto-optimal, and none of the corresponding trade-offs can be said to be better than the others, when preference information is not available. Effectively, all these trade-off solutions are optimal in the wider sense that, in the search space, no other solutions are superior to them, when all objectives are taken into consideration. In the second case, the amplitude and complexity of the search space can be too large to be solved by classic exact methods. Consequently, efficient optimization strategies that are able to address both of these difficulties are required, in an effective way. Evolutionary algorithms have several attributes that are convenient for this sort of problem which, therefore, make them more suitable than classical optimization methods.

Evolutionary approaches operate on a set of candidate solutions. Using strong simplifications,

this set is subsequently modified by basic operations based on the principles of evolution: selection, crossover and mutation. Genetic algorithms, which are a class of evolutionary methodologies, implement elitist strategy selection, which ensures that the individual with highest fitness is always copied into the next generation. Among these basic operations, the most important is crossover, because it plays a fundamental role in guiding the population toward an acceptable solution. In general, mutation is not considered to be an especially important operation and it is usually set at a very low rate, sometimes omitted, as reported by Eberhart and Shi (2007). In evolutionary algorithms, natural selection can be simulated by a stochastic selection process. Evolutionary algorithms are especially suited to multi-objective optimization because they can capture multiple Pareto-optimal solutions in a single simulation run and may exploit similarities of solutions by recombination.

This work is concerned with the implementation of the ILMF local mesh free method, presented by Oliveira et al. (2019), with automatic multi-objective optimization of the mesh free discretization parameters, using GA, for the solution automatic discretization of problems in two-dimensional linear elasticity.

1.1 - MOTIVATION

The discretization of the a_s and a_q parameters determine the accuracy and efficiency of the numerical method and therefore play a key role in the modeling strategy. Both parameters are usually arbitrarily defined and can vary depending on the local mesh free method used. The effect on accuracy and convergence of different parameters was studied by Moussaoui and Bouziane (2013) for the MLPG. The main drawback of dealing with heuristically defined discretization parameters is that their definition is not unique, and consequently cannot be easily implemented into an automatic procedure.

Therefore, an optimization attempt, using genetic algorithms (GA), was performed, on MLPG, by Baradaran and Mahmoodabadi (2009) for two dimensional steady-state heat conduction problems and by Bagheri et al. (2011) for three dimensional elastostatic problems. A similar optimization was proposed by Ebrahimnejad et al. (2015), combined with an additional adaptive refinement technique. Although these authors were successful, their attempt led to a very time consuming approach that requires an analytical solution to be performed and therefore is not efficient.

Thus, there is a clear need for an alternative modeling strategy that considers the implementation of automatic local mesh free numerical methods, with discretization parameter optimization and nodal configuration, without use of the analytical solution.

1.2 - OBJECTIVES

1.2.1 - General objective

The major objective of this thesis is the implementation of the automatic discretization of the new local mesh-free numerical method (ILMF), for solving two-dimensional problems in linear elastostatics. The formulation is derived with the work theorem, of the theory of structures, which turns out to be the weak form of a weighted-residual statement of a statically admissible stress field. The discretization is carried out locally, through a reduced numerical integration, which therefore generates the system of algebraic equations in a node by node scheme. The axiomatization of the discretization is performed in a multi-objective optimization framework of robust evolutionary methods based on genetic algorithms.

1.2.2 - Specific objectives

- Develop a local form of the work theorem, valid in an arbitrary local region of the structural body, to be applied in the formulation of a local mesh-free method, in the set of kinematically-admissible strain fields.
- Formulate and implement a local mesh-free method, with reduced integration, in the set of kinematically-admissible strain fields. Assess the virtues of both the formulation and the implementation of the reduced numerical integration, of the numerical method.
- Formulate and implement a local mesh-free method, with numerical reduced integration, for regular and irregular nodal discretization. Assess the behavior of the numerical method for both cases of the regular and irregular nodal distributions
- Formulate the multi-objective optimization process of the discretization. Define and assess the performance of the objective functions of the formulation.
- Formulate and implement the MATLAB genetic algorithms for the multi-objective optimization of both the nodal discretization and the dimensionless discretization parameters (a_s and a_q) of the local mesh-free method. Discuss the implementation.
- Compare the performance and efficiency of the automatic local mesh-free method developed, against other local mesh-free methods and available analytical solutions.

1.3 - THESIS LAYOUT

This thesis is developed in seven chapters. In chapter 1, introduction, the motivation, general and specific objectives are presented. Chapter 2, presents the literature review. Chapter 3, presents the theoretical and mathematical development of the local form of the work theorem, the local kinematic formulation for the rigid body displacement and modeling strategy. Chapter 4 presents the local mesh-free method. Chapter 5 presents the optimization of local mesh-free parameters. Chapter 6 presents some numerical results, obtained for a benchmark problem, which give evidence of the accuracy, efficiency and robustness of the strategies adopted for the automatic optimization process. Chapter 7 presents the conclusions and future ideas for research. Finally, complementary annexes used in this research are presented.

2 - LITERATURE REVIEW

One of the paths that were followed in the development of rational mechanics is based on the so-called principle of virtual works, already known, albeit in rudimentary form, by Aristotle and to which Galileo, later on, recognized generality for the first time. Connected with Lagrangian and Hamiltonian mechanics, the principle of the virtual works is a global principle linked to the concepts of work and energy. In the framework of the modern theory of structures, the virtual-work principle is no more than a particular case of the work theorem that is used as a generator of generalized models, as presented by Oliveira (1973).

The work theorem has been postulated as a unifying basis in the formulation of numerical methods in continuum mechanics, as early reported by Portela (1981) and Brebbia (1985). The work theorem establishes an energy relationship between a statically-admissible stress field and an independent kinematically-admissible strain field. The independence of these stress and strain fields is a key feature of the work theorem that allows the generation of different numerical methods. Recently, the local form of the work theorem, valid in an arbitrary local region of the structural body, was applied in the formulation of local mesh-free numerical methods, in the set of kinematically-admissible strain fields, as reported by Oliveira and Portela (2016).

2.1 - MESHFREE METHOD

Mesh-free numerical methods achieved a remarkable progress over the past few years. The essential feature of these methods is that they perform the discretization of the problem domain and boundaries with a set of scattered field nodes that do not require any mesh for the approximation of the field variables. In general, their formulation is based in the weighted-residual method presented by Finalyson (1972). In this work it is shown that the weak form, of the weighted-residual statement of a statically-admissible stress field, is obviously the work theorem of the theory of structures.

Smoothed particle hydrodynamics (SPH), presented by Lucy (1977) and Gingold and Monaghan (1977) is one of the earliest mesh-free methods applied to solve problems in astrophysics. Libersky et al. (1993) were the first to apply SPH in solid mechanics. The main drawbacks of SPH are inaccurate results near boundaries and tension instability that was first investigated by Swegle et al. (1995). SPH is based on a strong-form formulation of the weighted-residual method, with a Lagrangian description.

The collocation method is also based in the weighted-residual strong-form formulation. Typical mesh-free collocation methods were published by Sekher and Vinay (1997), Wu (1992), Zhang et al. (2001), Liu et al. (2002b), Onate et al. (1996), Lee and Yoon (2004) and Jamil and Ng (2013). Collocation methods have some attractive advantages over other mesh-free methods, as they implement a simple algorithm, with no integration required. Despite these advantages, collocation methods tend to be inaccurate and unstable, due to the ill-conditioned system equations. Onate et al. (2001) presented a stabilization technique suitable only for some particular problems.

Other mesh-free methods are based on a weighted-residual weak-form formulation. After discretization, the weak form is used to derive a system of algebraic equations, through a process of numerical integration, using background cells constructed in the domain of the problem. Research on these formulations significantly increased after the publication, by Nayroles et al. (1992), of the diffuse element method (DEM). The reproducing kernel particle method (RKPM), presented by Liu et al. (1995), and the element-free Galerkin (EFG) method, presented by Belytschko et al. (1994), were the first weak-form mesh-free methods applied in solid mechanics. In contrast to EFG and RKPM methods, with a so-called intrinsic basis, other methods with an extrinsic basis and the partition of unity concept were developed. This extrinsic basis was used in the hp-cloud method, presented by Duarte and Oden (1996). Melenk and Babuska (1996) presented the partition of unity finite element method (PUFEM) which is similar to the hp-cloud method; while PUFEM shape functions are based on Lagrange polynomials, the general form of the hp-cloud method also includes the MLS-approximation. Strouboulis et al. (2000) presented the generalized finite element method (GFEM) and pointed out that different partition of unities can be used for the usual approximation and the enrichment.

2.1.1 - Local Meshfree Method

All these weak-form mesh-free methods require the use of a background mesh for integration of the weighted-residual weak form over the global problem domain, and therefore, they are not truly mesh-free methods. To overcome this difficulty, a class of mesh-free methods based on local weighted-residual weak forms, such as the mesh-free local Petrov-Galerkin (MLPG) method presented by Atluri and Zhu (1988) to Atluri and Shen (2002), the mesh-free local boundary integral equation (MLBIE) method presented by Zhu et al. (1998), the local point interpolation method (LPIM) presented by Liu et al. (2001) and the local radial point interpolation method (LRPIM) presented by Liu et al. (2002a), have been developed. The main difference of the popular MLPG method to other global mesh-free methods, such as EFG or RKPM, is that local weak forms are used in MLPG, for integration on local domains, rather than global weak forms and consequently the method does not require the use of a background

global mesh, but only a background local grid. Note that, in contrast to the MLPG method, the new formulations presented in this work, which use generalized local weak forms, are completely free of integration, a very important feature when it comes to computational efficiency.

Local mesh-free methods exhibit excellent performance, at least in some particular applications. Despite of their performance, local mesh-free methods have not succeeded in replacing the standard displacement-assumed finite-element method (FEM), in general applications. It is well known that the global formulation of the standard FEM considers an element-by-element stiffness calculation that is assembled into the global stiffness matrix. This method of generating the final system of equations is not suitable for the analysis processing in parallel environments. Regarding this case, there is a clear advantage in using local formulations of FEM which consider a node-by-node stiffness calculation, to generate the respective rows of the global stiffness matrix. Therefore, the analysis processing can easily be parallelized, in terms of nodes, due to the independence of the nodal equations. Furthermore, the independence of the nodal equations allows, in local formulations of FEM, using of enrichment of a particular nodal stiffness matrix without increasing the nodal degrees of freedom.

2.2 - REDUCED INTEGRATION

The issue of numerical stability is quite significant when developing numerical methods. In the standard FEM, elements with a reduced number of integration points are routinely employed because they are computationally very effective and avoid locking problems of fully integrated elements. As a side effect, such reduced integrated elements are susceptible to spurious singular modes, so-called hourglass modes, which are zero-energy modes in the sense that the element deforms without an associated increase of the elastic energy. These spurious modes, generated by a reduced number of integration points, can be prevented through stabilization techniques. Zienkiewicz and Taylor (1983) and Bathe (2014) provide additional information on this concept.

The reduced integration is the main source of the numerical instability of some meshfree methods, leading to unstable hourglass deformation and zero-energy modes. This is the case of the element-free Galerkin method, see Beissel and Belytschko (1996), and the meshfree particle method, as reported by Belytschko et al. (2000). Nodal integration, in meshfree methods without stabilization, leads to instabilities due to the fact that each node is associated with a support domain, where integrations are carried out, to compute the nodal stiffness. This implies that each integration domain is associated with only one integration point, that is the node and hence, when only one integration point is considered for higher order functions, other than constant strain, the nodal integration causes instabilities. In contrast, the new integrated numerical methods presented in this work consider, in the case of the meshfree

method, a total of 4 integration points to compute the stiffness associated to each local node which, therefore, prevents the generation of spurious zero-energy modes, unlike nodal integration methods without stabilization. In order to overcome solution instabilities that are present in direct nodal integration, Taylor series expansions have been used, to serve as stabilization terms, as presented, respectively by Liu et al. (1985), for FEM, and by Liu et al. (1996) and Liu et al. (2007), for meshfree methods. While stable, the drawback of this stabilization technique is that it requires the calculation of high order derivatives.

Therefore, there is still a clear need for an alternative modeling strategy that completely avoids all the issues associated with nodal integration. To fulfill such need, this work presents a linearly integrated local meshfree numerical method.

2.3 - NUMERICAL OPTIMIZATION

Optimization is the process of adjusting the input data or characteristics of a particular system, mathematical process, or experiment, thereby seeking to find the minimum or maximum output data, whether or not is the final result Haupt and Haupt (2004). Engineering problem solving involves multi-stage decision making. The main goal of all these decisions is to minimize the effort required or maximize the desired benefit, as seen in Rao (2009). Since the required effort or desired benefit in any practical situation can be expressed as a function of certain decision variables, optimization can be defined as the process of finding the condition that determines the maximum or minimum value of a function.

Several techniques have been developed over the years to solve different types of optimization problems. Mathematical programming techniques, also known as optimal solution search methods, are good at finding the minimum of a multi-variable function under a set of constraints. Stochastic process techniques can be used to analyze problems described by a set of random variables in a probability distribution. Finally, statistical methods allow the analysis of experimental data and the construction of empirical models, thus seeking to obtain the most accurate representation of the physical situation Goldberg and Holland (1988).

There are several ways to classify optimization problems. Whether or not there are restrictions, they can be classified as restricted or unrestricted. Regarding the nature of decision variables, they can be classified into two broad categories: first as a parameter or static optimization, second as a trajectory or dynamic optimization. Classifications between linear, nonlinear, geometric, and quadratic problems can be assigned with respect to the nature of expressions for the objective function and constraints. Based on the allowed values for decision variables, they can be classified as integers or actual values. Regarding the deterministic nature of the variables, the optimization problem can be classified as deterministic or stochastic. As for the

separation between objective functions and constraints, it can be classified as separable and non-separable. Finally, depending on the number of objective functions to be minimized, the problem and optimization can be classified as mono-objective and multi-objective, as seen in Rao (2009).

Recently, algorithms emerged with great results, including Genetic Algorithm (GA) developed by Holland (1975), Simulated Annealing (SA), developed by Kirkpatrick et al. (1983), Particle Swarm Optimization (PSO), presented by Parsopoulos and Vrahatis (2002). Adaptive Symbiotic Organisms Search developed by Tejani et al. (2016). These evolutionary methods generate new points in search space by applying operators to current points and moving statistically to optimal locations in space. The great results are the result of an intelligent search in a large but finite solution space using statistical methods.

Classic optimization methods are great at finding a single solution in just one interaction, thus making them inconvenient for problem solving with multiple objective functions. In contrast, as demonstrated by Deb (2001), evolutionary algorithms can find many optimal solutions, thanks to their sample space search process, particularly the mutation and the crossover. Thus, these methods are ideal for applications related to multi-objective problems, such as problems related to the present research.

3 - STRUCTURAL MODELING

Consider the domain Ω of a body with boundary Γ subdivided in Γ_u and Γ_t, with $\Gamma = \Gamma_u \cup \Gamma_t$, as Figure 3.1 represents.

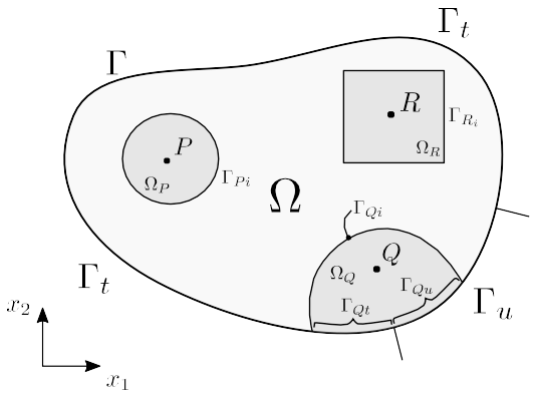

Figure 3.1 – Representation of the body's domain Ω, with boundary $\Gamma = \Gamma_u \cup \Gamma_t$; the work theorem is defined in an arbitrary domain $\Omega_Q \in \Omega \cup \Gamma$, assigned to a reference point $Q \in \Omega_Q$, with boundary $\Gamma_Q = \Gamma_{Qi} \cup \Gamma_{Qt} \cup \Gamma_{Qu}$, in which Γ_{Qi} is the interior local boundary, and Γ_{Qt} and Γ_{Qu} are local boundaries that share the global boundaries, respectively the static boundary Γ_t and the kinematic boundary Γ_u; points P and R, have arbitrary local domains, respectively Ω_P and Ω_R.

The fundamental boundary value problem of elasticity aims to find, in Ω, the distribution of stresses $\boldsymbol{\sigma}$, strains $\boldsymbol{\varepsilon}$ and displacements $\mathbf{u}$, when it has displacements $\bar{\mathbf{u}}$, constrained on Γ_u, and is under the action of an external system of distributed surface and body forces with densities represented, respectively by $\bar{\mathbf{t}}$, on Γ_t and $\mathbf{b}$, in Ω.

The solution of the posed problem, simultaneously satisfying kinematic admissibility of the strains and static admissibility of the stresses, is thus a fully admissible elastic field. Kirchhoff's theorem, see Kirchhoff (1859), on the uniqueness of solutions of the elasticity boundary value problem shows that this solution is unique, assuming that it exists. The general work theorem will be used to solve the posed problem.

In the body's domain, loaded by a system of external forces in the conditions already referred, consider a statically admissible stress field $\boldsymbol{\sigma}$, which therefore satisfies

$$\mathbf{L}^T\boldsymbol{\sigma} + \mathbf{b} = \mathbf{o}, \tag{3.1}$$

in Ω, with boundary conditions

$$\mathbf{t} = \mathbf{n}\,\boldsymbol{\sigma} = \bar{\mathbf{t}}, \tag{3.2}$$

specified on Γ_t; $\mathbf{L}$ is a matrix differential operator; $\mathbf{t}$ denotes traction components; $\bar{\mathbf{t}}$ denotes prescribed tractions and $\mathbf{n}$ is the matrix of the components of the unit normal to the boundary outwardly directed.

3.1 - LOCAL DOMAIN

In the body, consider an arbitrary local domain $\Omega_Q \in \Omega \cup \Gamma$, assigned to a reference point $Q \in \Omega_Q$, with boundary $\Gamma_Q = \Gamma_{Qi} \cup \Gamma_{Qt} \cup \Gamma_{Qu}$, in which Γ_{Qi} is the interior local boundary, with local boundaries Γ_{Qt} and Γ_{Qu} sharing the global boundaries, respectively the static boundary Γ_t and the kinematic boundary Γ_u, as Figure 3.1 represents. The work theorem will be derived for this arbitrary local domain Ω_Q. Due to its arbitrariness, this local domain $\Omega_Q \cup \Gamma_Q \in \Omega \cup \Gamma$ can be overlapping with other similar sub-domains that can be defined in the body.

3.2 - THE WORK THEOREM

The work theorem, presented in Oliveira and Portela (2016), establishes an energy relationship, in an arbitrary local domain $\Omega_Q \in \Omega$, between two independent elastic fields that can be defined in the body which are, respectively a statically admissible stress field $\boldsymbol{\sigma}$ that satisfies equilibrium with a system of external forces, and a kinematically admissible strain field $\boldsymbol{\varepsilon}^*$ that satisfies compatibility with a set of constrained displacements. Expressed as an integral form, defined in the domain $\Omega_Q \cup \Gamma_Q$, the theorem of work can be written in a compact way, simply as

$$\int_{\Gamma_Q} \mathbf{t}^T \mathbf{u}^*\, d\Gamma + \int_{\Omega_Q} \mathbf{b}^T \mathbf{u}^*\, d\Omega = \int_{\Omega_Q} \boldsymbol{\sigma}^T \boldsymbol{\varepsilon}^*\, d\Omega, \tag{3.3}$$

in which no constitutive relation links the stress $\boldsymbol{\sigma}$ and the strain $\boldsymbol{\varepsilon}^*$ and therefore, they do not depend on each other, as Figure 3.2 schematically represents.

The stress $\boldsymbol{\sigma}$, a statically admissible field, can be any one that is in equilibrium with the system of external forces, therefore satisfying equations (3.1) and (3.2); it is not necessarily the stress that the system of external forces actually introduces in the body.

The strain $\boldsymbol{\varepsilon}^*$, a kinematically admissible field, can be any one, generated by continuous displacements $\mathbf{u}^*$ with small derivatives, compatible with an arbitrary set of constraints specified on the kinematic boundary; it is not necessarily the strain actually settled in the body.

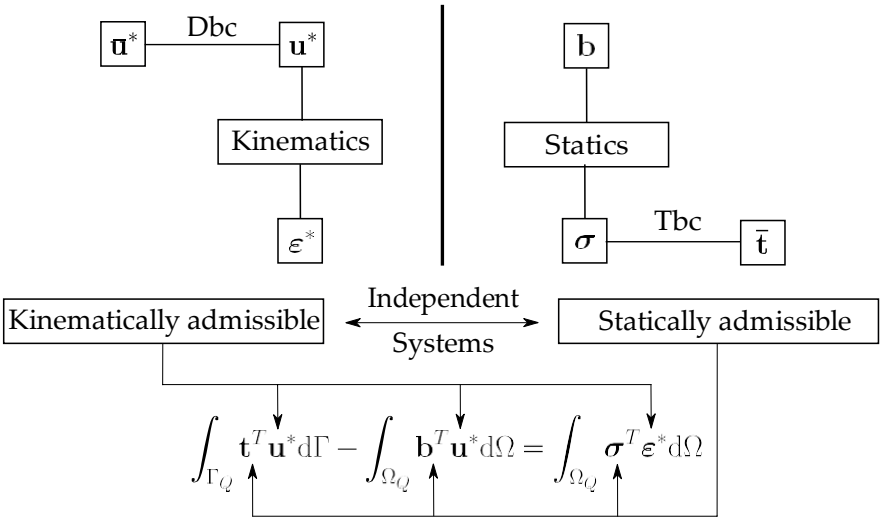

Figure 3.2 – Schematic representation of the work theorem, an energy relationship, valid in an arbitrary local domain $\Omega_Q \in \Omega \cup \Gamma$, with boundary Γ_Q, between any two independent fields, in which one of them, the stress field $\boldsymbol{\sigma}$, is required to satisfy equilibrium with a system of external forces $\mathbf{b}$ and $\bar{\mathbf{t}}$, while the other, the strain field $\boldsymbol{\varepsilon}^*$, is required to satisfy compatibility with a set of constrained displacements $\bar{\mathbf{u}}^*$, in the domain $\Omega \cup \Gamma$ of the body.

Finally, the local domain $\Omega_Q \cup \Gamma_Q$ is an arbitrary sub-domain of the body, associated with the reference point Q, as represented in Figure 3.1, where the independent fields $\boldsymbol{\sigma}$ and $\boldsymbol{\varepsilon}^*$ are defined.

3.3 - KINEMATIC FORMULATIONS

In order to use the work theorem, as the starting point in the formulation of numerical methods, it is necessary to specify one of the two independent fields that can be defined in the body, in accordance with some particular convenience of the numerical method formulation.

Kinematic formulations consider a particular specification of the strain field $\boldsymbol{\varepsilon}^*$, leading thus to an equation of mechanical equilibrium that is used in numerical models, to generate the respective stiffness matrix. A simple case of a kinematic formulation, based on a strain field generated by a rigid-body displacement.

3.3.1 - Rigid-body displacement formulation

Bearing in mind the key feature of the work theorem, that is the complete independence of the admissible fields, $\boldsymbol{\sigma}$ and $\boldsymbol{\varepsilon}^*$, the strain field is defined to simplify the formulation. Hence, the simplest and obvious choice is to use a strain field generated by a rigid-body displacement that can be defined as

$$\mathbf{u}^*(\mathbf{x}) = \mathbf{c}, \tag{3.4}$$

in which $\mathbf{c}$ is a constant vector that conveniently generates null strains

$$\boldsymbol{\varepsilon}^*(\mathbf{x}) = \mathbf{o}. \tag{3.5}$$

The great virtue of this formulation is the simplicity used in the generation of the strain field; in addition, this formulation leads to a simple form of equilibrium equations that, in the absence of body forces, has no domain terms.

3.3.2 - Mechanical equilibrium

When the rigid-body displacement formulation is considered, the work theorem, equation (3.3), simply leads to the equation

$$\int_{\Gamma_Q - \Gamma_{Qt}} \mathbf{t}\, d\Gamma + \int_{\Gamma_{Qt}} \bar{\mathbf{t}}\, d\Gamma + \int_{\Omega_Q} \mathbf{b}\, d\Omega = \mathbf{o} \tag{3.6}$$

which states an integral form of mechanical equilibrium, of tractions and body forces, in the domain Ω_Q. Obviously, this equation expresses the local version of the Euler-Cauchy stress principle.

Local equilibrium equation (3.6), is used to generate the stiffness matrix associated to the local node.

3.4 - MODELING STRATEGY

The formulation of numerical methods can be based on the work theorem, along with a proper and convenient kinematic formulation, in order to derive the equilibrium equations that are used to generate the stiffness matrix of each numerical model. This modeling strategy is adopted to solve the actual elastic problem.

3.4.1 - Defining the strain field

The work theorem is kinematically formulated through the specification of an appropriate strain field $\boldsymbol{\varepsilon}^*$. This thesis considers the arbitrary rigid-body displacement, to kinematically formulate the work theorem, thus leading to the equilibrium equation (3.6).

3.4.2 - Defining the stress field

This stage of the modeling strategy regards the definition of the statically admissible stress field, in the equilibrium equation (3.6). The stress field $\boldsymbol{\sigma}$, required to satisfy equilibrium with a system of external forces, is assumed as the state of stress that actually settles in the body, loaded by the actual system of distributed surface and body forces, with the actual displacement constraints. This key assumption is schematically represented in Figure 3.3.

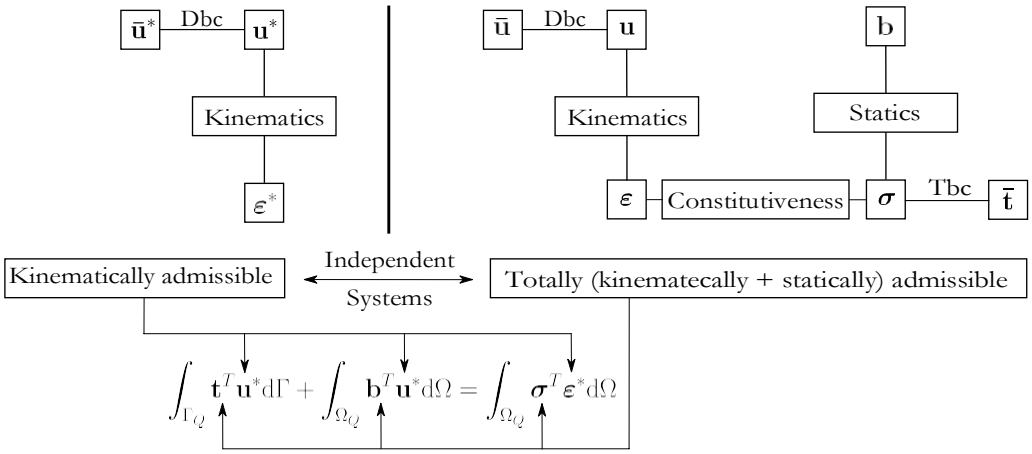

Figure 3.3 – Modeling strategy of kinematic models of the work theorem. After choosing the kinematically admissible strain field, the strategy considers that the statically admissible stress field is always assumed as the stress field of the unique elastic field that actually settles in the body which satisfies full admissibility. Dbc and Tbc stands for Displacement boundary condition and Traction boundary condition respectively.

Recall that the elastic field that settles in the body is the unique fully admissible elastic field satisfying the given problem. Therefore, besides satisfying equilibrium, through equations (3.1) and (3.2), or through equation (3.6), generated by the work theorem, this unique fully admissible field also must satisfy compatibility, defined as

$$\boldsymbol{\varepsilon} = \mathbf{L}\,\mathbf{u}, \tag{3.7}$$

in Ω, with boundary conditions

$$\mathbf{u} = \bar{\mathbf{u}}, \tag{3.8}$$

on Γ_u, in which continuous displacements are assumed with small derivatives, leading to geometrical linearity of the strain field. Hence, equation (3.8), which specifies the constraints of the actual displacements, must be applied in any numerical model, in order to allow for a unique solution of the problem.

This thesis considers the absence of body forces in the formulation of the local mesh free method.

4 - LOCAL MESH-FREE NUMERICAL METHOD

The essential feature of mesh free methods is that they perform the discretization of the problem only with a set of scattered nodes, without using any mesh for the approximation of the variables. The local mesh free method, presented in this paper, is based on the widely used approximation of the moving least-squares (MLS). The basic MLS terminology, introduced by Atluri and Zhu (2000), is presented here, along with a summary of the essential features of the MLS approximation, used in this work.

Each node of the mesh free discretization is associated with its local domain, as schematically represented in Figure 4.1. In general, this local domain is a circular or rectangular region,

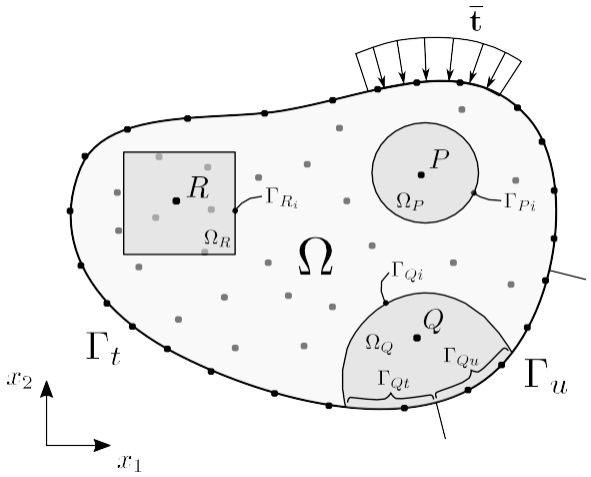

Figure 4.1 – Mesh free discretization of the domain Ω and boundary $\Gamma = \Gamma_u \cup \Gamma_t$; reference nodes P, Q and R have associated local domains Ω_P, Ω_Q and Ω_R; the local domain Ω_Q, assigned to the node Q, where the work theorem is defined, has boundary $\Gamma_Q = \Gamma_{Qi} \cup \Gamma_{Qt} \cup \Gamma_{Qu}$, in which Γ_{Qi} is the interior local boundary and $\Gamma_{Qt} \in \Gamma_t$ and $\Gamma_{Qu} \in \Gamma_u$.

centered at the respective node, where the rigid-body displacement formulation of the work theorem is defined as a local form, of mechanical equilibrium.

The local character of the MLS approximation is a consequence of the compact support of each node, where the respective MLS shape functions are defined. Circular or rectangular local compact supports, centered at each node, can be used. The size of the compact support, in turn, sets out, in a neighborhood of a sampling point, the respective domain of definition of the MLS approximation at this point, as schematically represented in Figure 4.2. The domain of definition contains all the nodes whose MLS shape functions do not vanish at this sampling point.

The MLS approximation has local character which is a direct consequence of the compact

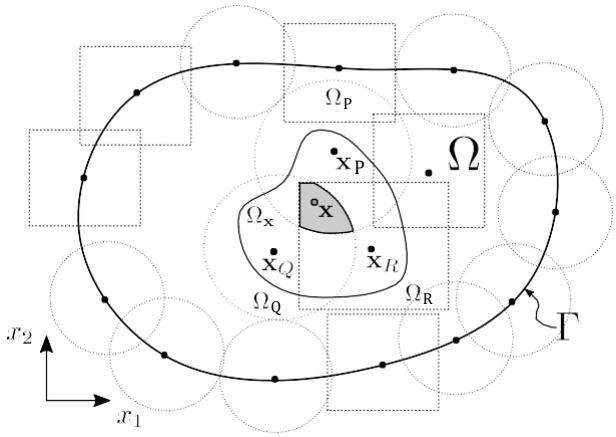

Figure 4.2 – Schematic representation of a mesh-free discretization of the global domain Ω and boundary Γ, with a distribution of nodes; Ω_P , Ω_Q and Ω_R represent the local compact supports of the corresponding nodes $\mathbf{x}_P$, $\mathbf{x}_Q$ and $\mathbf{x}_R$; $\Omega_\mathbf{x}$ is the domain of definition, of the MLS approximation of the sampling point $\mathbf{x}$, which is the set of nodes, in this case $\mathbf{x}_P$, $\mathbf{x}_Q$ and $\mathbf{x}_R$, whose compact support contains this sampling point.

support of each node, where the respective MLS shape functions are defined. Local compact supports, with circular or rectangular shape, centered at each node, can be used. The size of the compact support determines, in a neighborhood of a sampling point, the respective MLS domain of definition at this point, as schematically represented in Figure 4.2.

All the nodes, whose MLS shape functions do not vanish at this sampling point, are contained in the domain of definition. Therefore, the union of the MLS domains of definition of all points in the local domain of each node, defines the domain of influence of the node. Based in the domain of influence of each node, local mesh free formulations use a node-by-node stiffness calculation to generate, the respective rows of the global stiffness matrix of the node. The MLS formulation is presented in the annex.

In the absence of body forces, the local form of the work theorem with the rigid-body displacement formulation, equation (3.6), can be written simply as

$$\int_{\Gamma_Q - \Gamma_{Qt}} \mathbf{t}\, d\Gamma = -\int_{\Gamma_{Qt}} \bar{\mathbf{t}}\, d\Gamma \tag{4.1}$$

which represents mechanical equilibrium of the boundary tractions of the local domain Ω_Q, associated with the field node $Q \in \Omega_Q$. Note that, although derived in an entirely different way that does not make use the work theorem, this equation corresponds to the model MLPG5 presented by Atluri and Shen (2002).

For a mesh-free discretization of the body, the local mesh-free method, symbolically referred to as LMFM, is used to compute the respective system of algebraic equations, in a node-by-node process, throughout integration of the corresponding local form (4.1) assigned to each node,

with rectangular or circular local domains and numerical quadrature applied on each side, or quadrant, of the local domain, as schematically represented in Figure 4.3.

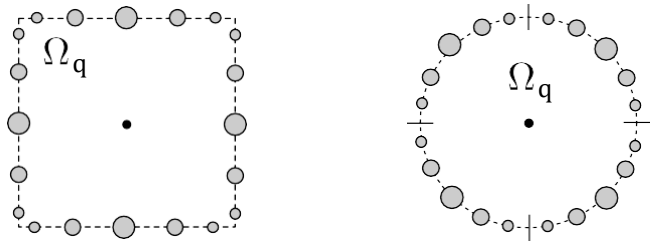

(a) Rectangular domain. (b) Circular domain.

Figure 4.3 – Schematic representation of numerical-quadrature points, on each side, or quadrant, of local domains, for the computation of the local form of the work theorem, with the rigid-body displacement formulation.

Discretization of the local form (4.1) is carried out with the MLS approximation, equations (A.15) to (A.19), in terms of the unknown nodal parameters $\hat{\mathbf{u}}$, thus leading to the system of two linear equations

$$\int_{\Gamma_Q - \Gamma_{Qt}} \mathbf{n}\,\mathbf{D}\,\mathbf{B}\,\hat{\mathbf{u}}\,\mathrm{d}\Gamma = -\int_{\Gamma_{Qt}} \bar{\mathbf{t}}\,\mathrm{d}\Gamma \tag{4.2}$$

that can be written as

$$\mathbf{K}_Q\,\hat{\mathbf{u}} = \mathbf{F}_Q, \tag{4.3}$$

in which $\mathbf{K}_Q$, the nodal stiffness matrix associated with the field node Q, is a $2 \times 2n$ matrix (n is the number of nodes included in the domain of influence of the reference node Q that is the union of the MLS domains of definition of all integration points in the local domain Ω_Q) given by

$$\mathbf{K}_Q = \int_{\Gamma_Q - \Gamma_{Qt}} \mathbf{n}\,\mathbf{D}\,\mathbf{B}\,\mathrm{d}\Gamma \tag{4.4}$$

and $\mathbf{F}_Q$, is the force vector associated with the field node Q, given by

$$\mathbf{F}_Q = -\int_{\Gamma_{Qt}} \bar{\mathbf{t}}\,\mathrm{d}\Gamma. \tag{4.5}$$

Consider that the problem has a total of N field nodes Q, each one associated with the respective local domain Ω_Q. Assembling equations (4.3) for all M interior and static-boundary field nodes leads to the global system of $2M \times 2N$ equations

$$\mathbf{K}\,\hat{\mathbf{u}} = \mathbf{F}. \tag{4.6}$$

Finally, the remaining equations are obtained from the $N - M$ boundary field nodes on the

kinematic boundary. For a field node on the kinematic boundary, a direct interpolation method, first presented by Liu and Yan (2000), is used to impose the boundary condition as

$$u_k^h(\mathbf{x}_j) = \sum_{i=1} \varphi_i(\mathbf{x}_j)\hat{u}_{ik} = \bar{\mathbf{u}}_k, \tag{4.7}$$

or, in matrix form as

$$\mathbf{u}_k = \mathbf{\Phi}_k\,\hat{\mathbf{u}} = \bar{\mathbf{u}}_k, \tag{4.8}$$

with $k = 1, 2$, where $\bar{\mathbf{u}}_k$ is the specified nodal displacement component. Equations (4.8) are directly assembled into the global system of equations (4.6).

It is quite important to note that, the line integration carried out only on the boundary of the local domain, in equation (4.1), to build the respective nodal stiffness matrix of LMFM, is computationally much more efficient than the other mesh-free methods that use domain integration, as is the case of the EFG method, presented by Belytschko et al. (1994), or the MLPG1, MLPG3 and MLPG6 methods presented by Atluri and Shen (2002). The higher efficiency of LMFM is clearly evident in numerical results.

4.1 - REDUCED INTEGRATION FORMULATION

General mesh free numerical methods can be effectively formulated through a reduced integration of the equilibrium equation (4.1). In the simplest case, linear variation of tractions is assumed on each boundary of the local domain, which leads to a point-wise discrete form that improves the computational efficiency. In addition, as numerical results clearly demonstrate, there is also an improvement of the accuracy.

For a linear variation of tractions, along each boundary segment of the local domain, the local form of equilibrium (4.1), can be exactly evaluated with 1 quadrature point, centered on each segment, thus leading to

$$\frac{L_i}{n_i} \sum_{j=1} \mathbf{t}_{\mathbf{x}_j} = -\frac{L_t}{n_t} \sum_{k=1} \bar{\mathbf{t}}_{\mathbf{x}_k}, \tag{4.9}$$

in which n_i and n_t denote the total number of collocation points defined on, respectively the interior local boundary $\Gamma_{Qi} = \Gamma_Q - \Gamma_{Qt} - \Gamma_{Qu}$, with length L_i, and the local static boundary Γ_{Qt}, with length L_t. This equation, completely free of integration, represents mechanical equilibrium of the boundary tractions, evaluated at a set of collocation points, on the boundary of the local domain Ω_Q, associated with the field node $Q \in \Omega_Q$.

For a given mesh free nodal distribution, the local mesh free method with linear reduced integration, symbolically referred to as ILMF, an acronym that stands for Integrated Local

Mesh Free method, is used to compute the stiffness matrix, in a node-by-node process, throughout traction evaluation at each central point of boundary segments, through equation (4.9) assigned to each node, with rectangular or circular local domains, schematically represented in Figure 4.4.

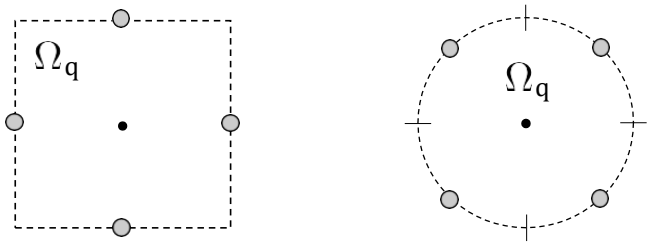

(a) Rectangular domain. (b) Circular domain.

Figure 4.4 – Schematic representation of rectangular and circular local domains, with 1 collocation point on each side, or quadrant, of the local domain, for the computation of the generalized local form of the work theorem, with the rigid-body displacement formulation.

Discretization of the generalized local form (4.9) is carried out with the MLS approximation, equations (A.15) to (A.19), in terms of the unknown nodal parameters $\hat{\mathbf{u}}$, thus leading to the system of two linear algebraic equations

$$\frac{L_i}{n_i}\sum_{j=1}^{n_i} \mathbf{n}_{\mathbf{x}_j}\mathbf{B}_{\mathbf{x}_j}\,\hat{\mathbf{u}} = -\frac{L_t}{n_t}\sum_{k=1}^{n_t} \mathbf{t}_{\mathbf{x}_k} \tag{4.10}$$

that can be written as

$$\mathbf{K}_Q\,\hat{\mathbf{u}} = \mathbf{F}_Q, \tag{4.11}$$

in which $\mathbf{K}_Q$, the nodal stiffness matrix associated with the field node Q, is a $2 \times 2n$ matrix (n is the number of nodes included in the domain of influence of the reference node Q that is the union of the MLS domains of definition of all collocation points in the local domain Ω_Q) given by

$$\mathbf{K}_Q = \frac{L_i}{n_i}\sum_{j=1}^{n_i} \mathbf{n}_{\mathbf{x}_j}\mathbf{B}_{\mathbf{x}_j} \tag{4.12}$$

and $\mathbf{F}_Q$ is the respective force vector given by

$$\mathbf{F}_Q = -\frac{L_t}{n_t}\sum_{k=1}^{n_t} \mathbf{t}_{\mathbf{x}_k}. \tag{4.13}$$

Consider that the problem has a total of N field nodes Q, each one associated with the respective local domain Ω_Q. Assembling equations equations (4.11) for all M interior and static-boundary field nodes leads to the global system of $2M \times 2N$ equations

$$\mathbf{K}\,\hat{\mathbf{u}} = \mathbf{F}. \tag{4.14}$$

Finally, the remaining equations are obtained from the $N - M$ boundary field nodes on the kinematic boundary. For a field node on the kinematic boundary, a direct interpolation method is used to impose the kinematic boundary condition as

$$\mathbf{u}_k = \mathbf{\Phi}_k \hat{\mathbf{u}} = \bar{\mathbf{u}}_k, \tag{4.15}$$

with $k = 1, 2$, where $\bar{\mathbf{u}}_k$ is the specified nodal displacement component. Equations (4.15) are directly assembled into the global system of equations (4.14).

Although ILMF generates a symmetric and banded global system of equations, these features are not addressed in the research since, as a local mesh free method, ILMF generates the global system of equations in a node-by-node process, through equations (4.11) to (4.14). This generation process is different from the one used in the standard FEM which considers an element-by-element process to generate the global stiffness matrix.

It can be easily anticipated high computational efficiency of the ILMF model, with very accurate results. As a matter of fact, the nodal stiffness matrix is effectively computed, in equations (4.12), with only 4 integration points (1 point per segment of the local domain), which basically implies a very short processing time to run the analysis. In addition, the reduced integration leads to high accuracy of the results. The reduced integration of this linearly integrated formulation plays a fundamental role in the behavior of the ILMF model, since it implies a reduction of the stiffness, corresponding to an increase of the strain energy which, in turn, leads to an increase of the solution accuracy and, which is most important, presents no instabilities. Note that this high accuracy, generated by the reduced integration, has been already used in the standard FEM to prevent locking.

4.2 - PARAMETERS OF LOCAL MESH-FREE METHOD

For each node of a mesh-free discretization, the size r_{Ω_s} of the compact support Ω_s, where the MLS shape functions are defined, and the size r_{Ω_q} of the local domain Ω_q, where the work theorem is defined, are very important parameters that can affect the performance of the solution of a numerical application and therefore, they must be addressed here. For a generic node i, of a mesh-free discretization, these parameters can be defined, respectively as

$$r_{\Omega_s} = a_s \, c_i \tag{4.16}$$

and

$$r_{\Omega_q} = a_q \, c_i, \tag{4.17}$$

in which c_i represents the distance of the node i, to the nearest neighbouring node, while α_s and α_q are constant parameters that must be defined in any application.

To improve the model accuracy, the nodal distribution requires a proper refinement of r_{Ω_s} and r_{Ω_q}, through the specification of parameters α_s and α_q defined in equations, respectively (4.16) and (4.17). In general, the discretization parameters are considered, respectively as $\alpha_s > 1.0$ and $\alpha_q < 1.0$, for regular node distributions.

The discretization parameters, α_s and α_q, play different roles in the local mesh free numerical method, which can be defined as follows:

- The size of the influence domain of each node, is directly determined by the compact supports. This influence domain completely defines the total number of nodes required to build the respective nodal shape functions, in order to perform the MLS approximation of variables. Therefore, the parameter α_s is primarily linked to the accuracy of the mesh free method.
- The local domain of integration of each node is used to build the stiffness matrix of each node and, therefore it must be within the solution domain, without intersecting the boundary of the body. Therefore, the parameter α_q is primarily linked to the efficiency of the method.

Historically, the discretization parameters, α_s and α_q, have been heuristically defined and their respective value depends mostly on the MLS approximation and on the nodal distribution considered. On the other hand, the ILMF model can obtain automatically the appropriate values of these parameters, α_s and α_q, through a multi-objective optimization process, carried out with genetic algorithms.

5 - OPTIMIZATION WHIT GENETIC ALGORITHMS

Basic concepts, terminology of optimization, feasibility, and Pareto optimality are formally defined in optimization literature presented by Sawaragi et al. (1985), Hwang and Masud (1979), Steuer (1986) and Ringuest (1992). This section presents some topics required by the optimization of the discretization. The complete full automated routine of GA implementation (in MATLAB 2015a) for local mesh free methodsis presented in Appendix C, for the sake of completeness.

5.1 - MULTI-OBJECTIVE OPTIMIZATION PROBLEM

In this work, the multi-objective optimization problem (MOP) includes a set of n decision variables, a set of k objective functions, and a set of m constraints. Objective functions and constraints are functions of the decision variables, in this case a_s. The optimization goal is to

$$\begin{aligned} &\text{minimize} && \mathbf{y} = \mathbf{f}(\boldsymbol{a_s}) = (f_1(\boldsymbol{a_s}), f_2(\boldsymbol{a_s}), \ldots, f_k(\boldsymbol{a_s})) \\ &\text{subject to} && \mathbf{e}(\boldsymbol{a_s}) = (e_1(\boldsymbol{a_s}), e_2(\boldsymbol{a_s}), \ldots, e_m(\boldsymbol{a_s})) \leq \mathbf{o} \\ &\text{where} && \boldsymbol{a_s} = (a_{s1}, a_{s2}, \ldots, a_{sn}) \in \boldsymbol{a} \\ & && \mathbf{y} = (y_1, y_2, \ldots, y_k) \in \mathbf{Y}, \end{aligned} \tag{5.1}$$

in which $\boldsymbol{a_s}$ is the decision vector, $\mathbf{y}$ is the objective vector, $\boldsymbol{a_s}$ represents the decision space and $\mathbf{Y}$ represents the objective space; the constraints $\mathbf{e}(\boldsymbol{a_s}) \leq \mathbf{o}$ determine the set of feasible solutions.

5.1.1 - Feasible Set

The feasible set $\boldsymbol{a}_f$ is defined as the set of decision vectors $\boldsymbol{a_s}$ that satisfy the constraints $\mathbf{e}(\boldsymbol{a_s})$ that is:

$$\boldsymbol{a}_f = \{\boldsymbol{a_s} \in \boldsymbol{a} \mid \mathbf{e}(\boldsymbol{a_s}) \leq \mathbf{o}\}. \tag{5.2}$$

The image of $\boldsymbol{a}_f$, that is the feasible region in the objective space, is denoted as $\mathbf{Y}_f = \mathbf{f}(\boldsymbol{a}_f) = \cup_{\boldsymbol{a_s} \in \boldsymbol{a}_f} \{\mathbf{f}(\boldsymbol{a_s})\}$.

The difficulty in MOP is the common situation when the individual optima, corresponding to different objective functions, are sufficiently different. Then, the objectives are conflicting and cannot be optimized simultaneously. Instead, a satisfactory trade-off has to be found, which

emphasizes that a new notion of optimality is required for MOP. When several objectives are involved, in general $\boldsymbol{\Omega}_f$ is not totally ordered, but only partially ordered, as represented in Figure 5.1a.

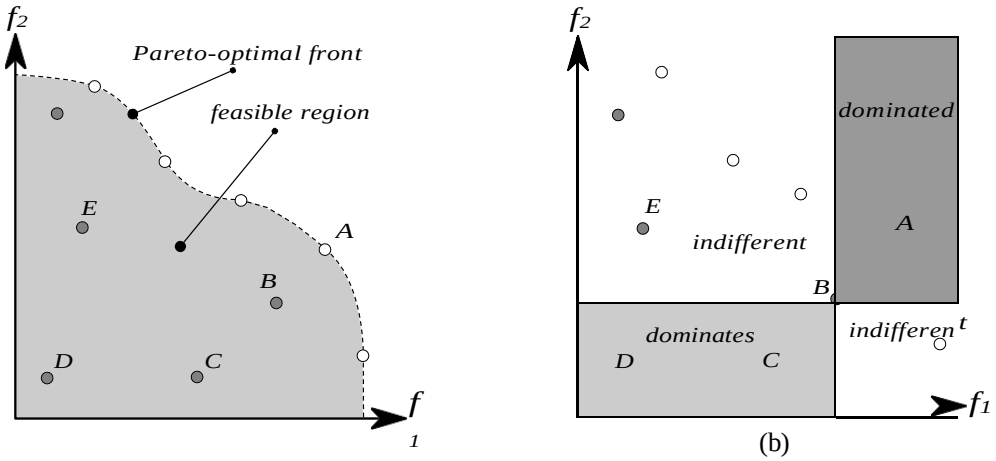

Figure 5.1 – Representation of Pareto optimality in objective space, on the left (a), and the possible relations of solutions in objective space, on the right (b).

5.1.2 - Pareto Dominance

For any two decision vectors **a** and **b**,

$$\begin{aligned} &\mathbf{a} \succ \mathbf{b} \ (\mathbf{a} \text{ dominates } \mathbf{b}) && \text{if } \mathbf{f}(\mathbf{a}) \succ \mathbf{f}(\mathbf{b}) \\ &\mathbf{a} \preceq \mathbf{b} \ (\mathbf{a} \text{ weakly dominates } \mathbf{b}) && \text{if } \mathbf{f}(\mathbf{a}) \succeq \mathbf{f}(\mathbf{b}) \\ &\mathbf{a} \sim \mathbf{b} \ (\mathbf{a} \text{ is indifferent to } \mathbf{b}) && \text{if } \mathbf{f}(\mathbf{a}) \not\succ \mathbf{f}(\mathbf{b}) \wedge \mathbf{f}(\mathbf{b}) \not\succ \mathbf{f}(\mathbf{a}). \end{aligned} \tag{5.3}$$

The definitions for a minimization problem ($\prec$, $\preceq$) are analogical. In Figure 5.1b, the light gray rectangle encapsulates the region in objective space that is dominated by the decision vector represented by *B*. The dark gray rectangle contains the objective vectors whose corresponding decision vectors dominate the solution associated with *B*. All solutions for which the resulting objective vector is in neither rectangle are indifferent to the solution represented by *B*.

5.1.3 - Pareto Optimality

A decision vector $\boldsymbol{\omega}_s \in \boldsymbol{\Omega}_f$ is said to be non-dominated, regarding a set $\mathbf{A} \subseteq \boldsymbol{\Omega}_f$,

$$\text{if } \nexists\, \mathbf{a} \in \mathbf{A} : \mathbf{a} \succ \boldsymbol{\omega}_s. \tag{5.4}$$

Hence, $\boldsymbol{a_s}$ is said to be Pareto optimal iff $\boldsymbol{a_s}$ is non-dominated regarding $\boldsymbol{a}_f$. Referring to Figure 5.1, the white points represent Pareto-optimal solutions. They are indifferent to each other. There is no single optimal solution but rather a set of optimal trade-offs. None of these can be identified as better than the others unless preference information is included, as a ranking of the objectives. The entirety of all Pareto-optimal solutions is called the Pareto-optimal set; the corresponding objective vectors form the Pareto-optimal front or surface, also known as Pareto frontier or functional efficient boundary.

5.1.4 - Global and Local Pareto-Optimal Sets

The set **A** is a local Pareto-optimal set

$$\text{iff } \forall\, \mathbf{a} \in \mathbf{A} : \exists\, \boldsymbol{a_s} \in \boldsymbol{a}_f : \boldsymbol{a_s} > \mathbf{a} \wedge \| \boldsymbol{a_s} - \mathbf{a} \| < s \wedge \| \mathbf{f}(\boldsymbol{a_s}) - \mathbf{f}(\mathbf{a}) \| < \delta, \qquad (5.5)$$

where $\| \cdot \|$ is a corresponding metric distance with $s > 0$ and $\delta > 0$. The set **A** is a global Pareto-optimal set

$$\text{iff } \forall\, \mathbf{a} \in \mathbf{A} : \exists\, \boldsymbol{a_s} \in \boldsymbol{a}_f : \boldsymbol{a_s} > \mathbf{a}. \qquad (5.6)$$

Note that, a global Pareto-optimal set does not necessarily contain all Pareto-optimal solutions and every global Pareto-optimal set is also a local Pareto-optimal set.

5.2 - GENETIC ALGORITHMS SEARCH AND DECISION MAKING

GA belong to evolutionary algorithms and are an optimization technique that is categorized as a non-derivative global search heuristic. GA perform a search and optimization procedure that is motivated by the principles of natural genetics and natural selection, originally proposed by Holland (1975). Some fundamental ideas of genetics are borrowed and used artificially to construct search algorithms that are robust and require minimal problem information. They are a robust and flexible approach that can be applied to a wide range of optimization problems, as seen in Kelner and Leonard (2004), McCall (2005) and Ebrahimnejad et al. (2015).

The genetic algorithm maintains a population of individuals, say **P(t)**, for generation **t**. Each individual represents a potential solution to the problem at hand. Each individual is evaluated to give some measure of its fitness. Some individuals undergo stochastic transformations by means of genetic operations to form new individuals. There are two types of transformation: mutation, which creates new individuals by making changes in a single individual, and crossover, which creates new individuals by combining parts from two others. New individuals, called offspring **C(t)**, are then evaluated. A new population is formed by selecting the more fit individuals from

the parent population and the offspring population. After several generations, the algorithm converges to the best individual, which hopefully represents an optimal or suboptimal solution to the problem, accordingly to Gen and Cheng (2000).

There are two important issues with respect to search strategies: exploiting the best solution and exploring the search space. Genetic algorithms provide a directed random search in complex landscapes. Genetic operations perform essentially a blind search; selection operators hopefully direct the genetic search toward the desirable area of the solution space. One general principle for developing an implementation of genetic algorithms for a particular real-word problem is to make a good balance between exploration and exploitation of the search space. To achieve this, all the components of the genetic algorithms must be examined carefully. Additional heuristics should be incorporated in the algorithm to enhance the performance.

5.2.1 - Objective Functions of the ILMF Model

The definition of appropriate objective functions has a great impact on the overall performance of the optimization process. This Section presents the objective functions considered in this work, for the automatic discretization of ILMF.

5.2.1.1 - Compliance (C)

Considering any state of the actual elastic field of the body, the strain energy U, and the potential energy P, of the applied loads, respectively given by

$$U = \int_{\Omega} \frac{1}{2} \boldsymbol{\sigma}^T \boldsymbol{\varepsilon} \, d\Omega \tag{5.7}$$

and

$$P = - \int_{\Gamma_t} \bar{\mathbf{t}}^T \mathbf{u} \, d\Gamma, \tag{5.8}$$

can be used to handle the total potential energy T. The application of the work theorem, to the global domain of the body, for the case of the actual elastic field settled in the body, leads to $P = -2U$ and therefore $T = -U$, as well as $T = P/2$. These results imply that the minimum value of the total potential energy of the body corresponds to a minimum value of the potential energy P or a maximum value of the strain energy U. The evaluation of the strain energy U of the body, requires the computation of the stress field for all nodal values which is computationally inefficient, since it requires the evaluation of derivatives of shape functions that can degrade the numerical accuracy.

Nevertheless, to compute the potential energy P , it is necessary to evaluate the displacement field, but only at static boundary nodes, the ones with no-null applied loads, which now is computationally very efficient. This process is carried out only at a few nodes and does not require the computation of derivatives of shape functions. For this reason, an efficient objective function can be defined with the structural compliance C, as

$$C = \frac{1}{2}\int_{\Gamma_t} \mathbf{t}^T \mathbf{u}\, d\Gamma = -\frac{1}{2}P. \tag{5.9}$$

Consequently, the minimum value of the potential energy P corresponds to a maximum value of $-C$ that is equivalent to a minimum value of C.

5.2.1.2 - Conditional Number (k)

Analyzing the static response, it can be seen that one of the upper bounds for the amplification of errors in the properties and structural loads is the condition number of stiffness matrix. However, even though standard stiffness matrices have very high condition numbers (higher than one million), errors or variations in structure or loads should not have a major influence on the error. The aim of this text is to clarify why, in most cases, the expectation is met. Moreover, an example is presented in which a case associated with the sensitivity judgment of the worst-case predicted by the condition number and yet the value is close to the actual error amplification. A criterion is suggested wherein the result is closer to the actual error magnification than the condition number, see Haftka (1990).

Consider discretized equations of static response equilibrium, such as those generated by a finite element model:

$$Ku = f \tag{5.10}$$

Where K is the n x n symmetric, positive, definite, stiffness matrix, u is the displacement vector, and f is the load vector.

The condition number of K, $k(K)$ is defined as:

$$k(K) = \|K\|\|K^{-1}\| \tag{5.11}$$

when the 2-norm is used

$$k(K) = \frac{\lambda_n}{\lambda_1} \tag{5.12}$$

Where λ_i denotes the i-th eigenvalue of K. It is well known $k(K)$ is an upper limit of the sensitivity of u for changes in K and f. If f is altered by Δf then

$$\frac{\|\Delta u\|}{\|u\|} \text{ ™ } k(K)\frac{\|\Delta f\|}{\|f\|} \tag{5.13}$$

and K is altered by ΔK then

$$\frac{\|\Delta u\|}{\|u + \Delta u\|} \text{ ™ } k(K)\frac{\|\Delta K\|}{\|K\|} \tag{5.14}$$

In most cases, the condition number of stiffness matrices generated by finite element models (FEM). This is similar to indicate that the calculated displacement field appears to be extremely sensitive to small errors in the stiffness matrix and load vectors. Notwithstanding this theoretical sensitivity, the stiffness matrix (eg, by reduced integration) and the load vector (eg, mass loads) are still approximated without concern of amplification of errors predicted by the very large condition number. Indeed, it is known that the condition number may be an overly conservative assessment of error sensitivity.

5.2.2 - Formulation and implmentation

The aim of the numerical problem optimization is to minimize the objective function using the ILMF model which yields different results, depending on the chosen function, by finding the optimal mesh free parameters, N, a_s and a_q such that the geometrical constraints of the problem are satisfied. This thesis presents two optimization schemes which are based on: a) the energy relative error (mono-objective optimization scheme) and b) the compliance and the Conditional number (multi-objective optimization scheme).

The basic optimization process is as follows: the initial population is randomly generated according to the predefined population size of individuals. Then, the fitness function is calculated for each member of the population and scaled using a rank process, which is used later in the selection process. The reproduction operator is implemented based on a tournament selection. Both mutation and crossover are constraint dependent. The genetic algorithm described above generates a stochastic values sequence of design variables which are evaluated

through the objective function. Finally, the optimization process is terminated if the number of generations exceeds the predefined maximum number, which is selected as in this scheme, or if the average change in fitness function.

5.2.2.1 - Mono-objective Optimization scheme

The mathematical formulation of the mono-objective optimization scheme is as follows

$$\begin{aligned} &\text{minimize} && r_\varepsilon(a_s, a_q) \\ &\text{subject to} && \mathbf{e}(a_s) = a_s^{min} \le a_s \le a_s^{max} \\ & && \mathbf{e}(a_q) = a_q^{min} \le a_q \le a_q^{max} \end{aligned} \tag{5.15}$$

in which r_ε is the energy relative error, to be presented in the next chapter; a_s^{min}/a_q^{min} and a_s^{max}/a_q^{max} denote the minimum and the maximum allowable limits for the mesh free discretization parameters a_s and a_q, respectively.

The approach of the automatic optimization of the discretization parameters is progamated into a single and unique routine, to automatically compute the ILMF discretization parameters, a_s and a_q, is a very efficient way. Figure 5.2 presents the flowchart of the mono-objective process.

5.2.2.2 - Multi-objetive Optimization scheme

The mathematical formulation of the multi-objective optimization scheme is as follows

$$\begin{aligned} &\text{minimize} && C(a_s, a_q, N, \boldsymbol{N_{x_1}}, \boldsymbol{N_{x_2}}) \\ & && k(a_s, a_q, N, \boldsymbol{N_{x_1}}, \boldsymbol{N_{x_2}}) \\ &\text{subject to} && \mathbf{e}(a_s) = a_s^{min} \le a_s \le a_s^{max} \\ & && \mathbf{e}(a_q) = a_q^{min} \le a_q \le a_q^{max} \\ & && \mathbf{e}(N) = N^{min} \le N \le N^{max} \\ &\text{where} && \boldsymbol{N_{x_1}} = (N_{x_{1_1}}, N_{x_{1_2}}, \ldots, N_{x_{1_n}}) \\ & && \boldsymbol{N_{x_2}} = (N_{x_{2_1}}, N_{x_{2_2}}, \ldots, N_{x_{2_n}}) \end{aligned} \tag{5.16}$$

This optimization requires only one steps procedure to be performed, all parameters are defining in a unique routine as presented in Figure 5.3. It is quite important to stress that the accuracy of the MLS parameter and the efficiency of the local domain parameter are combined into a fully

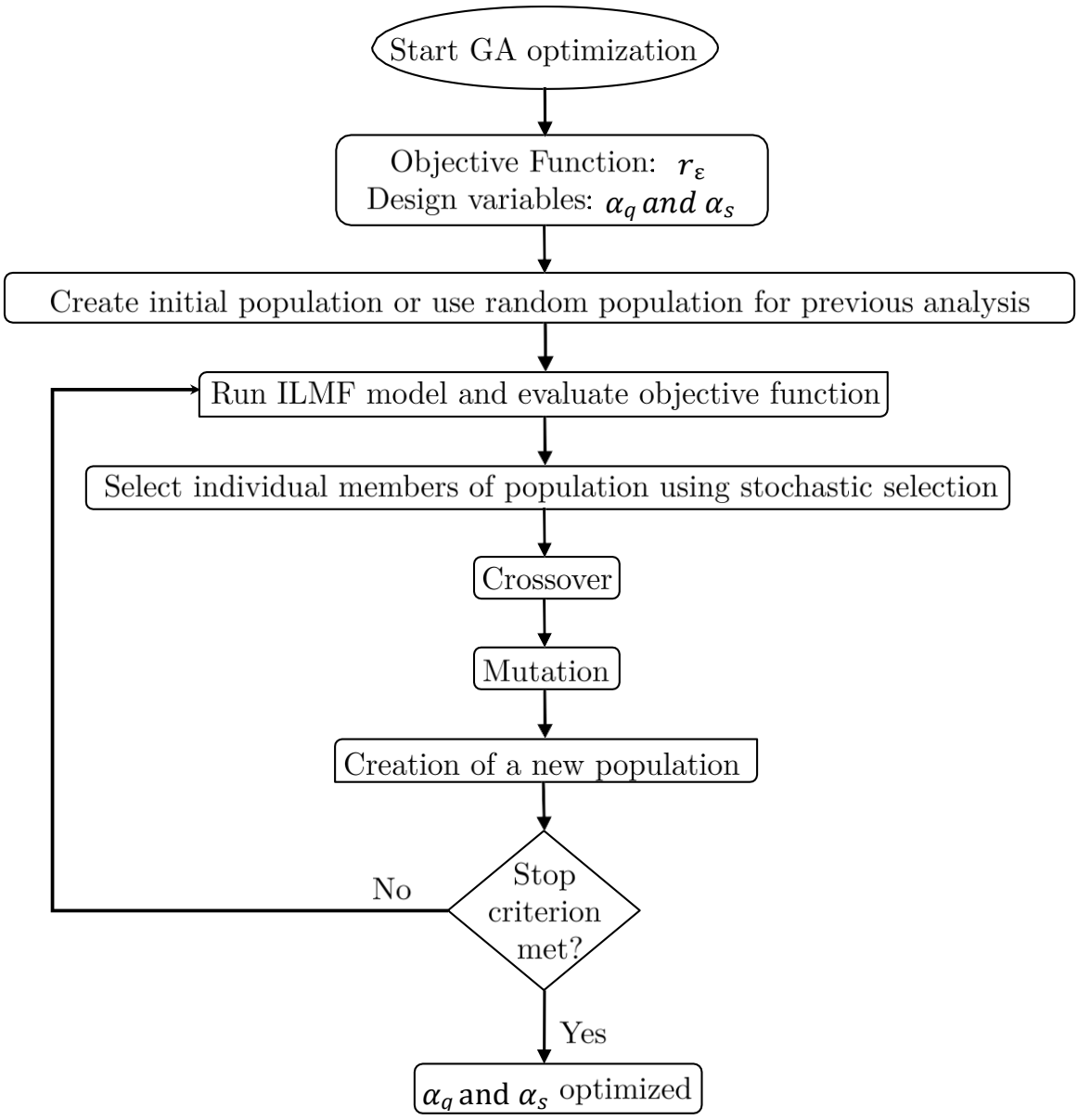

Figure 5.2 – Flowchart of the routine defined for the mono-objective optimization.

automated routine that can optimize a mesh free nodal configuration without the need of any analytical solution and for any geometry domain. The routine presented in this paper, although only combined with the ILMF for solving linear elastic problems, can be easily adapted to be used with any local mesh free method for solving different engineering problems. Even faster results can be obtained with this routine by using the MATLAB parallel environment, which performs multiple analyses simultaneously.

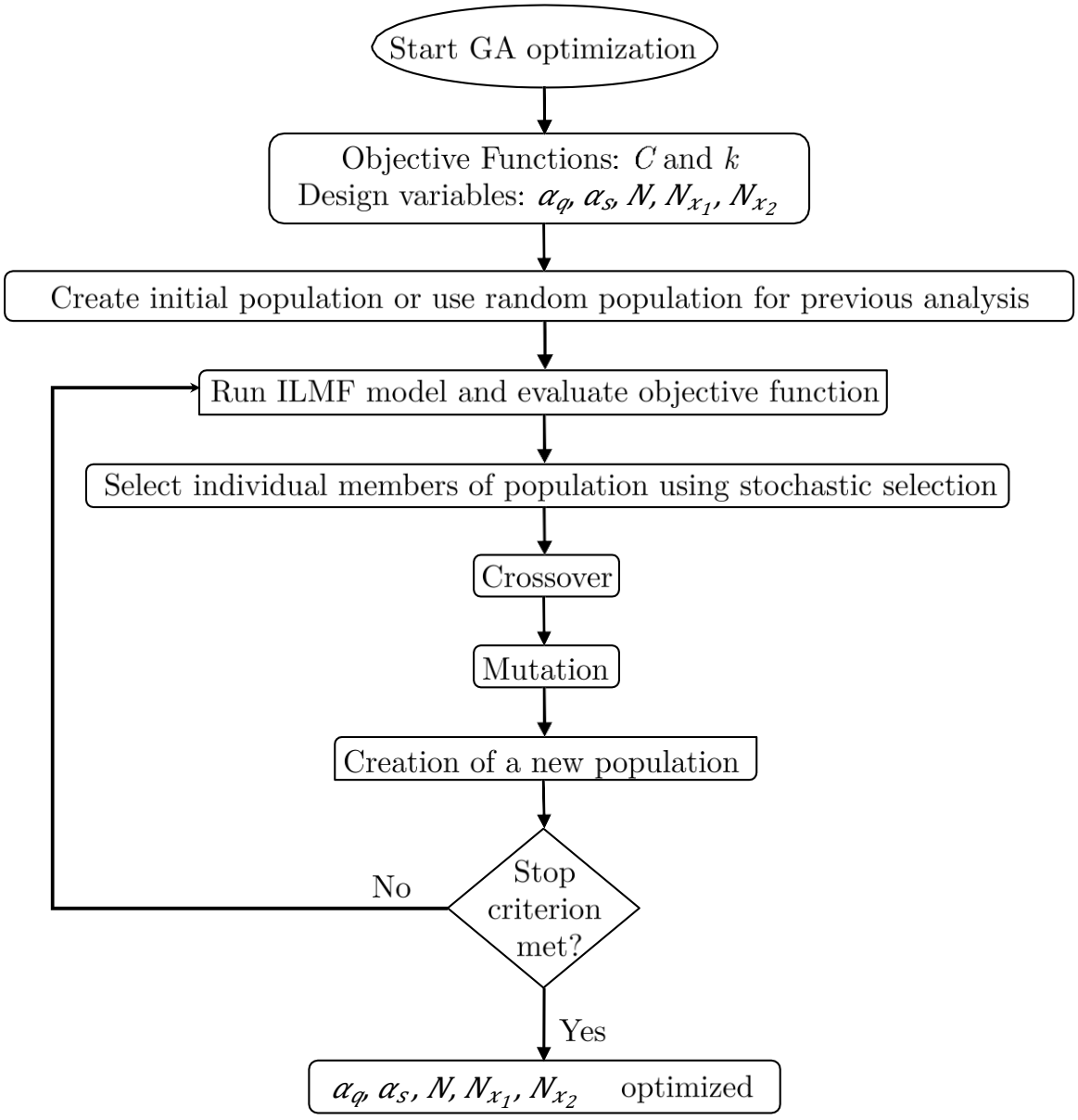

Figure 5.3 – Floowchart of the routine defined for the Multi-objective Optimization.

6 - NUMERICAL RESULTS

Numerical results are presented in this section to illustrate the accuracy and efficiency of the ILMF numerical model carried out with multi-objective optimization process. These results are always compared with the analytical results and the other local mesh-free method; MLPG-5 is among these methods and, for the sake of simplicity, it is always referred to as MLPG. The analytical solution of this four benchmark problems solved is this section, it is presented in Dally and Riley (1991).

For a node i, from a mesh free discretization, the local support Ω_s and the local integration domain Ω_q sizes are, respectively, the parameters a_s and a_q, defined in equations (4.16) and (4.17). The size of the support is a very important parameter that depends on the nodal distribution, and thus requires a proper refinement. Through testing, it was verified that the optimal size of the support varies between $a_s = 3.0 \sim 6.0$ and $a_q = 0.4 \sim 0.6$.

For error estimation, in displacement and energy, L_2 norms can be used, respectively as

$$\|\mathbf{u}\| = \left[\int_{\Omega} \mathbf{u}^T \mathbf{u} \, d\Omega \right]^{1/2} \tag{6.1}$$

and

$$\|\boldsymbol{\varepsilon}\| = \left[\frac{1}{2} \int_{\Omega} \boldsymbol{\varepsilon}^T \mathbf{D} \, \boldsymbol{\varepsilon} d\Omega \right]^{1/2}. \tag{6.2}$$

Then the relative errors, respectively for $\|\mathbf{u}\|$ and $\|\boldsymbol{\varepsilon}\|$ are given by

$$r_u = \frac{\|\mathbf{u}_{num} - \mathbf{u}_{exact}\|}{\|\mathbf{u}_{exact}\|} \tag{6.3}$$

and

$$r_\varepsilon = \frac{\|\boldsymbol{\varepsilon}_{num} - \boldsymbol{\varepsilon}_{exact}\|}{\|\boldsymbol{\varepsilon}_{exact}\|}. \tag{6.4}$$

6.1 - CANTILEVER-BEAM

As a benchmark problem, it is considered a cantilever beam with dimensions $L \times D$ and with unit depth, subjected to a parabolic traction at the free end, as shown in Figure 6.1. Material

properties of the cantilever beam are taken as Young's modulus $E = 3.0 \times 10^7$ and the Poisson's ratio $\nu = 0.3$ and the beam dimensions are $D = 12$ and $L = 48$. The shear force is $P = 1000$. The beam is assumed as a plane stress state and the parabolic traction is defined as

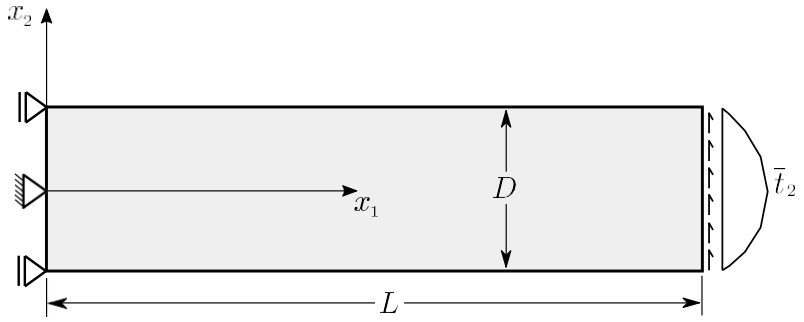

Figure 6.1 – Timoshenko cantilever beam.

$$\bar{t}_2(x_2) = -\frac{P}{2I}\left(\frac{D^2}{4} - x_2^2\right), \tag{6.5}$$

where $I = D^3/12$ is the moment of inertia. The exact displacement components for this problem are given by

$$\begin{Bmatrix} u_1(x_1, x_2) \\ u_2(x_1, x_2) \end{Bmatrix} = \frac{P}{6EI}\begin{Bmatrix} -x_2\left[(6L - 3x_1)x_1 + (2+\nu)\left(x_2^2 - \frac{D^2}{4}\right)\right] \\ 3\nu x_2^2(L - x_1) + (4+5\nu)\frac{D^2 x_1}{4} + (3L - x_1)x_1^2 \end{Bmatrix} \tag{6.6}$$

and the exact stress components are given by

$$\begin{Bmatrix} \sigma_{11}(x_1, x_2) \\ \sigma_{22}(x_1, x_2) \\ \sigma_{12}(x_1, x_2) \end{Bmatrix} = \begin{Bmatrix} -\frac{P(L - x_1)x_2}{I} \\ 0 \\ -\frac{P}{2I}\left(\frac{D^2}{4} - x_2^2\right) \end{Bmatrix} \tag{6.7}$$

6.1.1 - Performance of the reduced integration of ILMF

The relevant performance of the ILMF reduced integration is a very important attribute of this numerical method. Linear reduced integration is considered with 1 point per segment of the local boundary. Additional integration points can be considered by subdividing a boundary segment in identical segments, which leads to equally-spaced integration points. The performance of the method can be assessed through numerical results, as a function of the integration points defined on each boundary of the respective local domain. The behavior of the ILMF energy relative error (r_s), in terms of the integration points is represented in Figure 6.2.

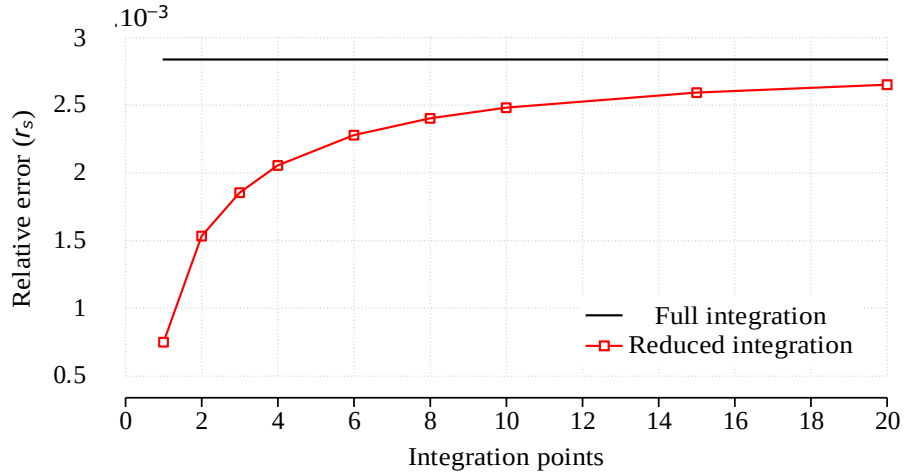

Figure 6.2 – ILMF energy relative error (r_s), as a function of the number of equally-spaced integration points, for a regular distribution of $33 \times 5 = 165$ nodes; results of MLPG, obtained with 10 points per segment of the local domain, referred to as full integration.

For the regular distribution of $33 \times 5 = 165$ nodes; the MLPG relative error, computed with 10 points per segment of the respective local domain, referred to as full integration, is also plotted for comparison. It can be seen that the lower value of the norm monotonically converges to the higher value of the norm, as a function of the integration points. The reduced integration of ILMF monotonically converges to the full integration of MLPG, as a function of the integration points, with the best result obtained for only 1 point per segment of the respective local domain. This is an important result that evidences that the linear reduced integration of the ILMF model leads to better results than those obtained with the MLPG full integration.

A discussion of this behavior of ILMF can be presented as follows. The total potential energy theorem leads to an upper limit of the strain energy, which represents a lower limit of the stiffness, of the exact solution settled in the body. Thus, any approximate solution underestimates the strain energy of the exact solution, which corresponds to overestimating its corresponding stiffness. Therefore, as shown in Figure 6.2, the full integration of MLPG is always stiffer than the reduced integration of ILMF; for only 1 point per segment of the respective local domain, the result is very close to the exact solution of the problem. When additional segments, with 1 point each, are considered in the reduced integration, the ILMF solution monotonically converges to the MLPG solution of the full integration and therefore, it can be deduced that the additional integration points monotonically increase the stiffness of ILMF, obtained with only 1 point. The best solution is always obtained from the lowest stiffness, computed with only 1 point per segment of the respective local domain.

Note that the improvement of the solution accuracy, generated by the reduced integration, has been already used in the standard FEM, as a measure to prevent locking problems of fully integrated elements.

As a final conclusion of this discussion, it is important to mention that the ILMF reduced integration, along each side of the local domain, does not lead to any sort of spurious instability. This behavior is a direct consequence of having a total of 4 integration points, schematically represented in Figure 4.4, to compute the stiffness associated to each local node which, therefore, prevents the generation of spurious zero-energy modes, unlike nodal integration methods without stabilization. Nodal integration in mesh free methods leads to instabilities due to the fact that each node is associated with a support domain, where integrations are carried out, to compute the nodal stiffness. This means that each integration domain is associated with just 1 integration point, that is the node and thus, when only 1 point is used for integration of higher order functions, the nodal integration inevitably causes fatal instabilities.

Another test was carried out to assess the influence of the integration points on the ILMF solution accuracy. Four regular distributions of $13 \times 4 = 52$, $65 \times 9 = 585$, $97 \times 13 = 1261$ and $129 \times 17 = 2193$ nodes were used. The results obtained for the ILMF energy relative error (r_s), as a function of the integration points are presented in Figure 6.3,

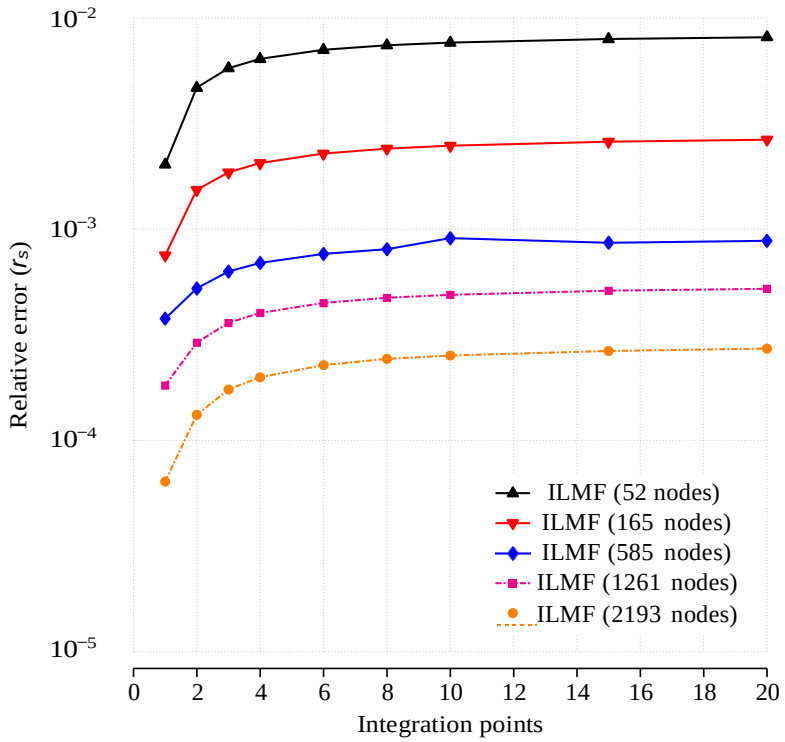

Figure 6.3 – ILMF energy relative error (r_s), for the beam discretization with 52, 165, 585, 1261 and 2193 nodes, as a function of the equally-spaced integration points, on the boundaries of the respective local domain.

where it can be seen that the ILMF solution accuracy increases with the number nodes of the discretization, as expected; the overall ILMF relative error decreases with finer nodal distributions, requiring only 1 point per segment of the respective local domain to obtain the

most accurate results. This is an important result that testifies that ILMF is an efficient numerical method.

A final test was carried out, in order to asses the ILMF accuracy when using higher order polynomial basis. Three regular distributions of $13 \times 4 = 52$, $33 \times 5 = 165$ and $65 \times 9 = 585$ nodes were considered. Figure 6.4

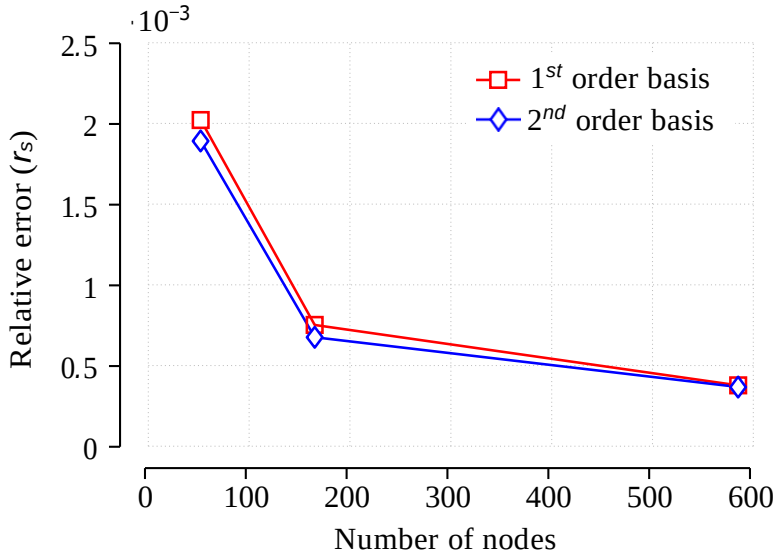

Figure 6.4 – ILMF relative error r_s, for the beam discretization with $13 \times 4 = 52$, $33 \times 5 = 165$ and $65 \times 9 = 585$ nodes, as a function of the number of nodes, considering a complete set of 1st and 2nd order polynomial basis for the MLS approximation. As expected, the ILMF accuracy increases with finer nodal distributions and higher order polynomial basis.

clearly shows the high accuracy of the ILMF reduced integration for high-order polynomial basis, providing a stable convergence rate.

6.1.2 - Influence of the local compact support domain size (a_s) and the local integration domain size (a_q)

The local character of the MLS approximation plays a key role in the solution performance. It is a direct consequence of the compact support of each node, where the respective shape functions are defined. Rectangular compact supports have been used in this benchmark problem. The size of the compact support determines, in a neighborhood of a sampling point, the respective domain of definition of the MLS approximation at this point, as Figure 4.2 schematically represents. This domain of definition contains the nodes whose shape functions do not vanish at the sampling point. Finally, the influence domain of each node results from the union of the MLS definition domains, of all points in the local integration domain of the node, which thus contains the nodes used to define the stiffness of the node.

Therefore, for each node of a mesh free discretization, the size of the compact support and the size of the arbitrary parameters a_s and a_q, are very important parameters in a local mesh free analysis that can affect the performance of the solution, as a consequence of the pattern of the nodal distribution. If the nodal distance is too large, the support regions around each node can never intersect with each other, thus leading to no meaningful results. In the other extreme, if the nodal distance is too small, a lot of nodes can couple to each other, thus making the local character of the MLS approximation to be lost.

6.1.2.1 - Local compact support domain (a_s)

Usually, the parameter a_s is greater than 1.0, to make sure that there are enough points to support the nodes on the global boundary. For a small size, the algorithm of MLS approximation may be singular and the shape function cannot be constructed, because there is not enough nodes for interpolating.

The influence of size parameter (a_s) in the solution is obtained when the (a_q) is fixed. The Figure 6.5 shows the variation of energy relative error, compliance and condition number, as a function of the size of the local support domain with seven ratios, which vary from 3.5 to 6.5 with 0.5 increments, and a_q = 0.5. These results are presented for the beam discretization with $13 \times 4 = 54$, $33 \times 5 = 165$ and $65 \times 9 = 585$ nodes.

The Figure 6.5 shows that for values between 4.0 and 4.5 at the local support domain (a_s) the relative energy errors is low by regular nodal discretization. The compliance value (C) presents a small variation, ranging bettween -4.4 for discretization with a large number of nodes and -4.6 for discretization with a few number of nodes. Additionally, it is identified that there is a directly proportional relationship between the size of the local compact support domain parameter (a_s) and the condition number (k). Similar results are obtained for displacement.

6.1.2.2 - Local integration domain (a_q)

The parameter a_q is chosen to be less than 1.0 to ensure that the local sub-domains of the internal nodes are entirely within the solution domain, without being intersected by the global boundary.

The influence of (a_q) is obtained when the (a_s) is fixed. The Figures 6.6 shows the variation of energy relative error, compliance, and condition number, as a function of the size of the local integration domain with seven ratios varying from 0.4 to 0.7, with 0.05 increments. These results are presented for the beam discretization with $13 \times 4 = 54$, $33 \times 5 = 165$ and $65 \times 9 = 585$ nodes.

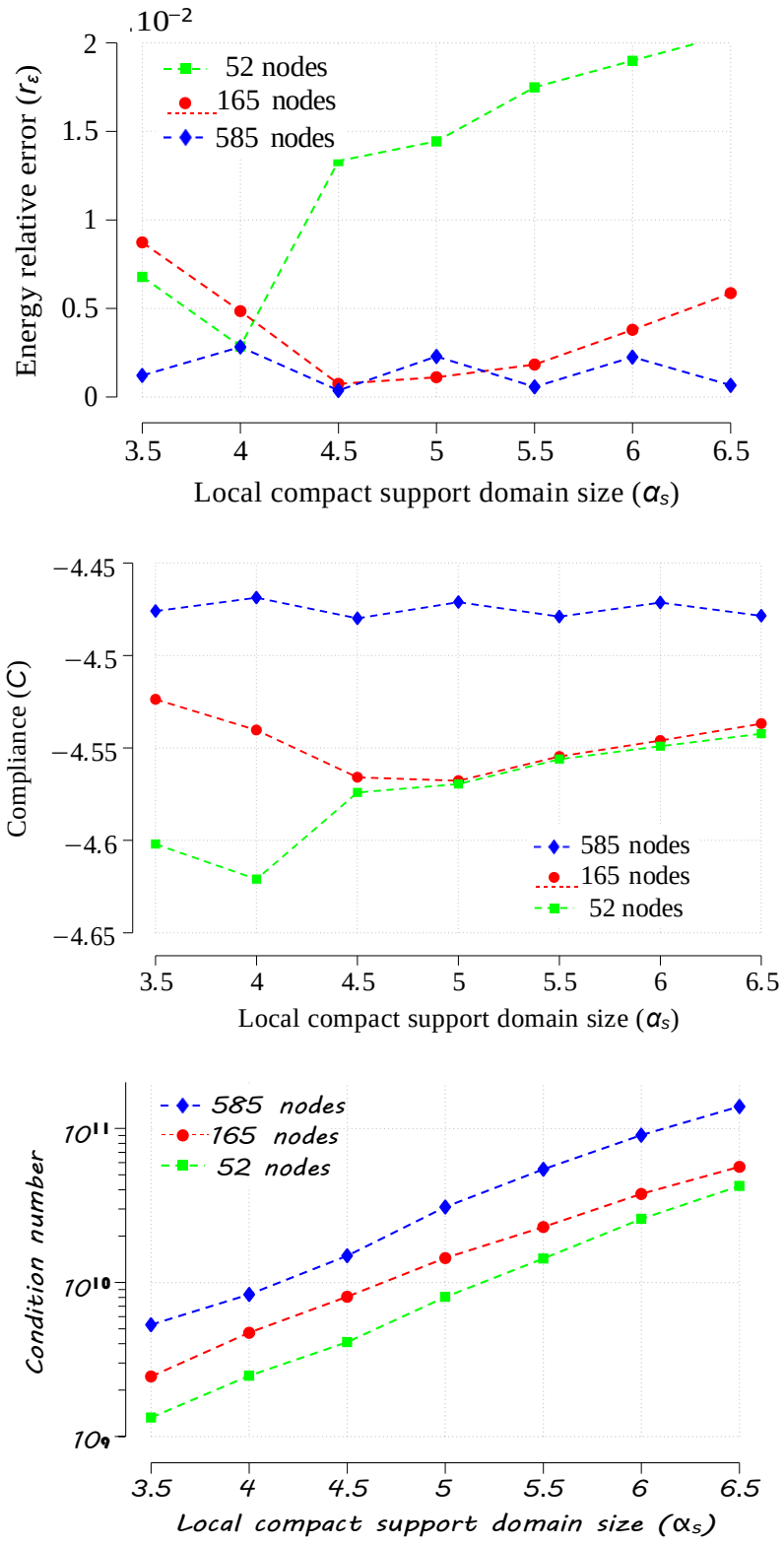

Figure 6.5 – Analysis of influence of the local compact support domain size on Energy relative error (r_ε), Compliance (C) and Condition number (k), carried out for three discretization with $13 \times 4 = 52$, $33 \times 5 = 165$ and $65 \times 9 = 585$ nodes, and $a_q = 0.5$.

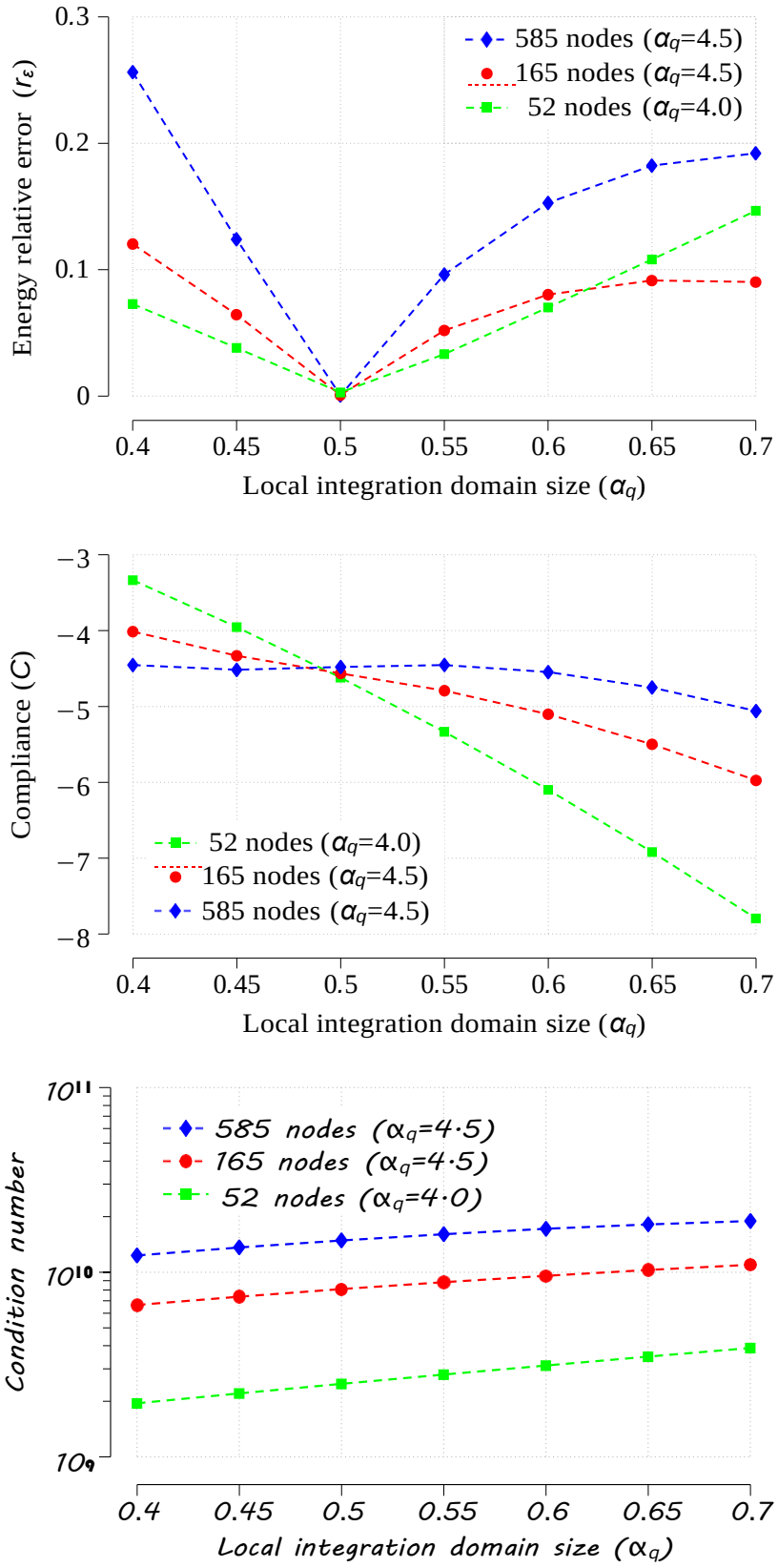

Figure 6.6 – Analysis of influence of the local compact support domain size on Energy relative error (r_ε), Compliance (C) and Condition number (k), carried out for three discretization with $13 \times 4 = 52$, $33 \times 5 = 165$ and $65 \times 9 = 585$ nodes, and $a_q = 0.5$.

Figure 6.6 shows that the value of 0.5, for local integration domain, (a_q) presents low relative energy error in regular discretization, and for this value, the compliance value ($C = -4.5$) is the same for the three discretizations carried out in this problem. Additionally, it is identified that these there values forms a directly proportional relationship between the size of the local integration domain parameter (a_q) and the condition number (k). Similar results are obtained for displacement.

6.1.3 - Irregular nodal distributions

The mesh-free methods may require discretizations with irregular nodal distribution by P problems with special geometries or that present discontinuities in their domain and contour. Consequently, the accuracy of the ILMF model must be assessed, in dealing with irregular nodal distributions. In this thesis, two types of irregularities are presented, with fixed local domain (Level-1) and variable local domain (Level-2).

The irregularity of the nodal distribution can be generated simply by randomly changing the coordinates of a nodal regular distribution, inside the local domain of integration. This process, referred to as level-1 of irregularity, can be controlled through an arbitrary parameter c_n that varies the range from 0.0 to 0.4, in which $c_n = 0.4$ corresponds to a maximum irregularity, as presented by Liu (2003).

Figure 6.7 shows three nodal distributions of the beam discretization, with 189 nodes and level-1 of irregularity, with two different irregularity configurations, regarding to the boundary nodes.

Results obtained for the irregularity of the level-1, are presented in Figure 6.8 for the MLPG and ILMF. Each value of c_n is the normal average of the twelve different irregular nodal discretizations. These results confirm the remarkable accuracy of ILMF, even for mild irregular nodal distributions. In addition, it is noticeable that there is a direct relation between the parameter c_n and the energy relative error. Similar results are obtained for displacement.

A severe irregularity of the nodal distribution can be generated in two steps; first, the coordinates of a nodal regular distribution are randomly changed, allowing each node to move outside the respective local domain of integration and, next, each local domain is regenerated, in order to include the new location of the respective node, by considering the middle of the distance between the node and its neighboring nodes. This process, referred to as level-2 of irregularity, can be controlled through the same arbitrary parameter c_n that now varies in the range from 0.0 to 0.9, in which $c_n = 0.9$ corresponds to a maximum irregularity.

The Figure 6.9 shows three nodal distributions of the beam discretization, with 55 and 189 nodes with irregularity of level-2 of interior nodes only (Configuration A).

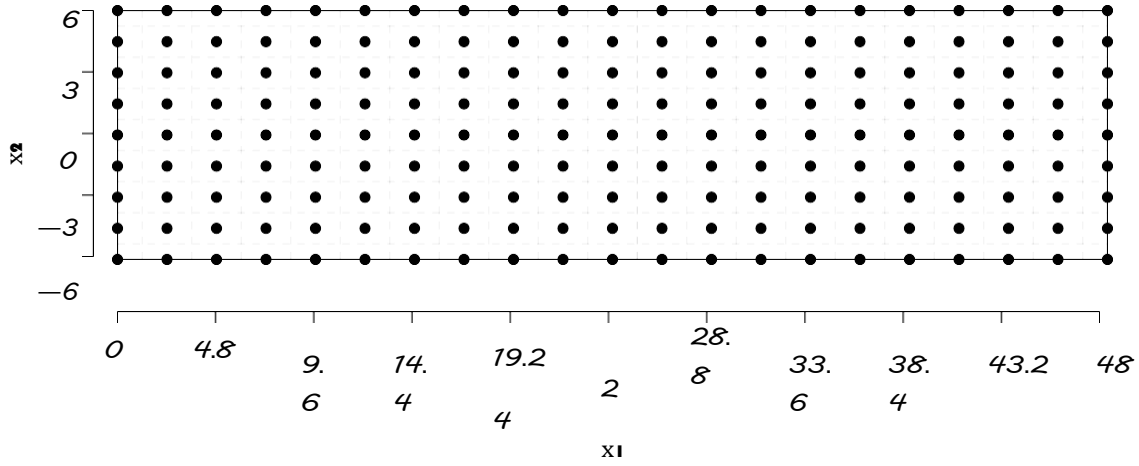

(a) $c_n = 0.0$

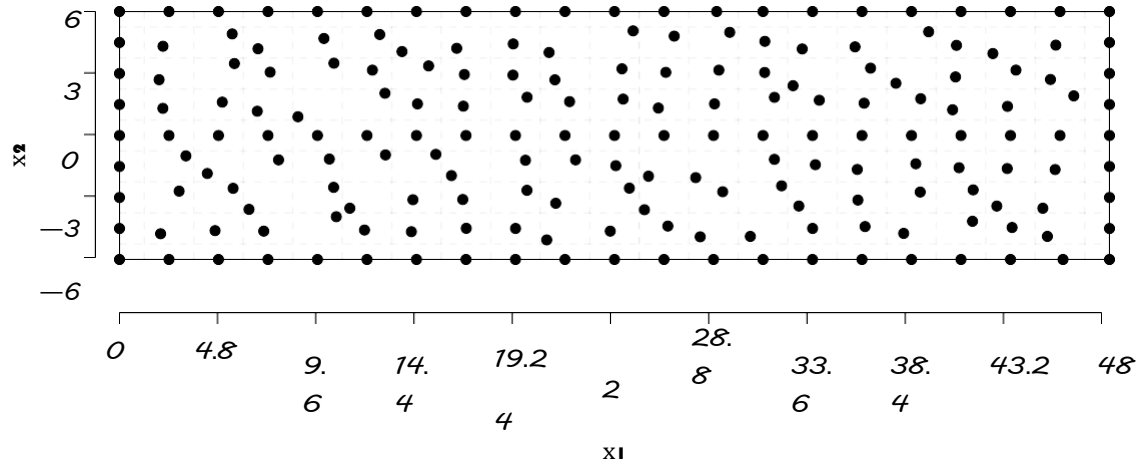

(b) $c_n = 0.4$, configuration A

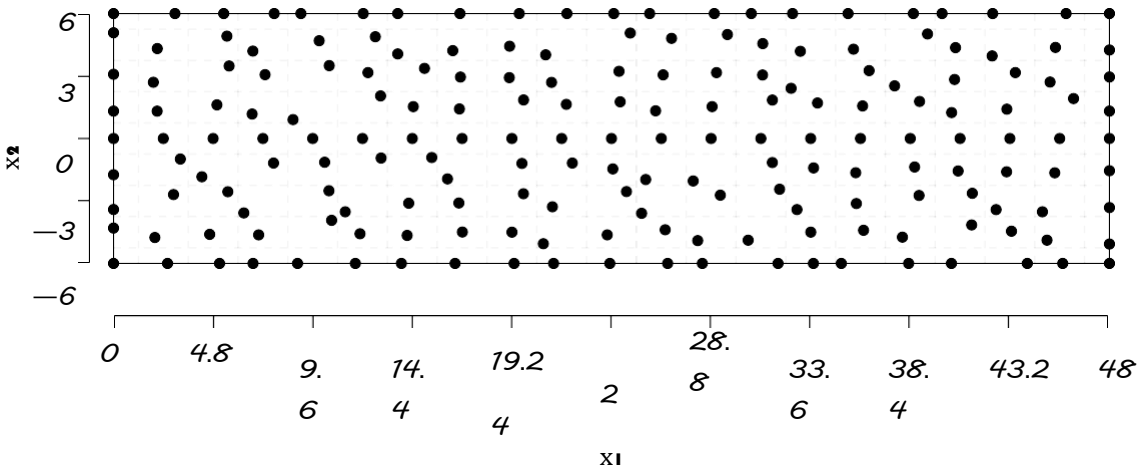

(c) $c_n = 0.4$, configuration B

Figure 6.7 – Nodal distributions of the beam discretization with 189 nodes and level-1 of irregularity; in configuration A, only interior nodes have an irregular distribution, as presented by Liu (2003), while in configuration B all nodes are irregularly distributed.

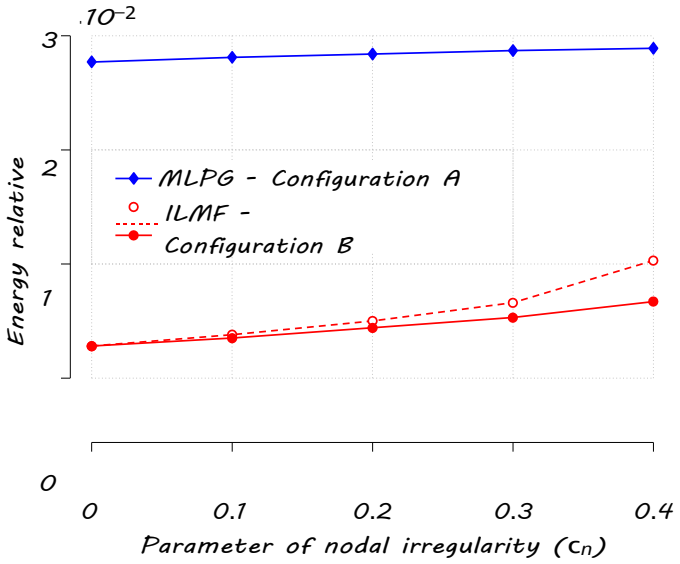

(a) MLPG (Liu, 2003) and ILMF

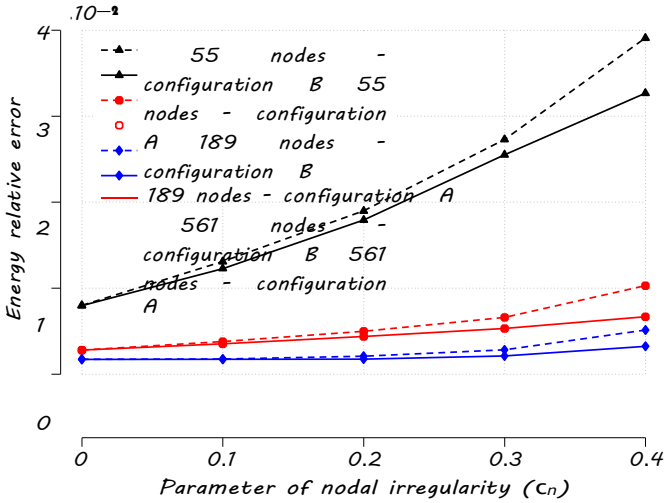

(b) ILMF, configuration A and B with $\alpha_s = 2.11$

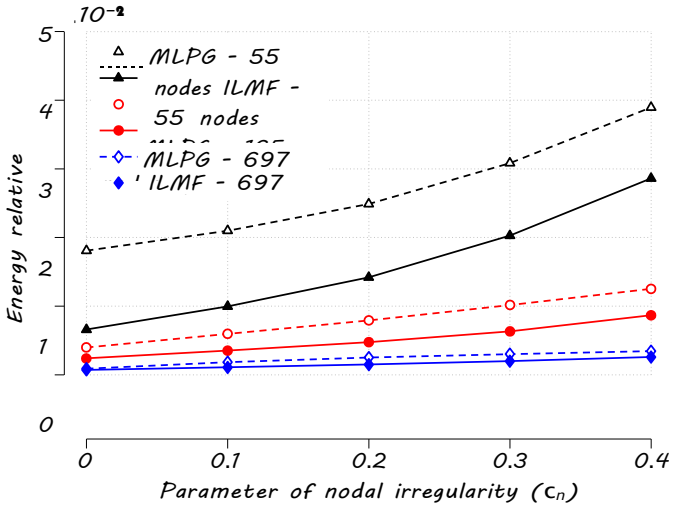

(c) MLPG and ILMF, configuration A with $\alpha_s = 2.12$

Figure 6.8 – ILMF energy relative error, computed with $a_q = 0.5$, as a function of the

irregularity parameter c_n, obtained with irregular nodal distributions with 55, 189, 561 and 697 nodes of the beam discretization. The ILMF accuracy is evident.

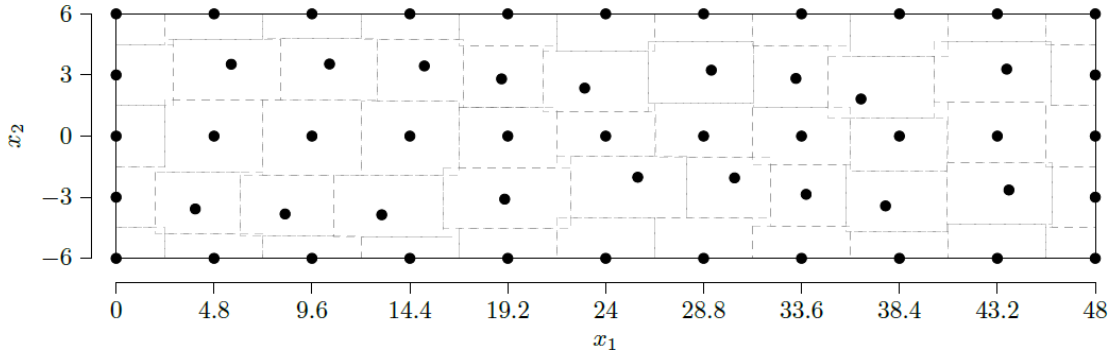

(a) 55 nodes with $c_n = 0.4$

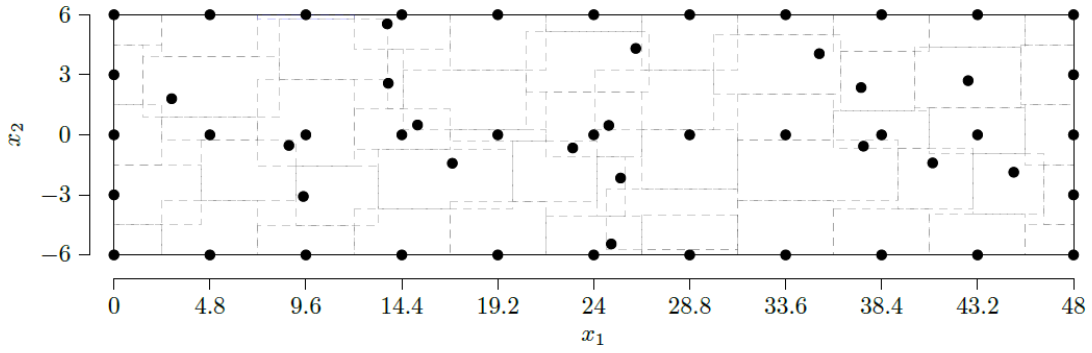

(b) 55 nodes with $c_n = 0.8$

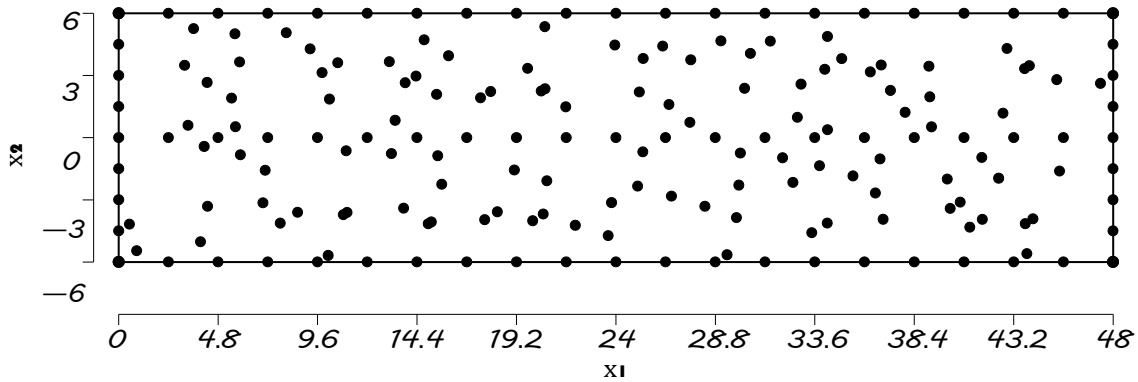

(c) 189 nodes with $c_n = 0.8$

Figure 6.9 – Nodal distributions of the beam discretization, with 55 and 189 nodes with irregularity of level-2 of interior nodes only.

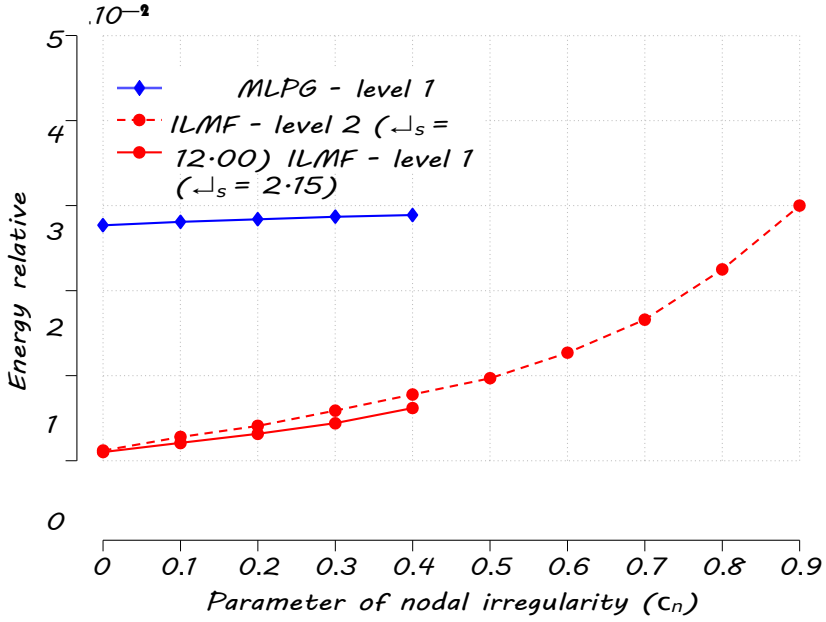

(a) Level-1 and level-2 irregularities

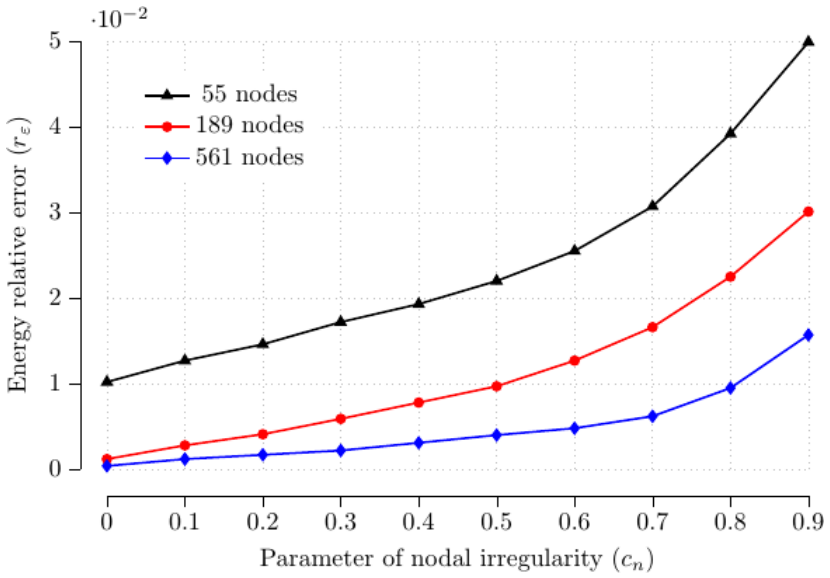

(b) ILMF, level-2 irregularities with α_s = 12.00

Figure 6.10 – Energy relative error of ILMF and MLPG, as presented by Liu (2003), as a function of the irregularity parameter c_n, obtained with irregular nodal distributions of the beam discretization. The ILMF accuracy is evident.

Results obtained for irregular nodal distributions of level-2, are presented in Figure 6.10, where still, a high level of accuracy of ILMF results can be seen. These results also show that the higher is the irregularity, the higher must be the parameter c_n, in order to keep the accuracy of results. In addition, it can be seen that when the larger is the number of nodes better is the accuracy of the results. A final note to confirm the remarkable accuracy of the ILMF model, even for severe irregularities of nodal distributions, which makes ILMF a very reliable mesh free numerical model. Similar results are obtained for displacement.

The irregular nodal distribution with variable local domain (Level-2) has important characteristics, one of them is the possibiliy to solve problems with a very irregular noda arrangement or make specific nodal distributions according to the need of user.

The Figure 6.11 shows three different nodal distributions (regular, irregular and especial) of the beam discretization with 145 nodes and irregularity of level-2 of interior nodes only (Configuration A).

In Figure 6.12 the principal results for the vertical displacement, and stress ($\sigma 11$ and $\sigma 12$) are presented. In general, It can be perceived that there is a good agreement with the analytical results independent of the distribution used.

Another important observation is that the two levels of the irregularity (Level-1 and Level-2) have a similar behavior for the low irregularity. Consequently, the irregular type 2 will be used to make the automatic discretization.

6.1.4 - Automatic Discretization

This section is divided into two schemes: Mono-objective and Multi-objective optimization. In the first scheme, the GA is implemented in order to minimize one objective, the energy relative error (r_ε), using the mesh-free parameters a_q and a_s as a design variables validating the methodology implemented. In the second scheme, GA minimize two objectives, the Compliance (C) and the Condition number (k), using the number and nodes position (N, N_{x_1}, N_{x_2}), parameters a_q and a_s as a problem variables. The second scheme is called the automatic discretization for the design mesh-free methods, this process will be addressed only ILMF with configuration A and irregularity Level-2, thinking about future problems with greater geometric irregularity.

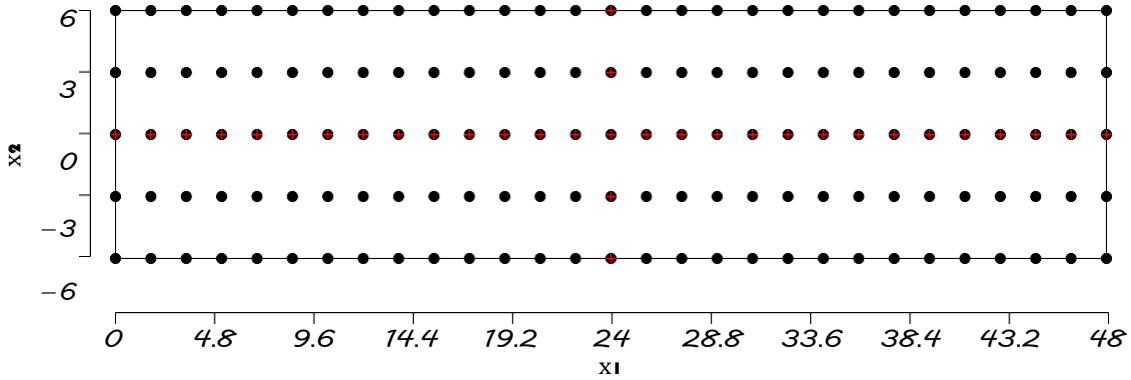

(a) Regular distribution

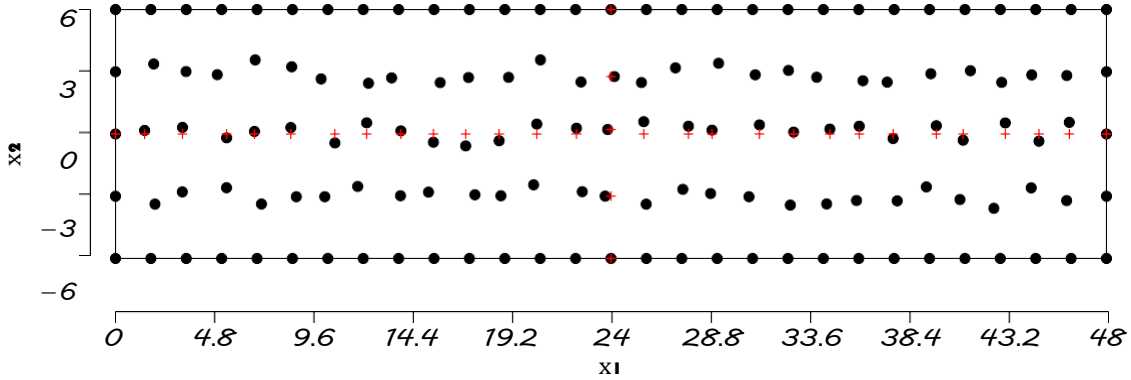

(b) Irregular distribution

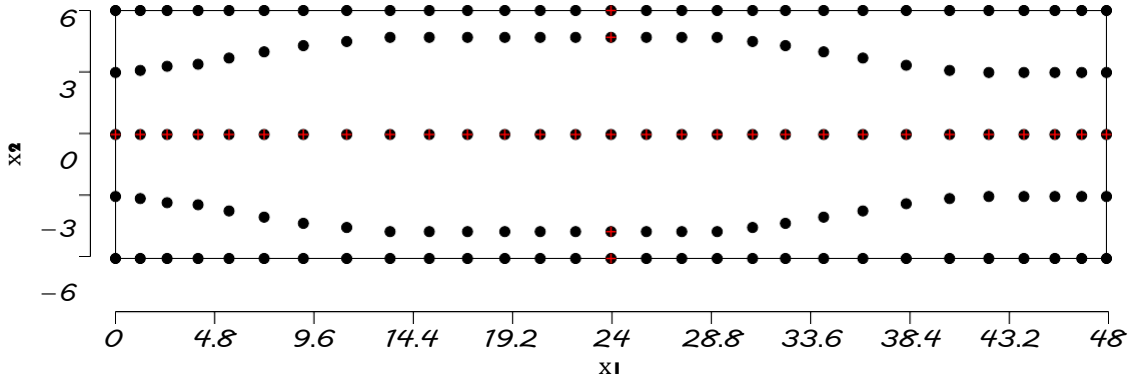

(c) Especial distribution

Figure 6.11 – Three different nodal distributions of the beam with 29×5 = 145 nodes with irregularity of level-2 and Configuration A.

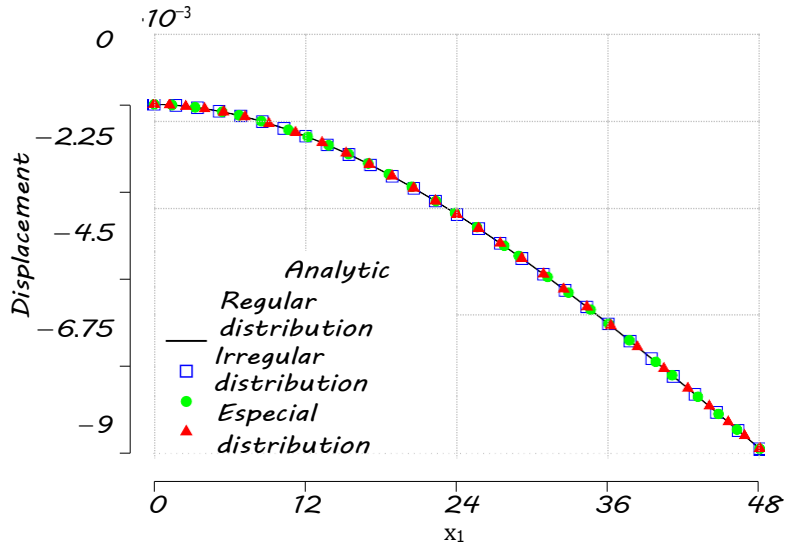

(a) Vertical displacement

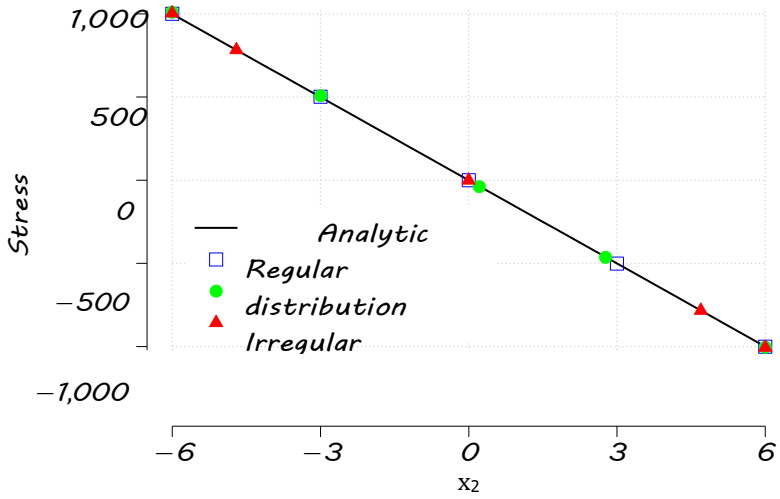

(b) Vertical displacement

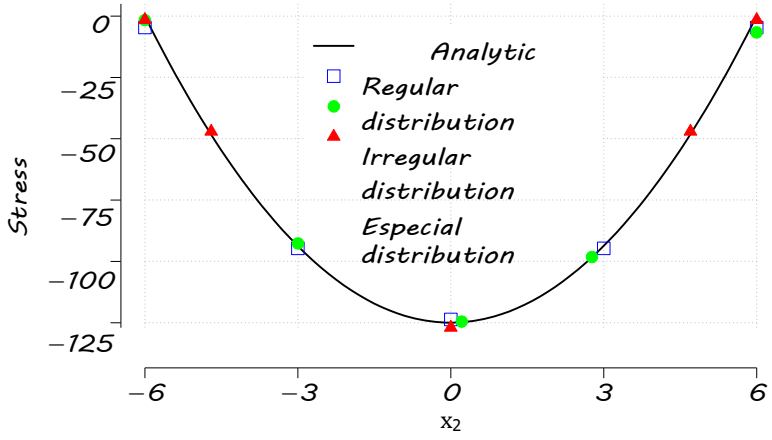

Figure 6.12 – Principal displacement and stress for the cantilever beam with three different nodal distribution.

6.1.4.1 - Mono-objective Optimization

The main objective of this scheme is to asses the performance of the optimization process related to the accuracy. Only the major computational cost, that is the cost of generating and solving the global system of algebraic equations, was measured. The decision variables, a_s and a_q, are defined as continuous in the intervals,

$$a_s = [2\ 13] \quad and \quad a_q = [0.4\ 0.7]. \tag{6.8}$$

The objective functions are related to the decision variables. This means that by selecting various values for the design variables, a_s and a_q, we can make changes in the objective function r_ε, of the ILMF analysis.

In order to evaluate the mono-objective optimization process, it is calculated the energy relative error optimized as a function of the irregularity parameter c_n for irregular nodal discretizations with 55 nodes.

The results obtained are compared with a different nodal discretization with 697 nodes in Figure 6.14. To each point of c_n, the normal average of results were obtained from twelve different analysis. Figure 6.13 presented the scheme of irregular nodal configuration for the analyses.

The Figure 6.14 showed the relative energy error for two different nodal discretization (55 and 697 nodes) with configuration A, as a function of parameter of nodal irregularity (c_n). The discretization with 55 nodes is carried out with the Mono-objective optimization process. The Figure 6.14 showed the relative energy error for two different nodal discretization (55 and 697 nodes) with configuration A, as a function of parameter of nodal irregularity (c_n). The discretization with 55 nodes is carried out with the Mono-objective optimization process.

It can be seen that the results from the solution using genetic algorithm optimization presented more accuracy than the discretization for both local methods without the optimization. For example, the discretization with 55 nodes using GA presented an minor energy relative error than the discretization with more nodes (697 nodes) using the ILMF and MLPG. In addition, it is visible that the IMLF displayed a better accuracy than the MLPG, in general; for this reason the Multi-objective optimization process will be only used for the ILMF. Similar results are obtained using nodal irregularity Level-2.

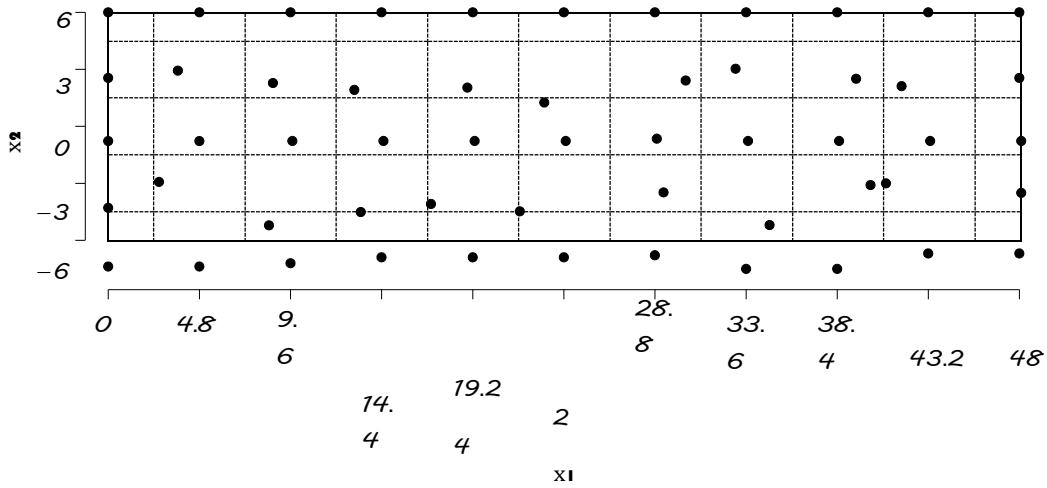

(a) 55 nodes with $c_n = 0.5$

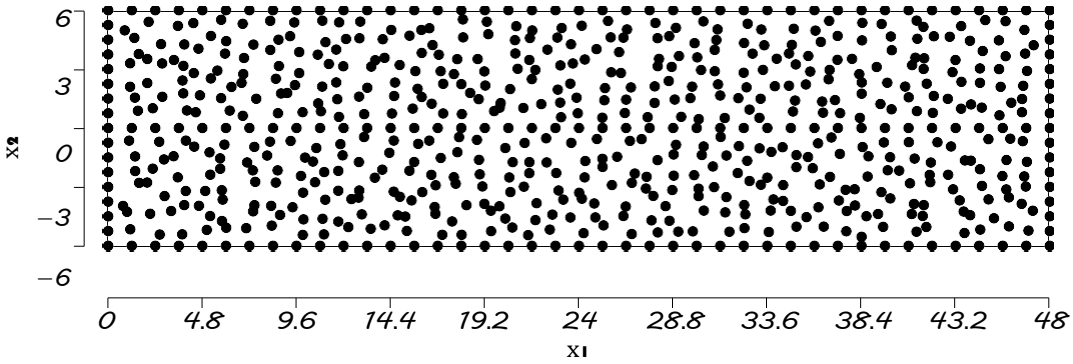

(b) 697 nodes with $c_n = 0.4$

Figure 6.13 – Nodal distributions of the cantilever beam, discretization (5×11 = 55, and 41×17 = 697 nodes) with level-1 of irregularity in configuration A.

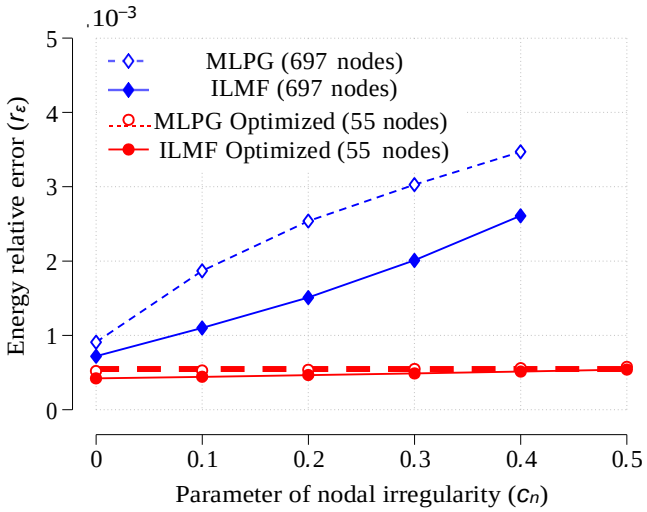

Figure 6.14 – Energy relative error of ILMF and MLPG as a function of the irregularity parameter c_n, obtained for the irregular discretization of the cantilever beam.

6.1.4.2 - Multi-objective Optimization

The problem presented in Figure 6.1 is solved via ILMF optimization method with 700 variables, the CPU time required was 350 sg. This multi-objective optimization process has the ability to discretized automatically by defining the number of nodes, nodal position and parameters size. Figure 6.15 shows the pareto results obtained for this problem.

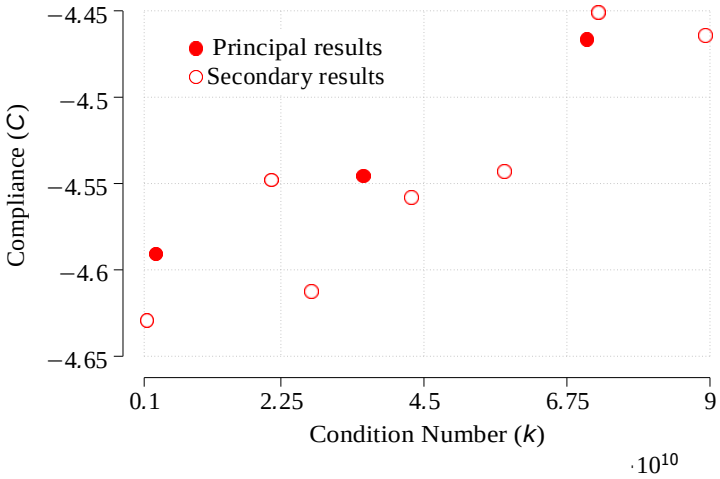

Figure 6.15 – The multi-objective Pareto front for irregular distribution of the cantilever beam discretization, obtained with the automatic optimization routine.

Each point of Figure 6.15 represents a different discretization for the problem. Three solutions are considered satisfactory to verify the automatic discretization process. Thus, three point at the beginning, middle and end are chosen from the solution cloud. Table 6.1 presents the main characteristics of the three chosen solutions.

Table 6.1 – The multi-objective Pareto front principal results for the cantilever beam, obtained with the automatic optimization routine.

C	k	$N_{x_1} \times N_{x_2} = N$	a_q	a_s
-4.5907	2.8528×10^9	5×4 = 20	0.4998	3.0713
-4.5455	3.5456×10^{10}	9×5 = 45	0.5003	4.5980
-4.4666	7.0647×10^{10}	15×9 = 135	0.4985	5.0665

In order to evaluate the relation between the parameteres Condition Number (k) and Compliance (C) with the number of nodes (N), it was plotted a graph (Figure 6.16) with the Table 6.1 data.

Evaluating the Figure 6.16, it is easy to see that the k is directly proportional to N. In the other hand, the C variable remains practically constant, i.e., there is no great difference between the nodes 20 and 135, respectively.

The problem shown in Figure 6.1 is seen as a benchmark test to evaluate the accuracy and efficiency of the ILMF multi-objective optimization process with 379 variables, the CPU time

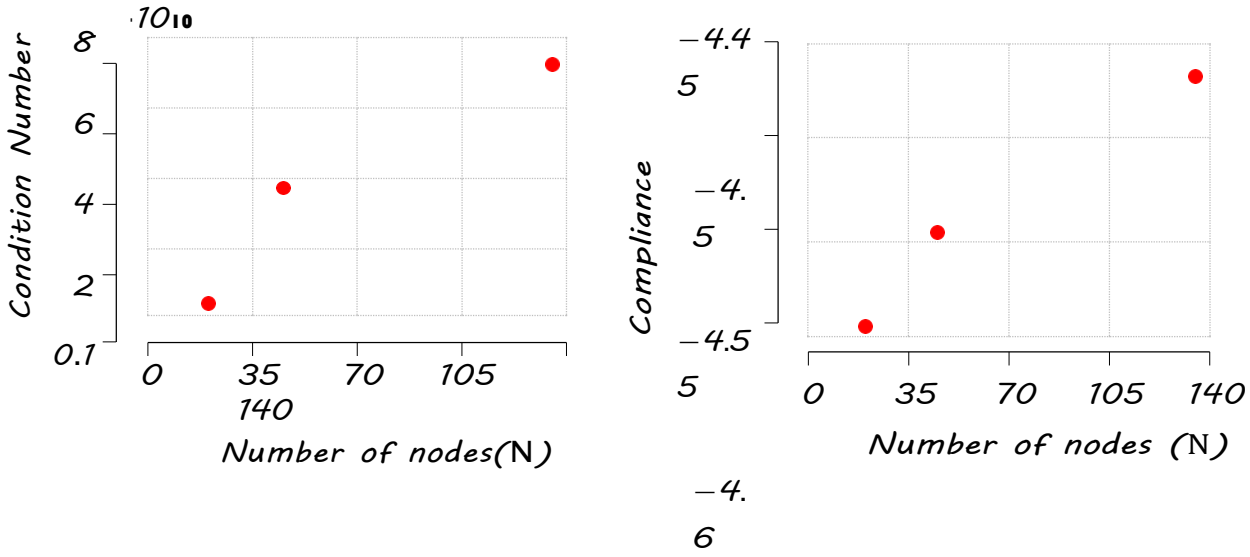

Figure 6.16 – Condition number (k) and Compliance (C) as a function of the number of nodes (N), carried out for three different optimization discretization of cantilever beam.

required was 212 sg. The discretization is showed in figure 6.17 for each one of the principal solution presented in the Figure 6.15 .

Analyzing Figure 6.17, it can be noticed that each one of the principal results presents different nodal discretizations and number of nodes. The nodal distribution presents smooth irregularity with good agreement with the previous results obtained for the irregularity nodal discretization. The red marks is going to be used to calculated the displacements and stress for the problem, presented sequentially.

In Figure 6.18 the principal results for the vertical displacement, and stress ($\sigma 11$ and $\sigma 12$) are presented. In general, It can be perceived that there is a good agreement with the analytical results. The discretizations with the 20 nodes has the same behavior as the analytical solution; however, the accuracy is smaller comparing with the results from the 45 and 135 nodes for the stress.

To evaluate the results and compared it with the analytical solution of the problem, the relative errors are plotted in the Figure 6.19. It presents the errors values related to energy and displacement, and it confirms what was already predicted by the previous Figures 6.37 and 6.38. The errors related to energy and displacement are small, in the order of 10^{-3}. For both cases the error decreases with increasing the number of nodes, which shows the accuracy of the results.

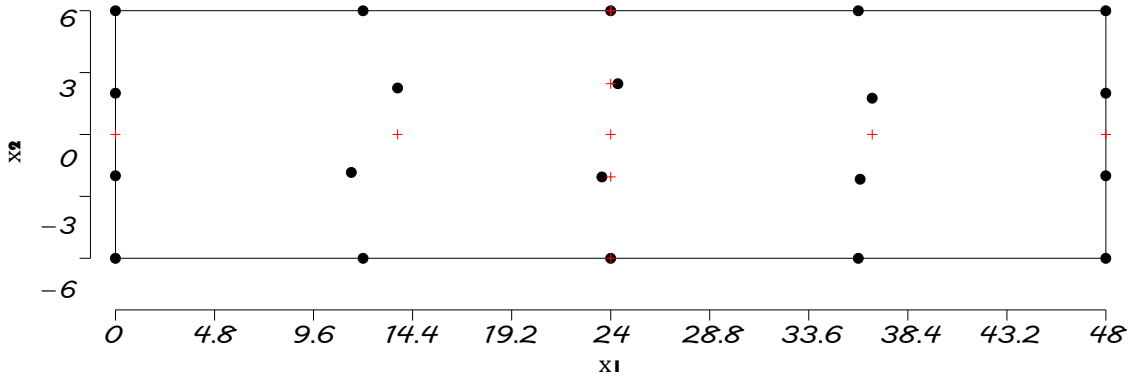

(a) 20 nodes

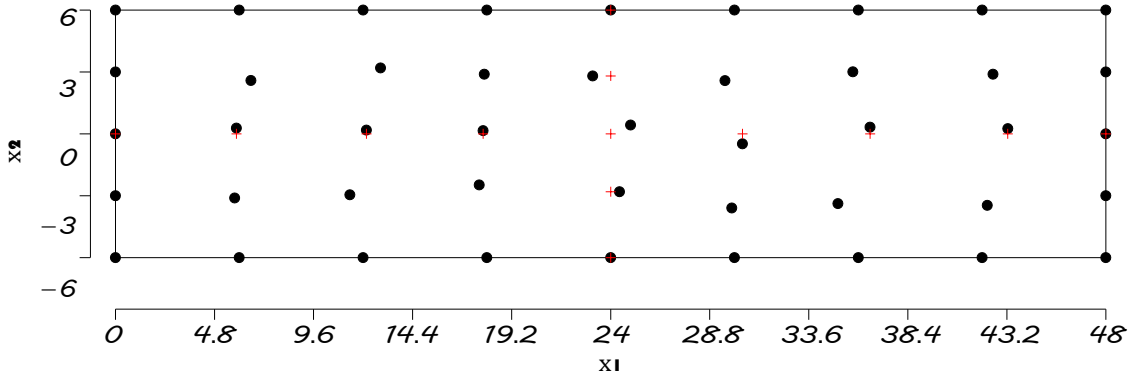

(b) 45 nodes

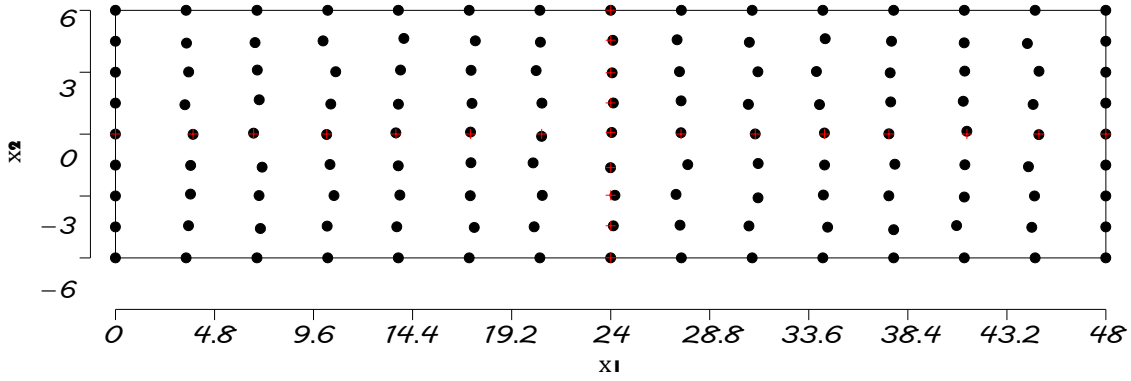

(c) 135 nodes

Figure 6.17 – Nodal distributions of the cantilever beam, discretization (5×4 = 20, 9×5 = 45 and 15×9 = 135 nodes) with level-2 of irregularity; in configuration A.

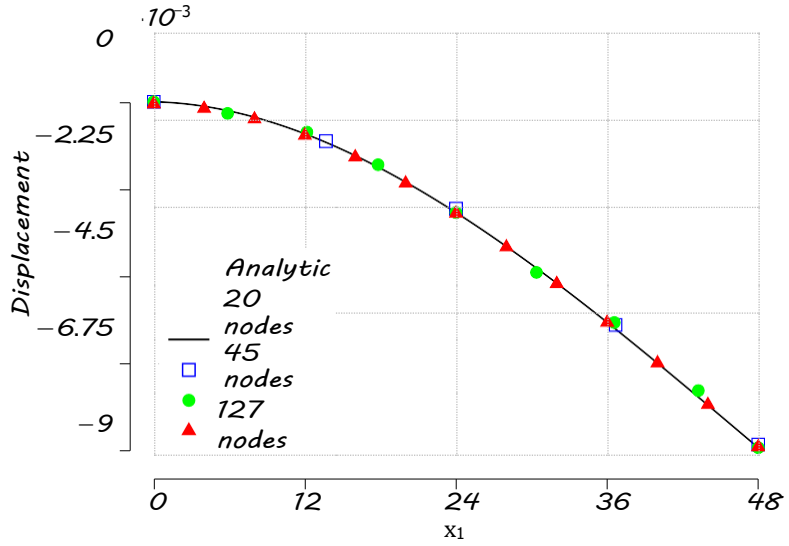

(a) Vertical displacement

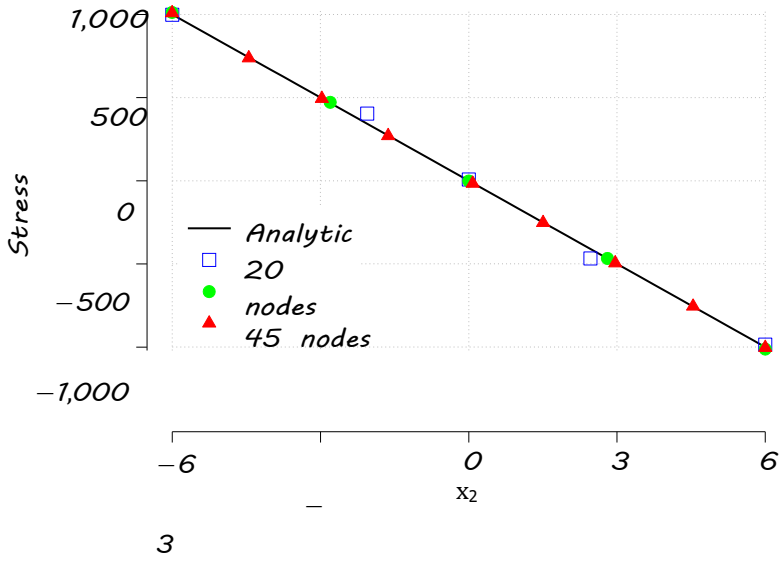

(b) stress (σ11)

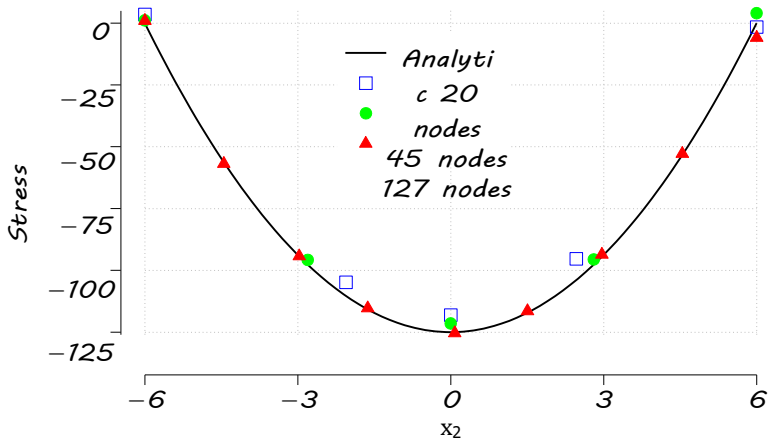

(c) stress (σ12)

Figure 6.18 – Principal displacement and stress for the cantilever beam with three different irregular nodal discretization, obtained by the automatic optimization routine.

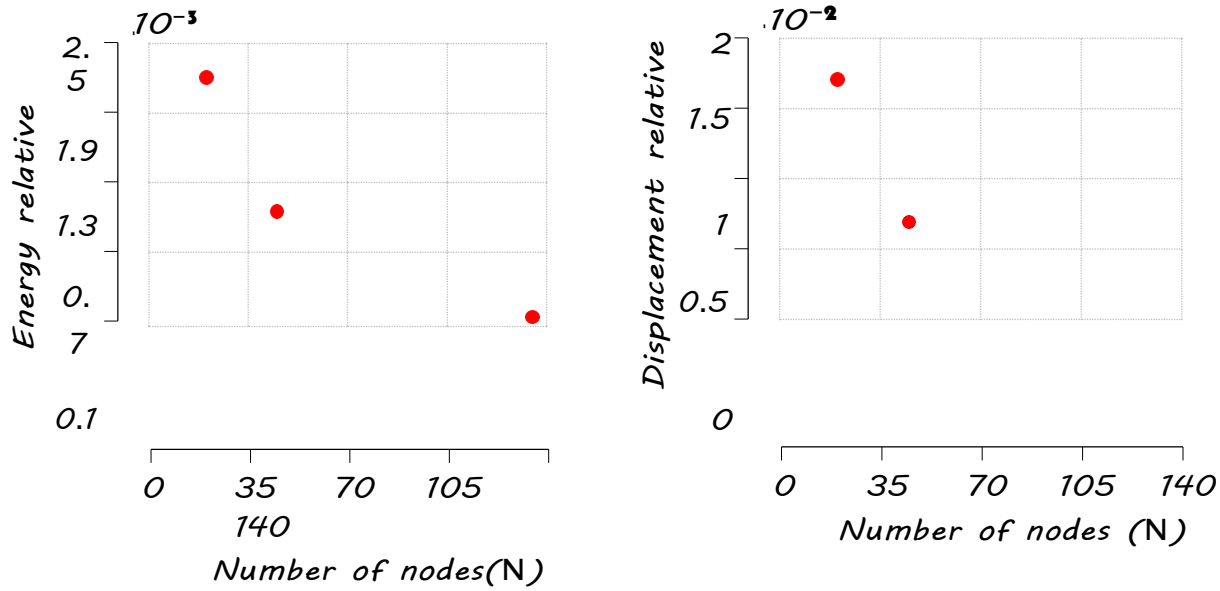

Figure 6.19 – Nodal distributions of the beam discretization with 20, 45 and 135 nodes with level-2 of irregularity; in configuration A.

6.2 - CIRCULAR CYLINDER

This example considered a long hollow cylinder shown in Figure 6.20, which is subjected to an internal pressure (Pi) and external pressure (Po). The inner and outer radios of the cylinder are denoted as (a) and (b), respectively. Due to the symmetry of the problem, only a portion of the upper right quadrant of the circular cylinder is considered for the analysis. The modeled section of the cylinder has two radius a = 5, with b = 25. Material properties of plate with a circular hole are taken as Young's modulus $E = 3.0 \times 10^7$ and the Poisson's ratio $\upsilon = 0.3$.

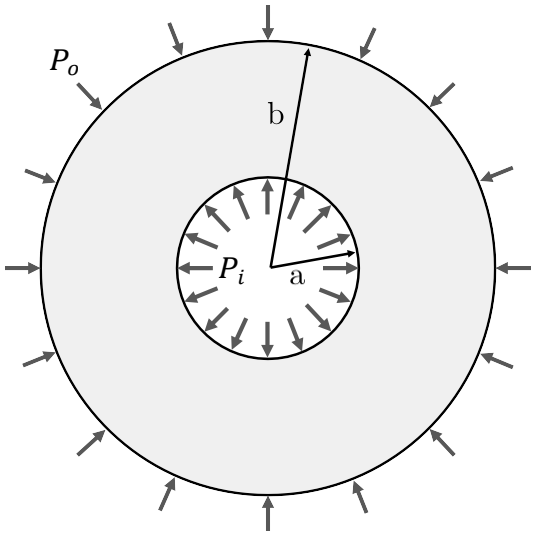

Figure 6.20 – Circular cylinder with internal and external pressure.

6.2.1 - Internal pressure

This special case is often encountered when dealing with stresses in piping systems or pressure vessels. A portion of the upper right quadrant of the circular cylinder used to solved this problem is presented in Figure 6.21.

A plane-stress state is considered which leads to the following displacements

$$\begin{Bmatrix} u_r(r) \\ u_\theta \end{Bmatrix} = \begin{Bmatrix} \frac{a^2 P_i}{Er(b^2-a^2)} [b^2(1+\upsilon) + r^2(1-\upsilon)] \\ 0 \end{Bmatrix} \tag{6.9}$$

The exact stress distribution in the plate is given by

$$\begin{Bmatrix} \sigma_{rr}(r) \\ \sigma^{\theta\theta}(r) \\ \tau_{r\theta} \end{Bmatrix} = \begin{Bmatrix} \frac{a^2 P_i}{(b^2-a^2)} [1 - \frac{b^2}{r^2}] \\ \frac{a^2 P_i}{(b^2-a^2)} [1 + \frac{b^2}{r^2}] \\ 0 \end{Bmatrix} \tag{6.10}$$

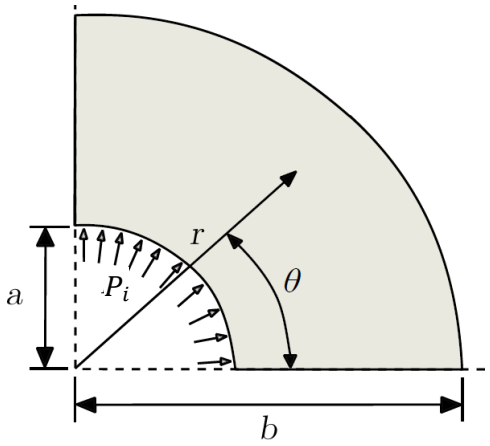

Figure 6.21 – Circular cylinder with internal pressure.

The problem presented in Figure 6.21 was solved using the ILMF optimization method, carried out with 1000 variables, the CPU time required was 1442 sg. Figure 6.22 shows the pareto results obtained for this problem.

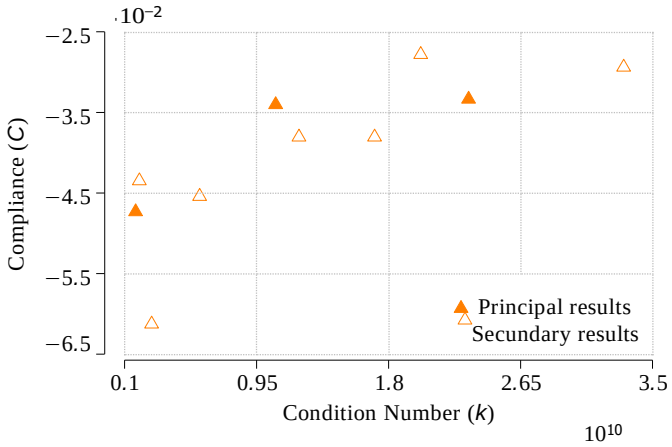

Figure 6.22 – The multi-objective Pareto front for irregular distribution of the circular cylinder discretizations with internal pressure, obtained with the automatic optimization routine.

Each point of figure 6.22 represents a different discretization for the problem. Three principal solutions were considered satisfactory to verify the uniqueness of each proposed discretization. Thus, from the solution cloud was chosen points at the beginning, middle and end. Main characteristics of the three chosen solutions are summarized in Table 6.2.

In order to evaluate the relation between the parameters k and C, with N for this problem, it was plotted the data of Table 6.1 in Figure 6.23.

Evaluating figure 6.23, it is clear that the k is directly proportional to N. However, the C variable remains practically constant, i.e, there is no great difference between the nodes 48 and 176, respectively.

Table 6.2 – The multi-objective Pareto front principal results for the circular cylinder with internal pressure, obtained with the automatic optimization routine.

C	k	$N_r \times N_\theta = N$	a_q	a_s
-0.04736	1.7101×10^{9}	8×6 = 48	0.5923	3.8282
-0.03407	1.0729×10^{10}	11×8 = 88	0.49016	4.1035
-0.03383	2.3151×10^{10}	17×11 = 187	0.5577	4.4231

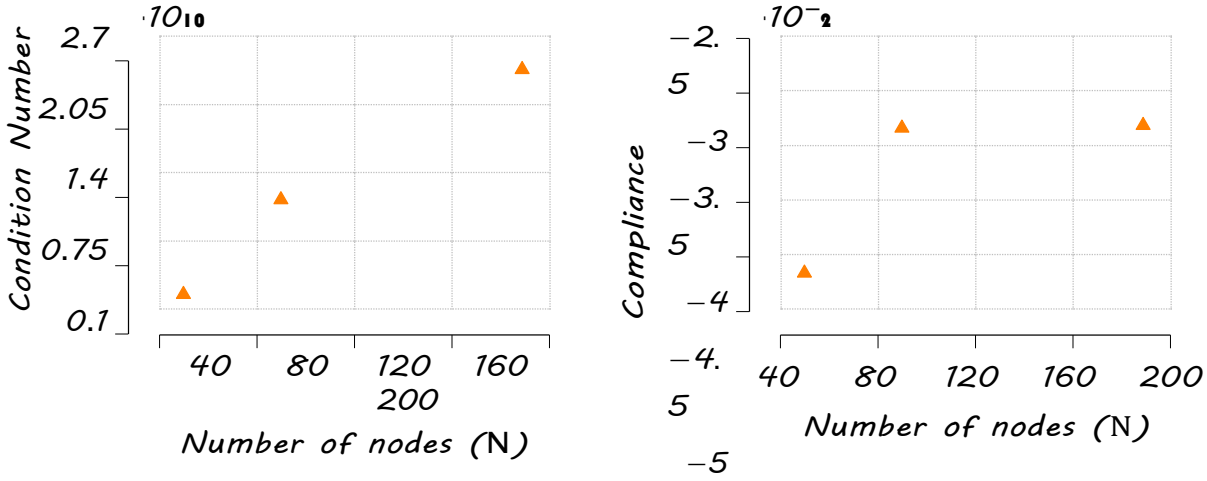

Figure 6.23 – Condition number (k) and Compliance (C) as a function of the number of nodes (N), carried out for three different optimization discretizations of circular cylinder with internal pressure.

ILMF multi-objective optimization process is evaluated the accuracy and efficiency by solving the problem shown in figure 6.19

Analyzing Figure 6.24, it can be noticed that which graph presents different nodal discretizations and number of nodes. The nodal distribution presents smooth irregularity with good agreement with the previous results showed in the nodal irregularity distribution. The red marks are going to be used to calculate the displacements and stresses for the problem, presented sequentially.

In Figure 6.25 are presented the principal numerical results for the radial displacement and stress in both directions, radial and angular for three discretizations. In addition, it contain its the analytical solution. It can be perceived that there is a good agreement, in general.

To evaluate and compare the results with the analytical solution of the problem, the relative errors are plotted in the Figure 6.26. The Figure presents the displacement and energy errors, it confirms what was already predicted by the previous Figures 6.24 and 6.25. The errors related to energy and displacement are expressively small, in the order of 10^{-2}. For both cases the error decreases with increasing the number of nodes, and shows the accuracy of the results.

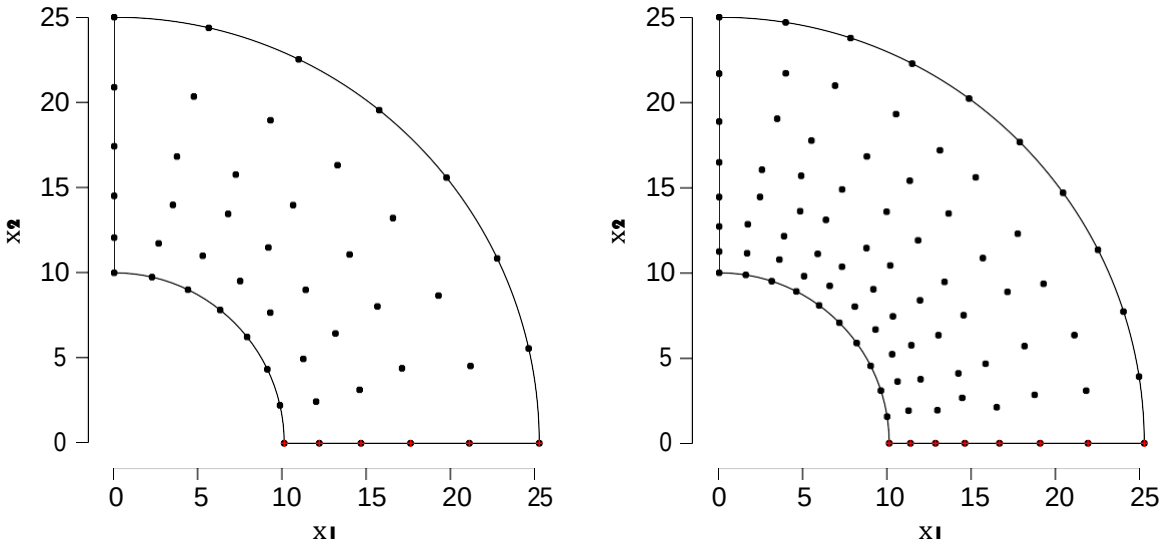

(a) *48* nodes

(b) *88* nodes

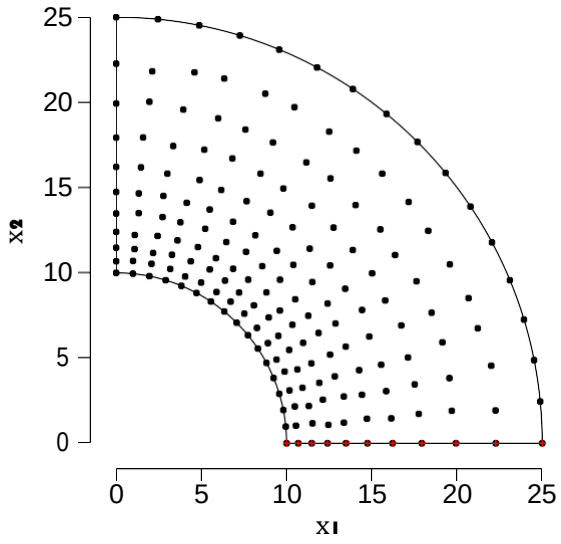

(c) *187* nodes

Figure 6.24 – Nodal distributions of the circular cylinder with external pressure, discretization (8×6 = 48, 11×8 = 88 and 17×11 = 187 nodes) with level-2 of irregularity; in configuration A.

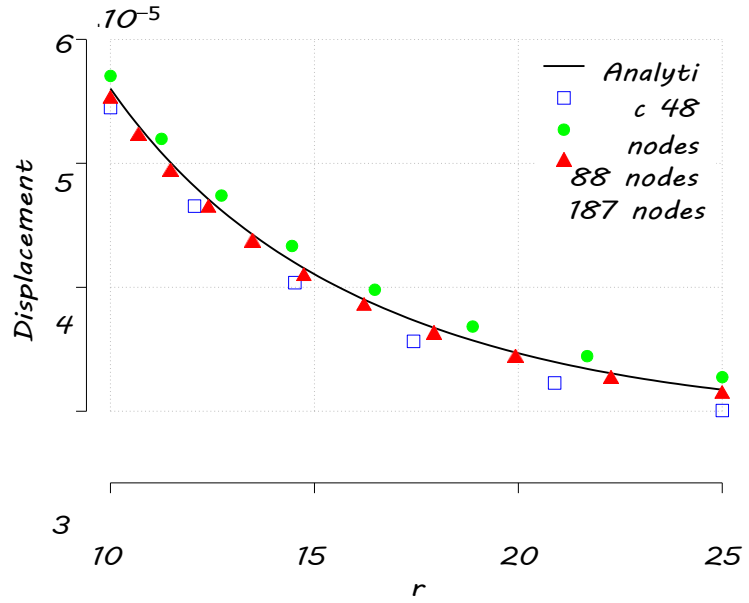

(a) Radial displacement

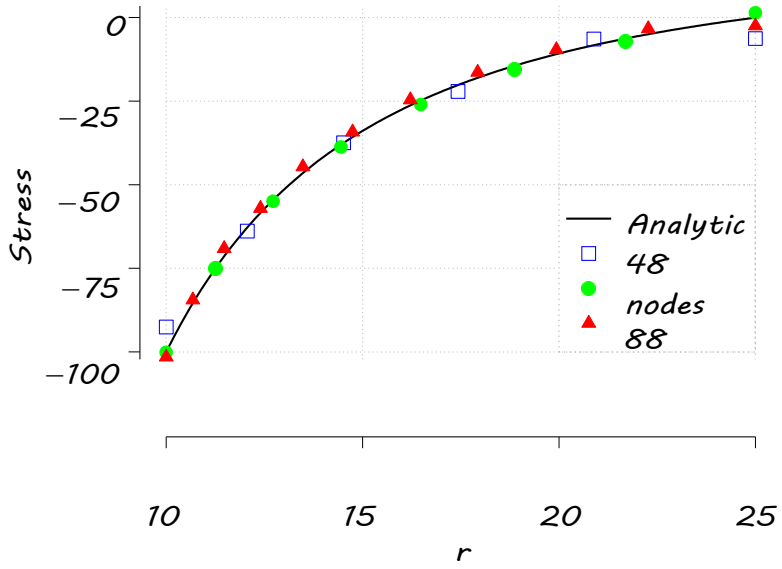

(b) Radial stress

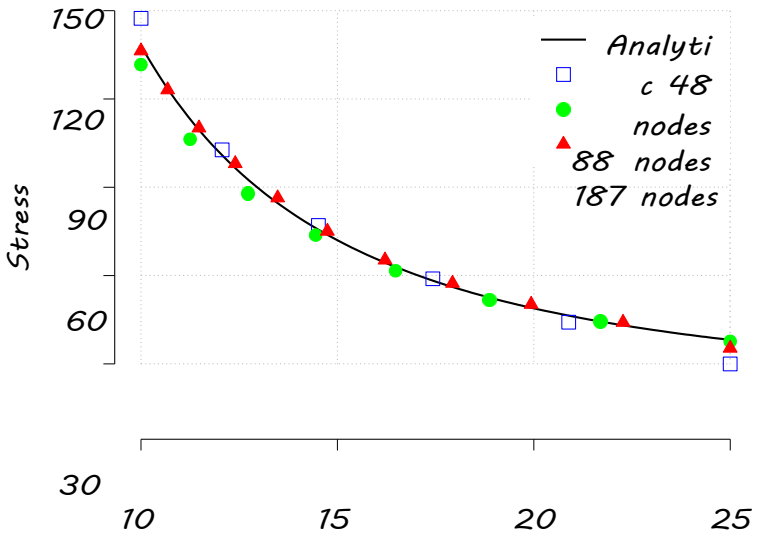

r

(c) Angular stress

Figure 6.25 – Principal displacement and stress for the circular cylinder with internal pressure carried out for three different irregular nodal discretizations, obtained by the automatic optimization routine.

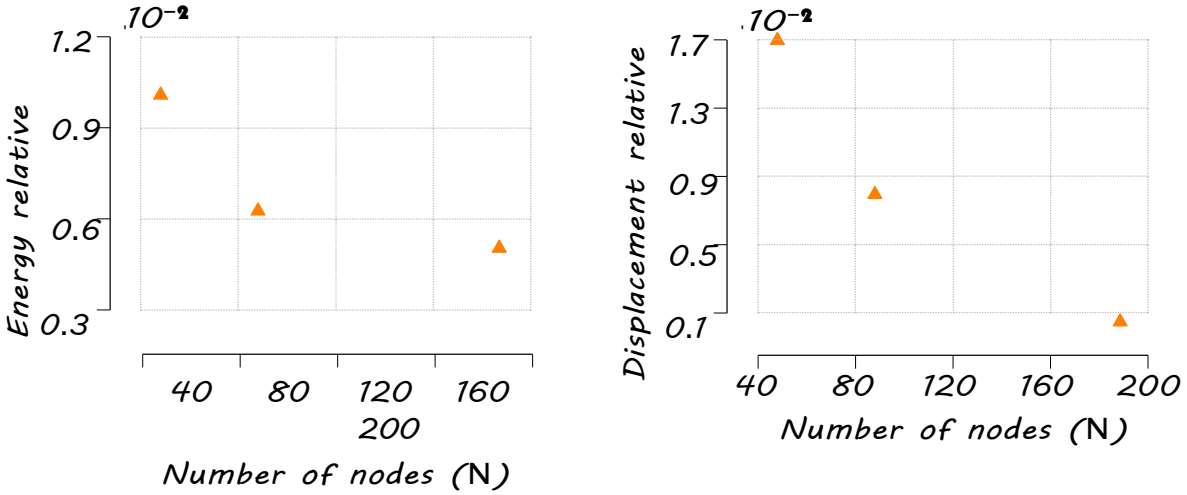

Figure 6.26 – Analysis of the influence of the number of nodes (N) on Condition number (k) and Compliance (C), carried out for three different optimization discretization.

6.2.2 - External pressure

When external pressure is applied to a cylindrical shell, the problem of buckling should also be considered. A portion of the upper right quadrant of the circular cylinder use for the analysis of this problem is presented in the Figure 6.27.

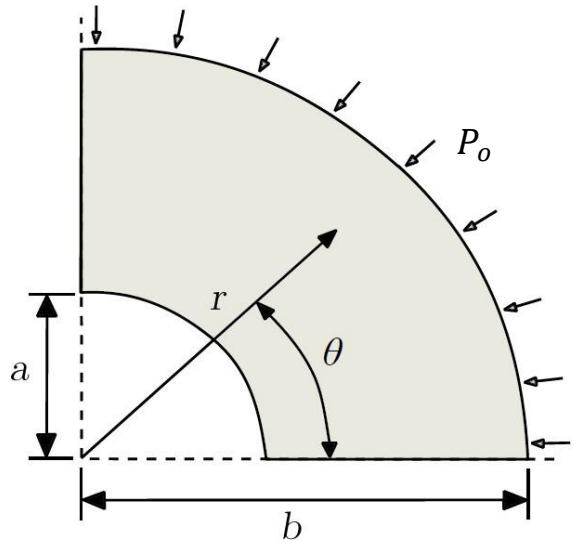

Figure 6.27 – Circular cylinder with internal pressure.

A plane-stress state is considered which leads to the following displacements

$$\begin{Bmatrix} u_r(r) \\ u_\theta \end{Bmatrix} = \begin{Bmatrix} -\frac{b^2 P_o}{Er(b^2-a^2)}\left[a^2(1+\upsilon)+r^2(1-\upsilon)\right] \\ 0 \end{Bmatrix} \tag{6.11}$$

The exact stress distribution in the plate is given by

$$\begin{bmatrix} \sigma_{rr}(r) \\ \sigma^{\theta\theta}(r) \\ \tau_{r\theta} \end{bmatrix} = \begin{bmatrix} \frac{b^2 P_o}{(b^2-a^2)}\left[\frac{a^2}{r^2}-1\right] \\ \frac{a^2 P_o}{(b^2-a^2)}\left[\frac{a^2}{r^2}+1\right] \\ 0 \end{bmatrix} \tag{6.12}$$

The problem presented in Figure 6.27 was solved via ILMF optimization method. This multi-objective optimization process defines automatically the discretization, Figure 6.28 shows the pareto results obtained for this problem, carried out with 498 variables.

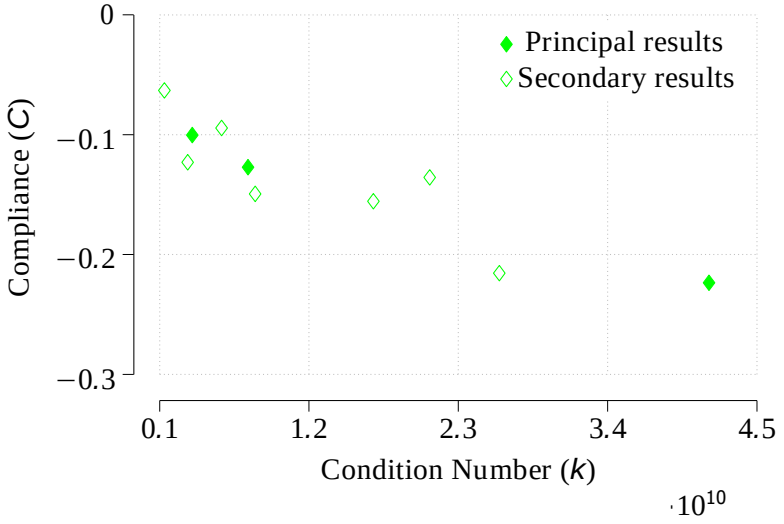

Figure 6.28 – The multi-objective Pareto front for irregular distribution of the circular cyliner discretization with external pressure, obtained with the automatic optimization routine.

Each point of Figure 6.28 represents a different discretization for the problem. Three principal solutions was considered satisfactory to verify the uniqueness of each proposed discretization. In the Table 6.3 is presented the main characteristics of the three chosen solutions.

Table 6.3 – The multi-objective Pareto front principal results for the circular cylinder with external pressure, obtained with the automatic optimization routine.

C	k	$N_r \times N_\theta = N$	a_q	a_s
-0.1002	3.4126×10^9	$8 \times 7 = 56$	0.5123	4.408
-0.1270	7.5207×10^{10}	$11 \times 8 = 88$	0.4802	4.6743
-0.2285	2.5818×10^{10}	$19 \times 12 = 228$	0.5106	4.6661

In order to evaluate the relation between the parameteres k and C and N, it was plotted a graph with this data in the figure 6.29.

Evaluating Figure 6.29, it is clear that the k is directly proportional to N. The Compliance

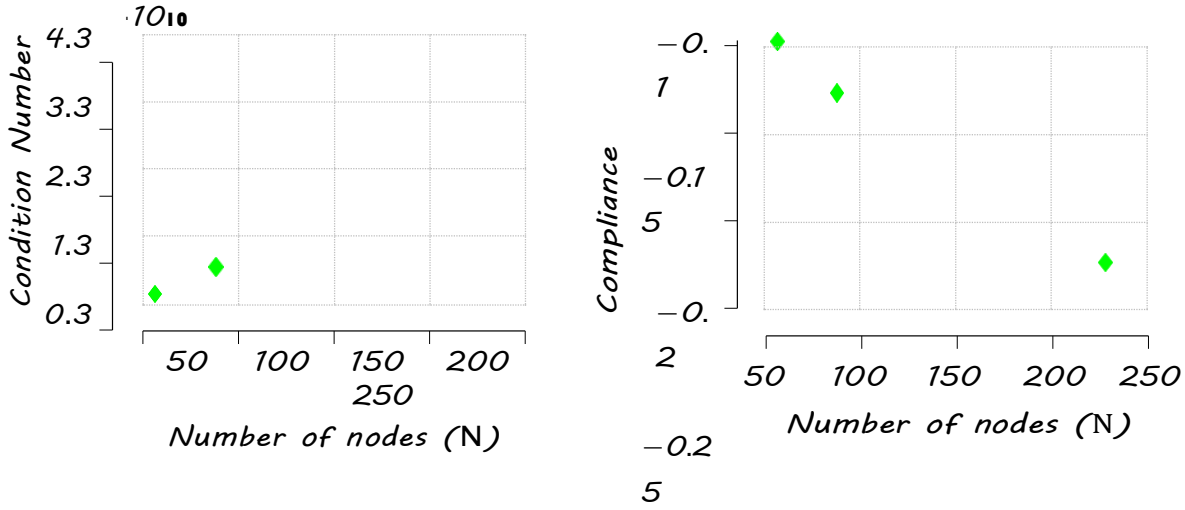

Figure 6.29 – Condition number (k) and Compliance (C) as a function of the number of nodes (N), carried out for three different optimization discretization of circular cylinder with external pressure.

variable remains practically constant, there is no great difference between the nodes 56 and 228, respectively.

The problem shown in figure 6.27 is seen as a benchmark test to evaluate the accuracy and efficiency of the ILMF multi-objective optimization process. In order to solve the problem, it was applied the ILMF. The solution is plotted in Figure 6.30 for each one of the selected point.

Figure 6.31 presented the principal results for the radial displacement, and radial and angular stresses; which shows the greater difference between the analytical and numerical solution for the 56 nodes. It can be perceived that there is a good agreement, in general.

To evaluate and compare the results with the analytical solution of the problem, the relative errors are plotted in the Figure 6.32.

The Figure 6.32 presents the errors values related to energy and displacement and it confirms what was already predicted by the previous Figures 6.31. The errors related to energy and displacement are expressively small, in the order of 10^{-2}. For both cases the error decreases with increasing number of nodes and shows the accuracy of the results.

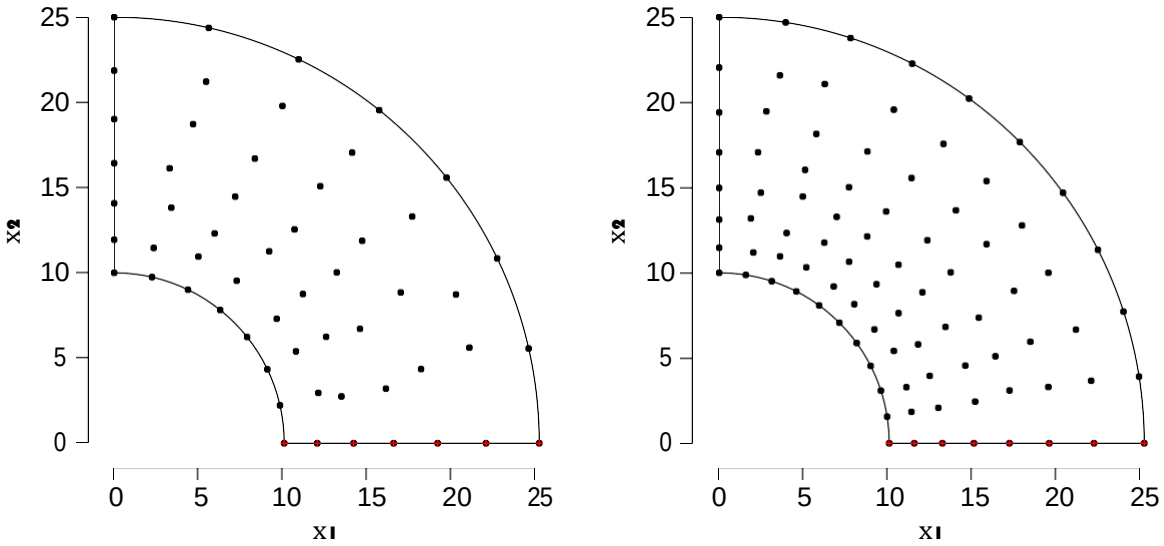

(a) 56 nodes

(b) 88 nodes

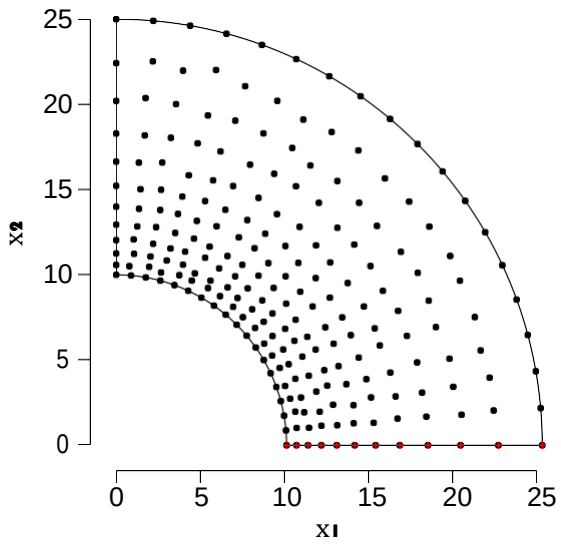

(c) 228 nodes

Figure 6.30 – Nodal distributions of the circular cylinder with external pressure, discretization (8×7 = 56, 11×8 = 88 and 19×12 = 228 nodes) with level-2 of irregularity; in configuration A.

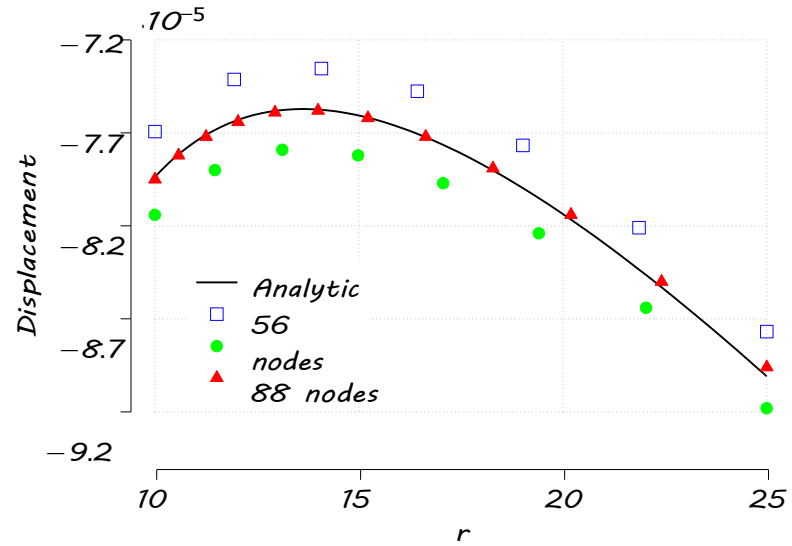

(a) Radial displacement

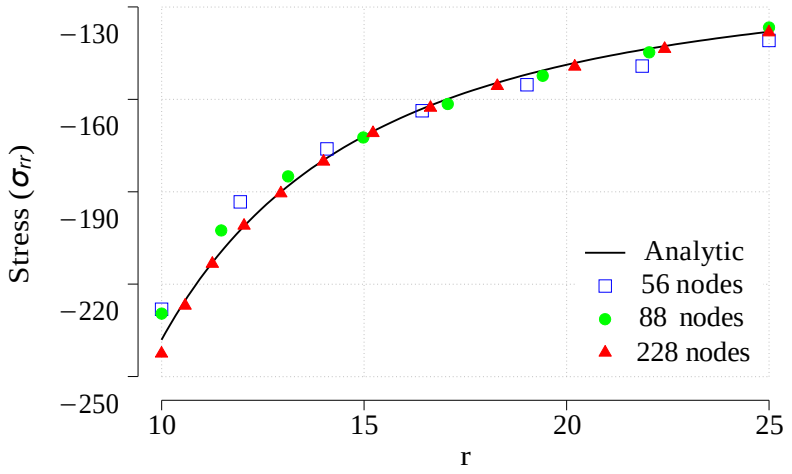

(b) Radial stress

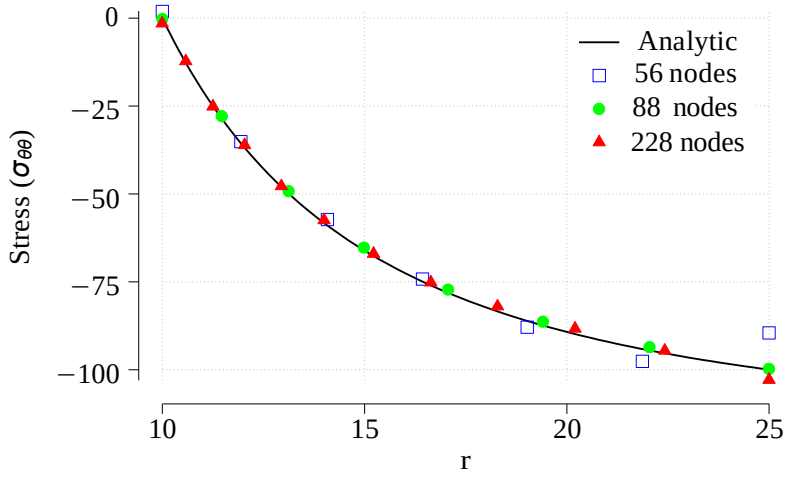

(c) Angular stress

Figure 6.31 – Principal displacement and stress for the circular cylinder with external pressure carried out for three different irregular nodal discretization, obtained by the automatic optimization routine.

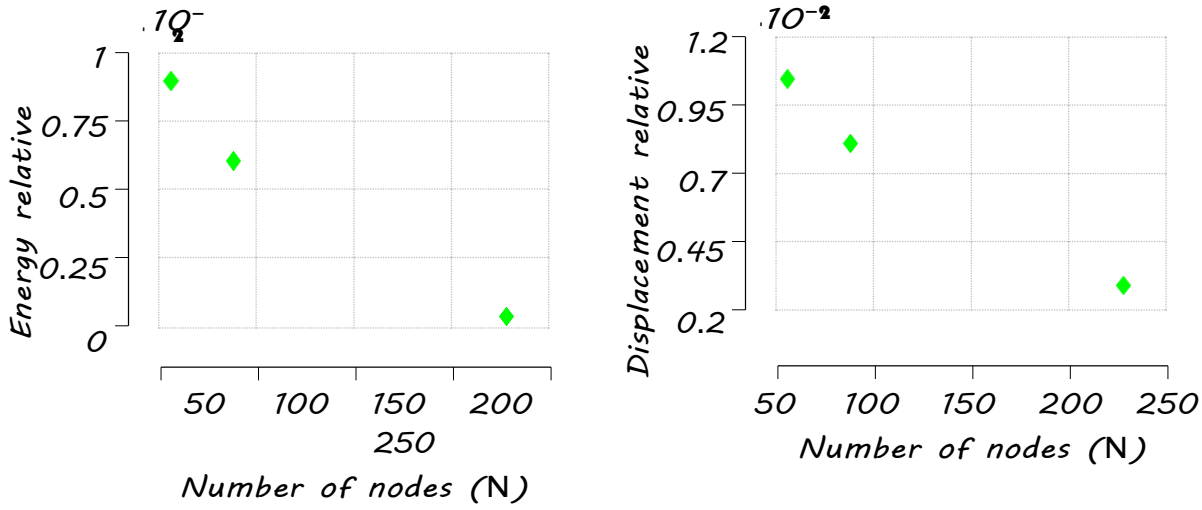

Figure 6.32 – Analysis of influence of the number of nodes (N) on Condition number (k) and Compliance (C), carried out for three different optimization discretization.

6.3 - PLATE WITH A CIRCULAR HOLE

Consider an infinite plate with a centered circular hole under unidirectional unit tension along the x_1 direction, as represented in Figure 6.33. Due to the symmetry of the problem about the horizontal and vertical axes, only a portion of the upper right quadrant of the plate is considered. The modeled section of the plate has dimensions b x b and the center circle has a radius a = 1, with b = 5a. Material properties of plate with a circular hole are taken as Young's modulus $E = 1.0 \times 10^5$ and the Poisson's ratio $\nu = 0.25$.

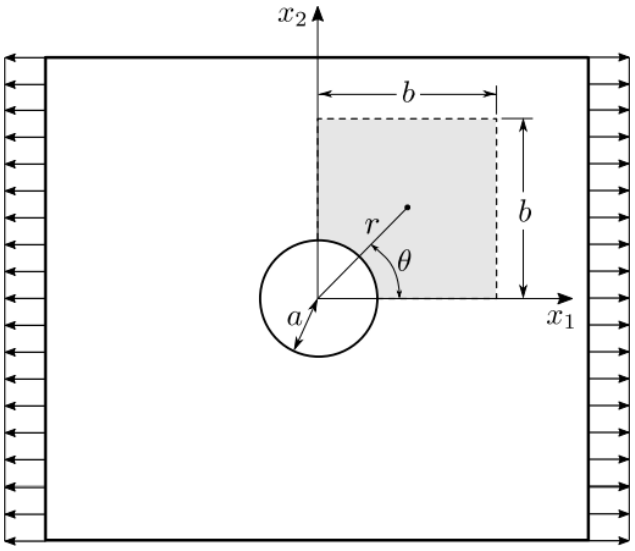

Figure 6.33 – Plate with a circular hole.

A plane-stress state is considered which leads to the following displacements

$$\begin{Bmatrix} u_1(r,\theta) \\ u_2(r,\theta) \end{Bmatrix} = \begin{matrix} -\frac{\cos\theta}{2r^3E}[4a^4\cos^2\theta\,(1+\nu)\,(1-r^2) - 3a^4(1+\nu) + (ar)^2(1-3\nu) - 2r^4] \\ -\frac{\sin\theta}{2r^3E}[4a^4\cos^2\theta\,(1+\nu)\,(1-r^2) - a^4(1+\nu) + (ar)^2(\nu-3) + 2r^4\nu] \end{matrix} \tag{6.13}$$

The exact stress distribution in the plate is given by

$$\begin{Bmatrix} \sigma_{11}(r,\theta) \\ \sigma_{22}(r,\theta) \\ \sigma_{12}(r,\theta) \end{Bmatrix} = \begin{matrix} 1 - \frac{a^2}{r^2}\left[\frac{3}{2}\cos 2\theta + \cos 4\theta\right] + \frac{3}{2}\frac{a^4}{r^4}\cos 4\theta \\ -\frac{a^2}{r^2}\left[\frac{1}{2}\cos 2\theta - \cos 4\theta\right] - \frac{3}{2}\frac{a^4}{r^4}\cos 4\theta \\ -\frac{a^2}{r^2}\left[\frac{1}{2}\sin 2\theta + \sin 4\theta\right] + \frac{3}{2}\frac{a^4}{r^4}\sin 4\theta \end{matrix} \tag{6.14}$$

where r and θ are the usual polar coordinates, centered at the center of the hole.

The bottom and left edges of the plate are assumed as kinematic boundaries, with displacements specified on the bottom $u_2(x_1,\ x_2 = 0)$ and left edges $(u_1(x_1 = 0,\ x_1 = L,\ x_2) = 0)$. The right and top edges are assumed as static boundaries, loaded by tractions computed from the stresses

of the exact solution equation (6.14) as $t_j = \sigma_{ij} n_i$, in which n_i represents the components of the unit outward normal to the edge of the plate.

The problem presented in Figure 6.33 was solved via ILMF optimization method. This multi-objective optimization process has the ability to automatically define the discretization determining the nodal distribution, parameters size and position of each node, the Figure 6.34 shows the pareto results obtained for this problem carried out with 674 variables .

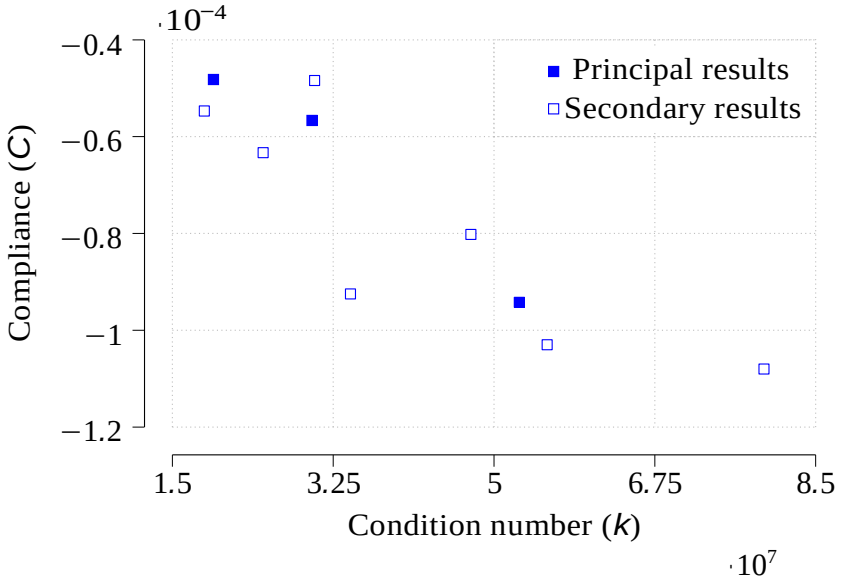

Figure 6.34 – The multi-objective Pareto front for irregular distribution of the plate with a circular hole discretization, obtained with the automatic optimization routine.

Each point of the figure 6.34 represents a different discretization for the problem solution. Three solutions was considered satisfactory to verify the uniqueness of each proposed discretization. In the Table 6.4 is presented the main characteristics of the three chosen solutions.

Table 6.4 – The multi-objective Pareto front with the principal results for the plate with circular hole, obtained with the automatic optimization routine.

C	k	$N_r \times N_\theta = N$	a_q	a_s
-4.8206 x 10^{-5}	1.9480×10^7	12×7 = 84	0.5027	4.1350
-5.6657 x 10^{-5}	3.0199×10^7	15×9 = 135	0.5393	4.6366
-9.4234 x 10^{-5}	5.2776×10^7	19×13 = 247	0.5010	4.7307

In order to evaluate the relation between the parameteres (k) and (C) (objective functions) and the number of nodes (N), a graph was plotted with this data in the Figure 6.35.

Evaluating the figure 6.35, it is clear that the (k) is directly proportional to N, the increase in the number of nodes generates a higher value of Conditional Number. However, the Compliance variable remains practically constant, there is no great difference between the nodes 84 and 247,

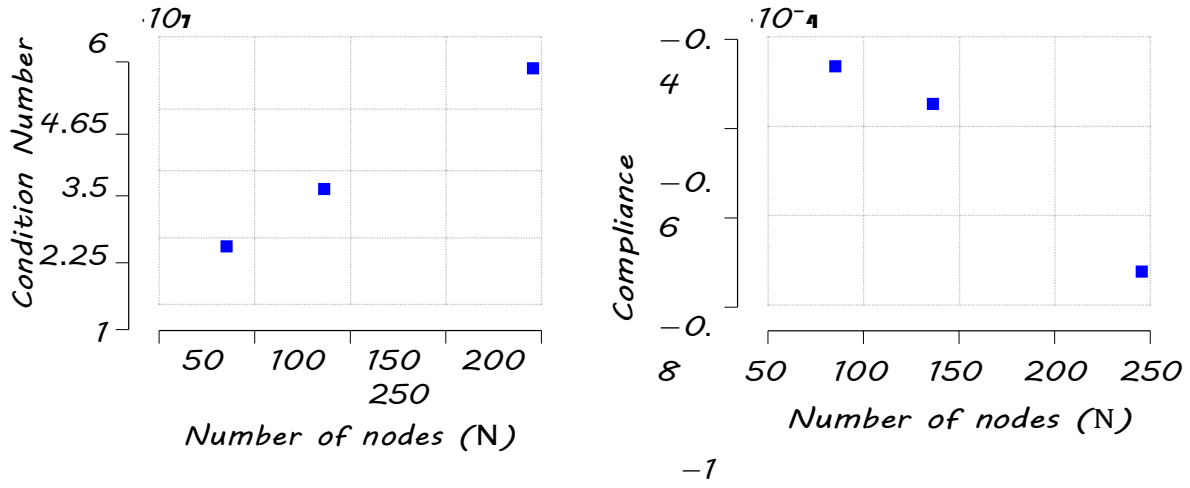

Figure 6.35 – Condition number (k) and Compliance (C) as a function of the number of nodes (N), carried out for three different optimization discretization of plate with circular hole.

respectively.

In order to solve the problem shown in the Figure 6.33, it was applied the ILMF. The solution is shown in the figure 6.36 for each one of the selected point.

Analyzing the Figure 6.36, it can be noticed that each graph presents different nodal discretizations and number of nodes. Again, the nodal distribution present smooth irregularity with good agreement with the previous results. The red marks are going to be used to calculate the displacements and stress for the problem, presented sequentially.

In the figure 6.37, there are presented the principal results for the displacement in the both directions, horizontal and vertical. In addition, it cointains the three discretizations and the analytical solution.

In the figure 6.37, it can be perceived that there is a good agreement, in general. The discretizations with the 84 nodes have the same behavior as the analytical solution, however there is a smaller accuracy than the results from the 135 and 247 nodes, in the vertical direction. It can be explained by the fact that the formulation is based on the optimized energy, and not in displacement.

In the figure 6.38, there are presented the principal results for the stress in three directions ($\theta = 0, \pi/4, \pi/2$). It can be perceived that there is a good agreement, in general. All discretizations have the same behavior as the analytical solution, however the results for the 84 nodes have a smaller accuracy of the results from the 135 and 247 nodes. It can occur because of the small number of nodes.

To evaluate the results and compare it with the analytical solution of the problem, the relative errors are plotted in the Figure 6.39.

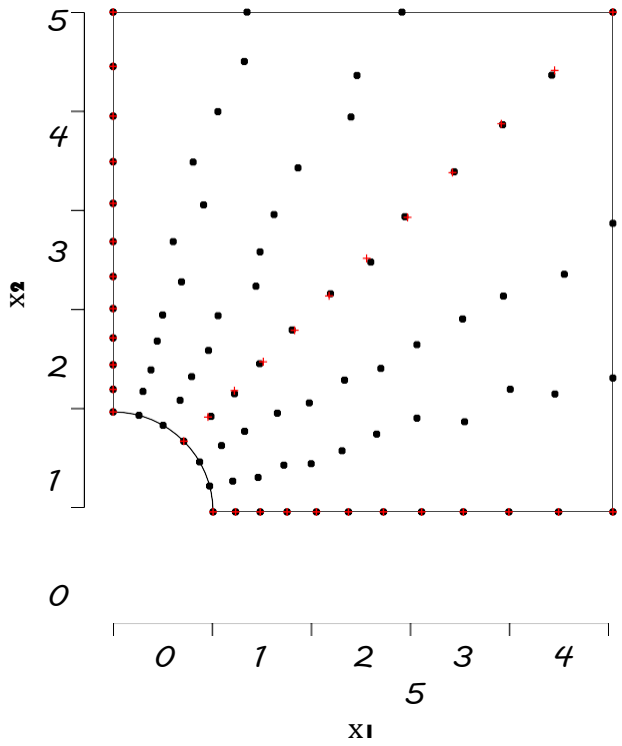

(a) 84 nodes

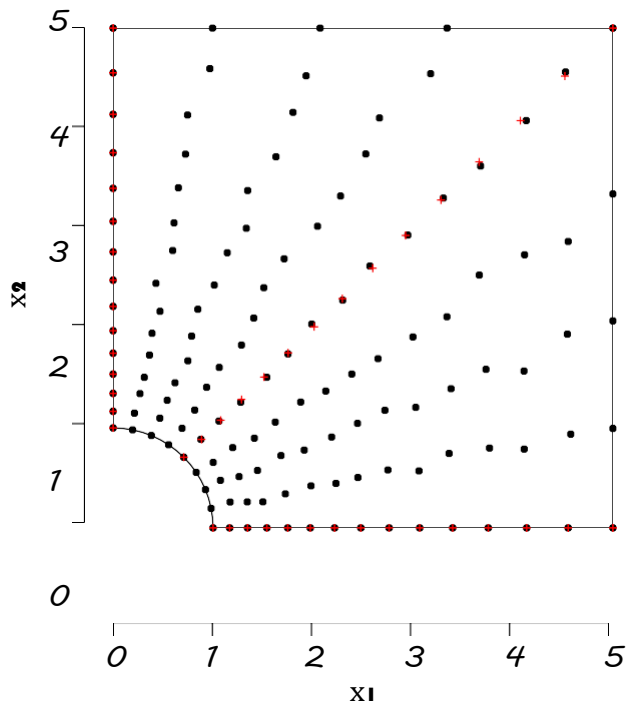

(b) 135 nodes

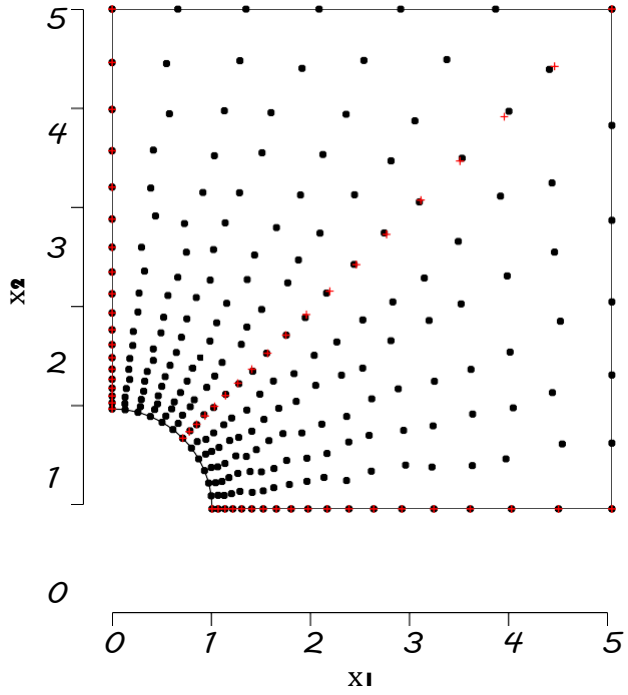

(c) 247 nodes

Figure 6.36 – Nodal distributions of the plate with a circular hole, discretization (12×7 = 84, 15×9 = 135 and 19×13 = 247 nodes) with level-2 of irregularity; in configuration A.

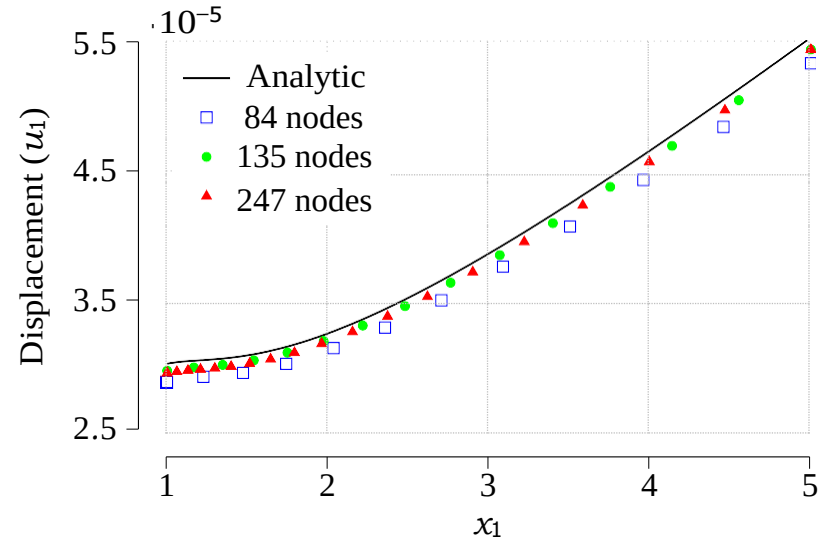

(a) $x_2 = 0$

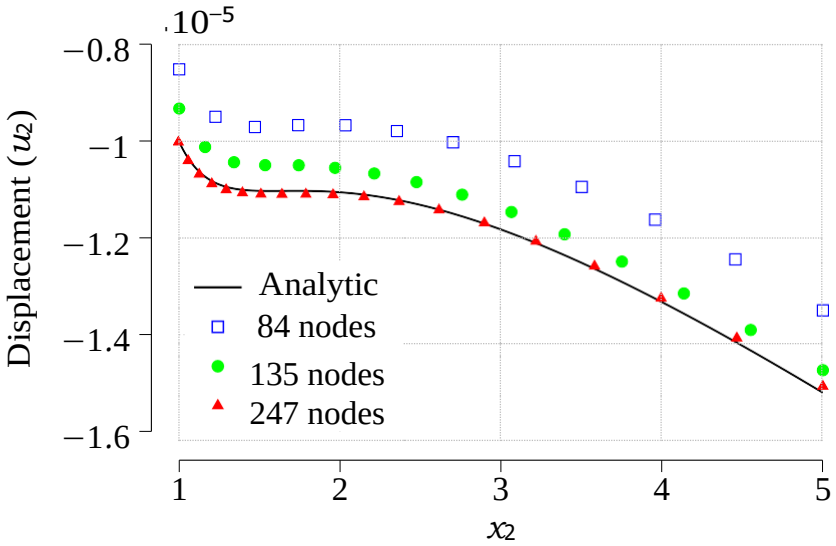

(b) for $x_1 = 0$

Figure 6.37 – Horizontal and vertical displacement of the plate with a circular hole, carried out for three different irregular nodal discretization, obtained by the automatic optimization routine.

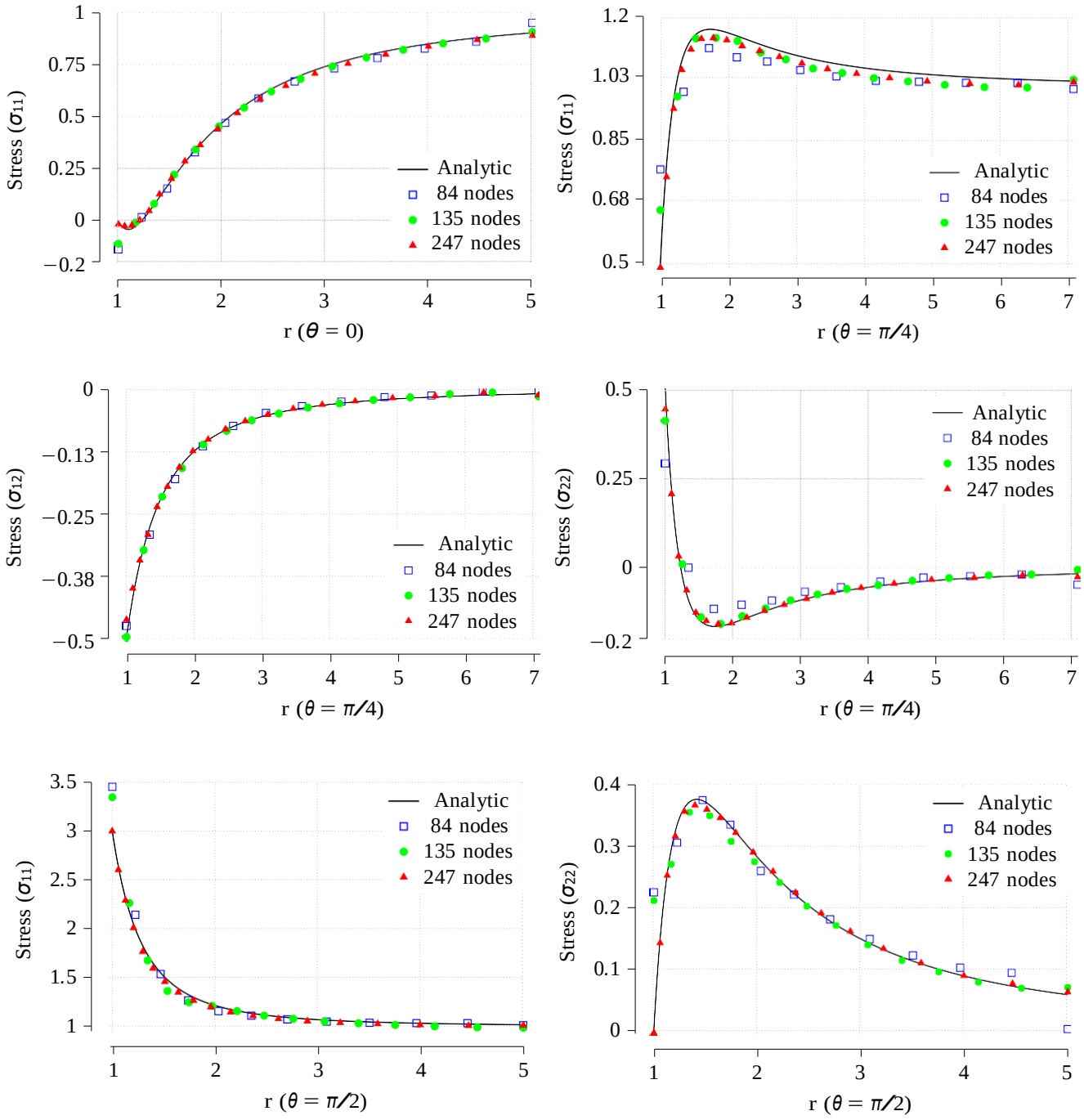

Figure 6.38 – Stress distribution of the plate with circular hole for $\theta = 0, \pi/4, \pi/2$, carried out for three different irregular nodal discretizations, obtained by the automatic optimization routine.

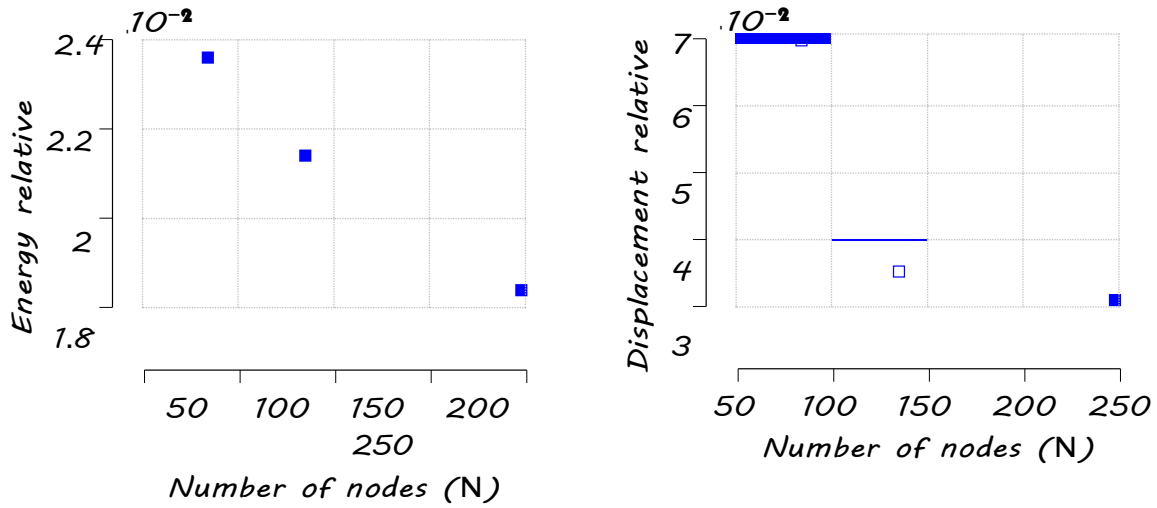

Figure 6.39 – Energy and displacement relative errors as a function of the number of nodes, carried out for three different optimization discretizations of plate with circular hole.

The Figure 6.39 presents the errors related to displacement and energy, it confirms what was already predicted by the previous Figures 6.37 and 6.38. The errors related to energy and displacement are expressively small, in the order of 10^{-2}. For both cases the error decreases with increasing number of nodes and shows the accuracy of the results.

6.4 - OBJETIVE FUNCTIONS

In order to evaluate the relation between the k and the N, it is plotted the Figure 6.40 with all the values of k for the four benchmark problems analyzed in this thesis.

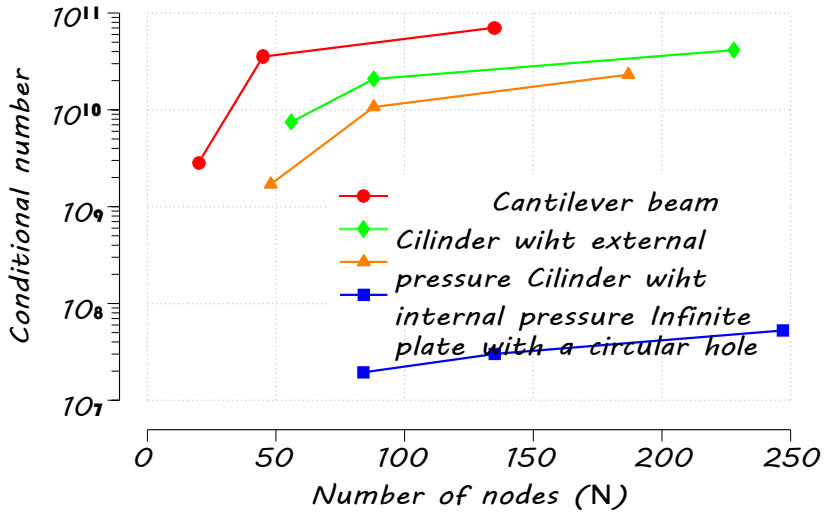

Figure 6.40 – Condition number (k) as a function of the number of nodes (N), carried out for different benchmark problems with automatic discretization.

It can be noticed in Figure 6.40, that the k is directly proportional to N. In addition, it

shows good agreement with the theory, making the function a good choice to this type of analyze; because, when the solution have a greater number of the nodes, the stiffness matrix size increases causing an increase in the conditional number.

In order to analyze the relation between the C and the N, it is plotted the Figure 6.41 with all the values of C for the four problems analyzed. According to Figure 6.41, it is possible

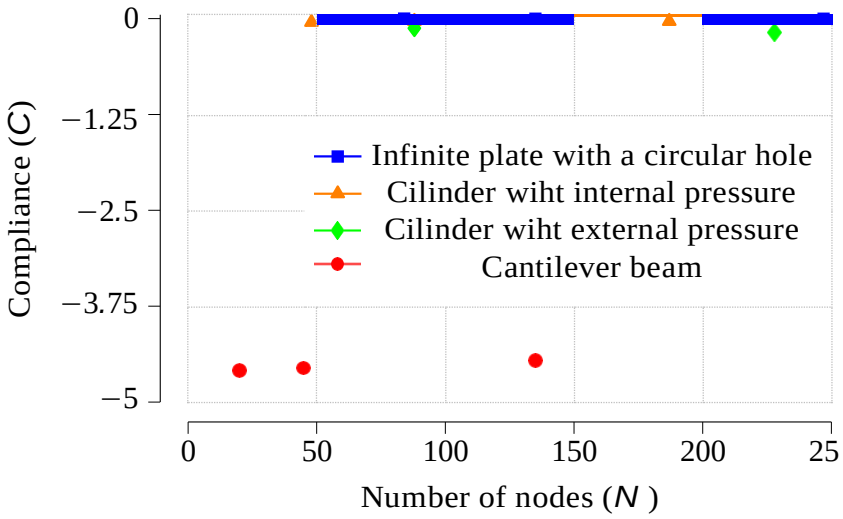

Figure 6.41 – Compliance (C) as a function of the number of nodes (N), carried out for different benchmark problems with automatic discretization.

to observe that the C value remains pratically constant with the increase N. The C variation related with the N is almost insignificant, hence it shows that is a excellent objetive function for the automatic discretization process.

7 - CONCLUSIONS

7.1 - GENERAL CONCLUSIONS

This thesis presents recent developments on a local mesh free numerical model (ILMF), for the solution of two-dimensional problems in elasticity and linear, carried out at the Department of Civil Engineering and Environment of the University of Brasília.

Derived from the work theorem, the model formulation leads to a weak form of the weighted residual statement of a statically admissible stress field, kinematically formulated with a simple rigid-body displacement. The discretization considers the MLS approximation and implements a reduced numerical integration. For each node of a nodal distribution, the equations of equilibrium are computed with a reduced numerical integration scheme that considers a total of 4 integration points, with 1 point per segment of the respective local domain of integration. Assuming a linear variation of tractions, along each boundary segment of the local domain, the local form of equilibrium can be exactly evaluated with 1 quadrature point, centered on each segment, thus leading to a point-wise discrete form that improves the computational efficiency. The reduced integration of the model induces a reduction of the stiffness associated with the local node, which means an increase of the strain energy, and, consequently leads to an increase of the solution accuracy with no instabilities at all. Hence, instability is not an issue of this model, in contrast to other methods that use nodal integration without stabilization. As a consequence of this strategy, this model, symbolically referred to as ILMF, an acronym that stands for Integrated Local Mesh Free method, is computationally much more efficient than other numerical methods that use standard numerical quadrature, as shown by numerical results.

Both regular and irregular nodal distributions can be considered by the ILMF model. For each node of a nodal distribution, the size of the compact support and the size of the local integration domain are very important discretization parameters in the analysis that affect the performance of the solution, as a direct consequence of the pattern of the nodal distribution. Results obtained with the ILMF model, for severe irregularities of the nodal distribution, show a high level of accuracy, which makes ILMF a robust and very reliable mesh free numerical model.

An important feature of the ILMF model is the automatic definition of the discretization parameters and the nodal distribution, through a multi-objective optimization process based on genetic algorithms. The size of the compact support and the size of the local domain, of each node, as well as the nodal distribution, are defined using two convenient objective functions,

one of them derived from the classical structural theorem of the minimum total potential energy and the other using of the condition number of the stiffness matrix. This optimization scheme led to an excellent accuracy of results, with local Pareto-optimal results always very close to the global Pareto-optimal solutions, as presented in numerical results.

The automatic discretization is an essential feature of any efficient numerical method. The results obtained in this work are in perfect agreement with the available analytical solutions. Therefore, the high level of accuracy and stability analysis of the ILMF model carried out with an automatic multi-objective optimization process make this a great tool that will improve the structural analysis process.

7.2 - FUTURE WORKS

Meshfree methods have been applied in almost all areas of structural and fracture mechanics; still, it is known that there are challenges in developing computationally efficient algorithms, with accurate integration techniques that can overcome the issue of the computational cost. The remarkable accuracy of the results with extremely fast computations, make it possible to apply the ILMF model in the case of nonlinear problems. ILMF can become an important tool in computational nonlinear solid mechanics, especially for solving problems with severe distortion, discontinuities and moving boundaries.

Local formulations of meshfree methods use a solution paradigm based in the node-by-node calculation to generate the rows of the global system of equations, in contrast to global formulations. Meshfree methods have been commonly applied as a computer simulation method to solve a wide range of problems in a variety of practical fields, such as mechanical, aerospace, nuclear, chemical and civil engineering. Implementation of meshfree methods in CAD systems on the basis of modern computers allows the solution of large-scale problems. Therefore, the introduction of parallel processing, a fast-growing direction of research, is able to give the most significant result in terms of saving time designing and modeling. Local formulations of meshfree methods are well suited for parallel processing, since they use a node-by-node algorithm to generate the global system of equations. Hence, in local formulations, the analysis processing can easily be parallelized, in terms of nodes, to set up and solve the global system of equations. Effectively, ILMF is quite suitable for parallel environments, because the respective algorithms associated to each node, are spatially highly localized.

BIBLIOGRAPHIC REFERENCES

Atluri, S.N. and S. Shen (2002). “The Meshless Local Petrov-Galerkin (MLPG) Method: A Simple and Less-costly Alternative to the Finite Element and Boundary Element Methods”. In: *CMES: Computer Modeling in Engineering and Sciences* v.3.n.1, pp. 11–51.

Atluri, S.N. and T. Zhu (1988). “A new Meshless Local Petrov-Galerkin (MLPG) approach in computational mechanics”. In: *Computational Mechanics* v.22.n.2, pp. 117–127.

— (2000). “New Concepts in Meshless Methods”. In: *International Journal for Numerical Methods in Engineering* v.47, pp. 537–556.

Bagheri, A. et al. (2011). “Optimization of meshless local Petrov-Galerkin using genetic algorithm for 3D elasto–static problems”. In: *International Journal of Engineering* 24.2, pp. 143–153.

Baradaran, G.H. and M.J. Mahmoodabadi (2009). “Optimal pareto parametric analysis of two dimensional steady–state heat conduction problems by MLPG method”. In: *International Journal of Engineering* 22.4, pp. 387–406.

Bathe, K.J. (2014). *Finite Element Procedures*. Prentice Hall.

Beissel, S. and T. Belytschko (1996). “Nodal Integration of the Element-Free Galerkin Method”. In: *Computer Methods in Applied Mechanics and Engineering* v.139, pp. 49–74.

Belytschko, T., Y.Y. Lu, and L. Gu (1994). “Element-free Galerkin Methods”. In: *International Journal for Numerical Methods in Engineering* v.37, pp. 229–256.

Belytschko, T. et al. (2000). “A Unified Stability Analysis of Meshless Particle Methods”. In: *International Journal for Numerical Methods in Engineering* v.48, pp. 1359–1400.

Brebbia, C.A. (1985). *Proc. of the II International Conference on Variational Methods in Engineering, C.A. Brebbia and H. Tottenham (Editors), Southampton, 1985, Computational Mechanics Publications*. Berlin: Southampton and Springer Verlag.

Dally, W. J. and F.W. Riley (1991). *Experimental Stress Analysis*. 3rd ed. New Jersey, USA: McGraw-Hill International editions.

Deb, K. (2001). *Multi-Objective Optimization using evolutionary Algorithms*. John Wiley & Sons.

Duarte, C.A. and J.T. Oden (1996). “Hp Clouds–an Hp Meshless Method”. In: *Numerical Methods for Partial Differential Equations* v.12, pp. 673–705.

Eberhart, Russell C. and Y. Shi (2007). *Computational Intelligence: Concepts to Implementations*. Elsevier.

Ebrahimnejad, M., N. Fallah, and A.R. Khoei (2015). “Adaptive refinement in the meshless finite volume method for elasticity problems”. In: *Computers & Mathematics with Applications* 69.12, pp. 1420–1443.

Finalyson, B.A. (1972). *The Method of Weighted Residuals and Variational Principles*. New York: Academic Press.

Gen, M. and R. Cheng (2000). *Genetic Algorithms and Engineering Optimization*. Wiley.

Gingold, R.A. and J.J. Monaghan (1977). “Smoothed Particle Hydrodynamics: Theory and Application to Non-Spherical Stars”. In: *Monthly Notices of the Royal Astronomical Society* v.181, pp. 375–389.

Goldberg, David E and John H Holland (1988). “Genetic algorithms and machine learning”. In: *Machine learning* 3.2, pp. 95–99.

Haftka, T. R. (1990). “Stiffness-Matrix Condition Number and Shape Sensitivity Errors”. In: *AIAA Journal* v.28, pp. 1322–1324.

Haupt, Randy L and Sue Ellen Haupt (2004). *Practical genetic algorithms*. John Wiley & Sons.

Holland, J. H. (1975). *Adaptation in Natural and Artificial Systems*. MIT press.

Hwang, C.-L. and A. S. M. Masud (1979). *Multiple Objectives Decision Making—Methods and Applications*. Springer.

Jamil, M. and E.Y.K. Ng (2013). “Evaluation of Meshless Radial Basis Collocation Method (RBCM) for Heterogeneous Conduction and Simulation of Temperature Inside the Biological Tissues”. In: *International Journal of Thermal Sciences* v.68, pp. 42–52.

Kelner, V. and O. Leonard (2004). “Application of genetic algorithms to lubrication pump stacking design”. In: *Journal of Computational and Applied Mathematics* 168.1, pp. 255–265.

Kirchhoff, G. (1859). “Uber das Gleichgewicht und die Bewegung einer unendlich diinnen elastischen Stabes”. In: *J. Reine Angew. Math.* v.56, pp. 285–313.

Kirkpatrick, S., Gelatt Jr. C. D., and M. P. Vecchi (1983). “Optimization by simulated annealing”. In: *Science* v.220.4598, pp. 671–680.

Lee, S.H. and Y.C. Yoon (2004). “Meshfree Point Collocation Method for Elasticity and Crack Problems”. In: *International Journal for Numerical Methods in Engineering* v.61, pp. 22–48.

Libersky, L.D. et al. (1993). “High Strain Lagrangian Hydrodynamics”. In: *Journal of Computational Physics* v.109, pp. 67–75.

Liu, G.R. (2003). *Mesh Free Methods - Moving beyond the Finite Element Method*. New York, USA: CRC Press.

Liu, G.R. and L. Yan (2000). *A Modified Meshless Local Petrov-Galerkin Method for Solid Mechanics*. Los Angeles: Proceedings of the conference Advances in Computational Engineering and Sciences, pp. 1374–1379.

Liu, G.R. et al. (2001). “Point Interpolation Method Based on Local Residual Formulation Using Radial Basis Functions”. In: *Structural Engineering and Mechanics* v.11.n.2, pp. 221–236.

— (2002a). “Point Interpolation Method Based on Local Residual Formulation Using Radial Basis Functions”. In: *Structural Engineering and Mechanics* v.14, pp. 713–732.

Liu, G.R. et al. (2007). “Integration Technique for Meshfree Radial Point Interpolation Method (NI-RPIM)”. In: *International Journal of Solids and Structures* v.44, pp. 3840–3860.

Liu, W.K., J.S. Ong, and R.A. Uras (1985). “Finite Element Stabilization Matrices - a Unification Approach”. In: *Computer Methods in Applied Mechanics and Engineering* v.53, pp. 13–46.

Liu, W.K., S. Jun, and Y.F. Zhang (1995). “Reproducing Kernel Particle Methods”. In: *International Journal for Numerical Methods in Engineering* v.20, pp. 1081–1186.

Liu, W.K. et al. (1996). “Overview and Applications of the Reproducing Kernel Particle Methods”. In: *Archives of Computational Methods in Engineering State of the Art Reviews* v.3, pp. 3–80.

Liu, X. et al. (2002b). “Radial Basis Point Interpolation Collocation Method For 2D Solid Problem, Proceedings of the 1st Asian Workshop on Meshfree Methods, Edited by G. R. Liu”. In: *World Scientific*, pp. 35–40.

Lucy, L.B. (1977). “A Numerical Approach to the Testing of the Fission Hypothesis”. In: *Astronomical Journal* v.82.n.12, pp. 1013–1024.

McCall, J. (2005). “Genetic algorithms for modelling and optimisation”. In: *Journal of Computational and Applied Mathematics* 184.1, pp. 205–222.

Melenk, J.M. and I. Babuska (1996). “The Partition of Unity Finite Element Method: Basic Theory and Applications”. In: *Computer Methods in Applied Mechanics and Engineering* v.139, pp. 289–314.

Moussaoui, A. and T. Bouziane (2013). “Comparative Study of the Effect of the Parameters of Sizing Data on Results by the Meshless Methods (MLPG)”. In: *World Journal of Mechanics* 3.1, pp. 82–87.

Nayroles, B., G. Touzot, and P. Villon (1992). “Generalizing the Finite Element Method: Diffuse Approximation and Diffuse Elements”. In: *Computational Mechanics* v.10, pp. 307–318.

Oliveira, E.R.A. (1973). *Acidentes Causados pelo Vento*. 4th ed. Lisbon: Editora da UFRGS.

Oliveira, T. and A. Portela (2016). “Weak-form collocation – A local meshless method in linear elasticity”. In: *Engineering Analysis with Boundary Elements* v.73, pp. 144–160.

Oliveira, T. et al. (2019). “A local mesh free method for linear elasticity and fracture mechanics”. In: *Engineering Analysis with Boundary Elements* 101, pp. 221–242.

Onate, E. et al. (1996). “A finite Point Method in Computational Mechanics: Applications to Convective Transport and Fluid Flow”. In: *International Journal for Numerical Methods in Engineering* v.39, pp. 3839–3867.

Onate, E., F. Perazzo, and J. Miquel (2001). “A Finite Point Method for Elasticity Problems”. In: *International Journal for Numerical Methods in Engineering* v.79, pp. 2151–2163.

Parsopoulos, K. E. and M. N. Vrahatis (2002). “Recent approaches to global optimization problems through particle swarm optimization”. In: *Natural Computing* 1235, pp. 671–680.

Portela, A. (1981). “Theoretical Basis of Boundary Solutions for the Linear Theory of Structures”. In: *J. Applied Mathematical Modelling* v.5.n.1, pp. 57–59.

Rao, S. S. (2009). *Engineering Optimization: Theory and Pratice*. John Wiley & Sons.

Ringuest, J. L. (1992). *Multiobjective Optimization: Behavioral and Computational Considerations*. Kluwer.

Sawaragi, Y., H. Nakayama, and T. Tanino (1985). *Theory of Multiobjective Optimization*. Academic Press.

Sekher, K. V. S. and K. G. Vinay (1997). “Higher Modes in Along-Wind Building Response”. In: *Journal of Structural Engineering* v.24.n.3, pp. 181–184.

Steuer, R. E. (1986). *Multiple Criteria Optimization: Theory, Computation, and Application*. Wiley.

Strouboulis, T., K. Copps, and I. Babuska (2000). “The Generalized Finite Element Method: an Example of its Implementation and Illustration of its Performance”. In: *International Journal for Numerical Methods in Engineering* v.47.n.8, pp. 1401–1417.

Swegle, J.W., D.L. Hicks, and S.W. Attaway (1995). “Smoothed Particle Hydrodynamics Stability Analysis”. In: *Journal of Computational Physics* v.116.n.1, pp. 123–134.

Tejani, V. et al. (2016). “Adaptive symbiotic organisms search (SOS) algoritm for structural design optimization”. In: *Journal of Computationa Design and Engineering* v.3, pp. 226–249.

Wu, Z. (1992). “Hermite-Birkhoff Interpolation of Scattered Data by Radial Basis Functions”. In: *Journal of Approximation Theory* v.8, pp. 1–10.

Zhang, X. et al. (2001). “Least-Squares Collocation Meshless Method”. In: *International Journal for Numerical Methods in Engineering* v.51.n.9, pp. 1089–1100.

Zhu, T., J. Zhang, and S.N. Atluri (1998). “A Local Boundary Integral Equation (LBIE) Method in Computational Mechanics and a Meshless Discretization Approach”. In: *Computational Mechanics* v.21, pp. 223–235.

Zienkiewicz, O.C. and R.L. Taylor (1983). *Finite Element and Approximation*. John Wiley.

ANNEXES

A - MLS APPROXIMATION

The moving least squares (MLS) approximation, schematically represented in Figure A.1 for the one-dimensional case, is based on three components which are a weight function of compact support associated with each node, a complete set of polynomial basis functions and a set of coefficients that are function of the space coordinates, as presented by Atluri and Zhu (1988). The basic MLS mesh-free terminology, presented by Atluri and Zhu (2000), is used in this work.

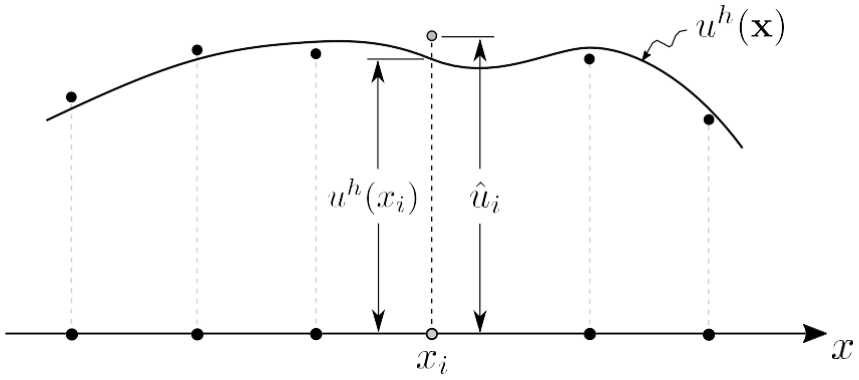

Figure A.1 – Schematic representation of the MLS approximation in one dimension.

Let Ω be the domain of a body with boundary Γ and let $N = \{\mathbf{x}_1, \mathbf{x}_2, \ldots, \mathbf{x}_N\} \in \Omega \cup \Gamma$ be a set of scattered nodal points that represents a mesh-free discretization, as represented in Figure 4.2. Centered at each nodal point $\mathbf{x}_i$, circular or rectangular local compact supports, denoted by Ω_s, can be used whose size, in turn, sets out, in a neighborhood of a sampling point $\mathbf{x}$, the domain of definition $\Omega_{\mathbf{x}}$, of the MLS approximation at this point.

A.1 - SHAPE FUNCTIONS

At a sampling point $\mathbf{x} \in \Omega_{\mathbf{x}}$, the MLS approximation of the displacement $u(\mathbf{x})$, over a number of scattered nodes $\mathbf{x}_i \in \Omega$, $i = 1, 2, \ldots, n$, where the nodal parameters $\hat{u}_i$ are defined, is given by

$$u^h(\mathbf{x}) = \mathbf{p}^T(\mathbf{x})\mathbf{a}(\mathbf{x}), \tag{A.1}$$

in which

$$\mathbf{p}^T(\mathbf{x}) = [p_1(\mathbf{x}), p_2(\mathbf{x}), \ldots, p_m(\mathbf{x})], \tag{A.2}$$

is a vector of the complete monomial basis of order m and $\mathbf{a}(\mathbf{x})$ is the vector of unknown coefficients $a_j(\mathbf{x})$, $j = 1, 2, \ldots, m$ that are functions of the space coordinates $\mathbf{x} = [x_1, x_2]^T$, for

2-D problems.

The coefficient vector $\mathbf{a}(\mathbf{x})$ is determined by minimizing the weighted discrete L_2 norm

$$J(\mathbf{x}) = \frac{1}{2}\sum_{i=1}^{n} w_i(\mathbf{x})\left[u^h(\mathbf{x_i}) - \hat{u}_i\right]^2 = \frac{1}{2}\sum_{i=1}^{n} w_i(\mathbf{x})\left[\mathbf{p}^T(\mathbf{x}_i)\mathbf{a}(\mathbf{x}) - \hat{u}_i\right]^2, \qquad (A.3)$$

with respect to each term of $\mathbf{a}(\mathbf{x})$, in which $w_i(\mathbf{x})$ is the weight function, with compact support, associated with the node $\mathbf{x}_i$ that is $w_i(\mathbf{x}) > 0$, for all $\mathbf{x}$ in the support of $w_i(\mathbf{x})$. The compact support of the MLS weight function is schematically represented in Figure A.2. Finding the extreme of $J(\mathbf{x})$ with respect to each term of $\mathbf{a}(\mathbf{x})$, leads to

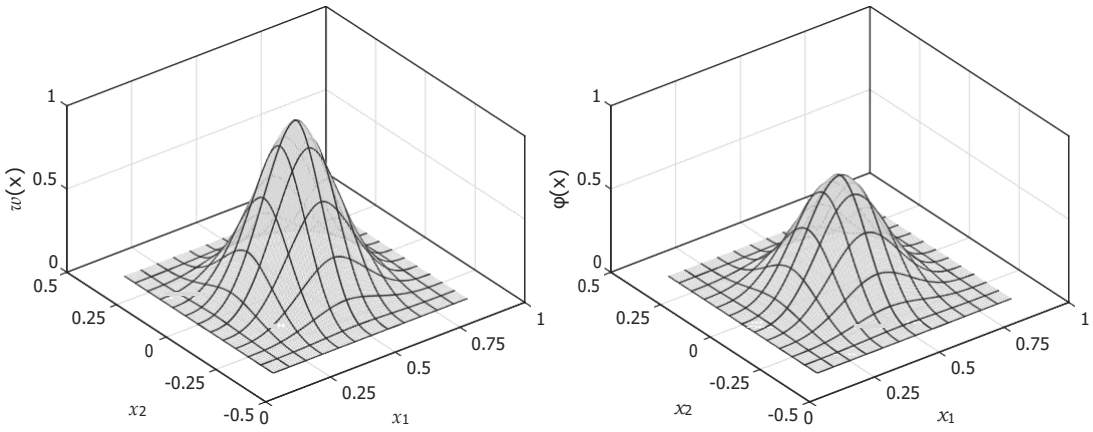

(a) Weight function (b) Shape function

Figure A.2 – Typical weight function and shape function of the MLS approximation for a node at $\mathbf{x} = [1/2\ 0]^T$.

$$\mathbf{A}(\mathbf{x})\mathbf{a}(\mathbf{x}) = \mathbf{B}(\mathbf{x})\hat{\mathbf{u}}, \qquad (A.4)$$

in which

$$\mathbf{A}(\mathbf{x}) = \sum_{i=1}^{n} w_i(\mathbf{x})\mathbf{p}(\mathbf{x}_i)\mathbf{p}^T(\mathbf{x}_i), \qquad (A.5)$$

$$\mathbf{B}(\mathbf{x}) = [w_1(\mathbf{x})\mathbf{p}(\mathbf{x}_1), w_2(\mathbf{x})\mathbf{p}(\mathbf{x}_2), \ldots, w_n(\mathbf{x})\mathbf{p}(\mathbf{x}_n)] \qquad (A.6)$$

and

$$\hat{\mathbf{u}} = [\hat{u}_1, \hat{u}_2, \ldots, \hat{u}_n]. \qquad (A.7)$$

Solving equation (A.4) for $\mathbf{a}(\mathbf{x})$ yields

$$\mathbf{a}(\mathbf{x}) = \mathbf{A}^{-1}(\mathbf{x})\mathbf{B}(\mathbf{x})\hat{\mathbf{u}}, \qquad (A.8)$$

provided $n \geq m$, for each sampling point $\mathbf{x}$, as a necessary condition for a well-defined MLS approximation. Finally, substituting for $\mathbf{a}(\mathbf{x})$ into equation (A.1) leads to the MLS

approximation

$$u^h(\mathbf{x}) = \sum_{i=1} \varphi_i(\mathbf{x}) \hat{u}_i, \tag{A.9}$$

in which

$$\varphi_i(\mathbf{x}) = \sum_{j=1} p_j(\mathbf{x}) \left[\mathbf{A}^{-1}(\mathbf{x})\mathbf{B}(\mathbf{x})\right]_{ji} \tag{A.10}$$

is the shape function of the MLS approximation corresponding to the node $\mathbf{x}_i$, schematically represented in Figure A.2. The MLS shape functions are not nodal interpolants that is $\varphi_i(\mathbf{x}_j) \neq \delta_{ij}$. Since $\varphi_i(\mathbf{x})$ vanishes for $\mathbf{x}$ outside the compact support of the node $\mathbf{x}_i$, the local character of the MLS approximation is preserved. The nodal shape function is complete up to the order of the basis. The smoothness of the nodal shape function is determined by the smoothness of the basis and of the weight function. The spatial derivatives of the shape function $\varphi_i(\mathbf{x})$ are given by

$$\varphi_{i,k} = \sum_{j=1} \left[p_{j,k}(\mathbf{A}^{-1}\mathbf{B})_{ji} + p_j(\mathbf{A}^{-1}\mathbf{B}_{,k} - \mathbf{A}^{-1}\mathbf{A}_{,k}\mathbf{A}^{-1}\mathbf{B})_{ji} \right], \tag{A.11}$$

in which $()_{,k} = \partial()/\partial x_k$.

A.2 - WEIGHT FUNCTIONS

Weight functions $w_i(\mathbf{x})$, introduced in equation (A.3) for each node $\mathbf{x}_i$, have a compact support which defines the subdomain where $w_i(\mathbf{x}) > 0$, for all $\mathbf{x}$. For the sake of simplicity, this paper considers rectangular compact supports with weight functions defined as

$$w_i(\mathbf{x}) = w_{i_x}(\mathbf{x})\, w_{i_y}(\mathbf{x}) \tag{A.12}$$

with the weight function given by the quartic spline function

$$w_{i_x}(\mathbf{x}) = \begin{cases} 1 - 6\left(\dfrac{d_{i_x}}{r_{i_x}}\right)^2 + 8\left(\dfrac{d_{i_x}}{r_{i_x}}\right)^3 - 3\left(\dfrac{d_{i_x}}{r_{i_x}}\right)^4 & \text{for } 0 \le d_{i_x} \le r_{i_x} \\ 0 & \text{for } d_{i_x} > r_{i_x} \end{cases} \tag{A.13}$$

and

$$w_{i_y}(\mathbf{x}) = \begin{cases} 1 - 6\left(\dfrac{d_{i_y}}{r_{i_y}}\right)^2 + 8\left(\dfrac{d_{i_y}}{r_{i_y}}\right)^3 - 3\left(\dfrac{d_{i_y}}{r_{i_y}}\right)^4 & \text{for } 0 \le d_{i_y} \le r_{i_y} \\ 0 & \text{for } d_{i_y} > r_{i_y}, \end{cases} \tag{A.14}$$

in which $d_{i_x} = \|x - x_i\|$ and $d_{i_y} = \|y - y_i\|$. The parameters r_{i_x} and r_{i_y} represent the size of the support for the node i, respectively in the x and y directions.

A.3 - ELASTIC FIELD

The elastic field is now approximated at a sampling point $\mathbf{x}$. Considering equation (A.9), displacement and strain components are respectively approximated as

$$\mathbf{u} = \begin{Bmatrix} u^h(\mathbf{x}) \\ v^h(\mathbf{x}) \end{Bmatrix} = \begin{bmatrix} \varphi_1(\mathbf{x}) & 0 & \dots & \varphi_n(\mathbf{x}) & 0 \\ 0 & \varphi_1(\mathbf{x}) & \dots & 0 & \varphi_n(\mathbf{x}) \end{bmatrix} \begin{Bmatrix} \hat{u}_1 \\ \hat{v}_1 \\ \vdots \\ \hat{u}_n \\ \hat{v}_n \end{Bmatrix} = \boldsymbol{\Phi}\,\hat{\mathbf{u}} \tag{A.15}$$

and

$$\boldsymbol{\varepsilon} = \mathbf{L}\,\mathbf{u} = \mathbf{L}\,\boldsymbol{\Phi}\,\hat{\mathbf{u}} = \mathbf{B}\,\hat{\mathbf{u}}, \tag{A.16}$$

in which geometrical linearity is assumed in the differential operator $\mathbf{L}$ and thus,

$$\mathbf{B} = \begin{bmatrix} \varphi_{1,1} & 0 & \dots & \varphi_{n,1} & 0 \\ 0 & \varphi_{1,2} & \dots & 0 & \varphi_{n,2} \\ \varphi_{1,2} & \varphi_{1,1} & \dots & \varphi_{n,2} & \varphi_{n,1} \end{bmatrix}. \tag{A.17}$$

Stress and traction components are respectively approximated as

$$\boldsymbol{\sigma} = \mathbf{D}\,\boldsymbol{\varepsilon} = \mathbf{D}\,\mathbf{B}\,\hat{\mathbf{u}} \tag{A.18}$$

and

$$\mathbf{t} = \mathbf{n}\,\boldsymbol{\sigma} = \mathbf{n}\,\mathbf{D}\,\mathbf{B}\,\hat{\mathbf{u}}, \tag{A.19}$$

in which $\mathbf{D}$ is the matrix of the elastic constants and $\mathbf{n}$ is the matrix of the components of the unit outward normal, defined as

$$\mathbf{n} = \begin{bmatrix} n_1 & 0 & n_2 \\ 0 & n_2 & n_1 \end{bmatrix}. \tag{A.20}$$

Equations (A.15) to (A.19) show that, at a sampling point $\mathbf{x} \in \Omega_{\mathbf{x}}$, the variables of the elastic field are defined in terms of the nodal unknowns $\hat{\mathbf{u}}$.

B - COMPARISON WITH OTHER NUMERICAL METHODS

The Local Mesh-free Method with reduced integration (ILMF) was comparated to Local Petrov-Galerkin Method (MLPG) and the standard Finite Element Method (FEM) for the four benchmark problems. The simulation with FEM was made the ABAQUS 6.14-4 software, using the CPS8 (8 nodes biquadratic plane stress quadrilateral element) and static analysis by Newton-Rapson method.

B.1 - CANTILEVER BEAM

The comparison for evaluate the accuracy of this three numerical methods (ILMF, MLPG and FEM) in the benchmark test will be made with the discretization shown in Figure B.1.

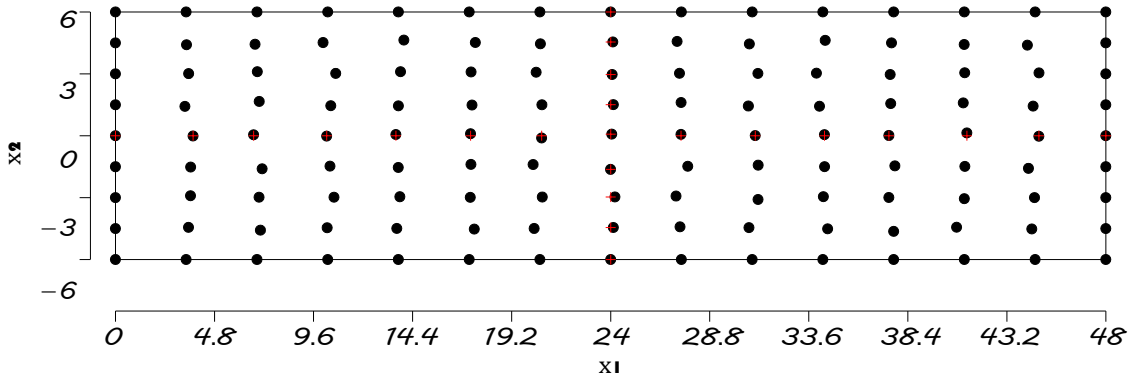

Figure B.1 – Nodal distributions of the cantilever beam, discretization with 15×9 = 135 nodes and level-2 of irregularity; in configuration A.

In Figure B.2 the principal results for the vertical displacement, and stress ($\sigma 11$ and $\sigma 12$) are presented. It can be perceived that there is a good agreement with the analytical resultsa and it is possible to appreciate a better accuracy for the results obtained with ILMF.

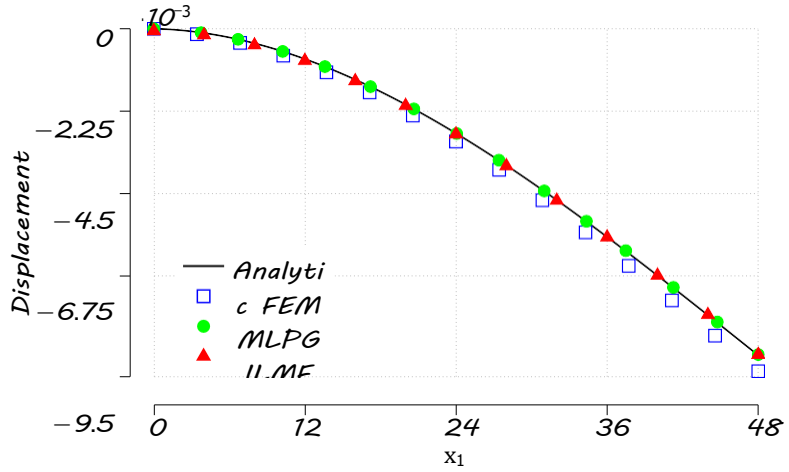

(a) Vertical displacement

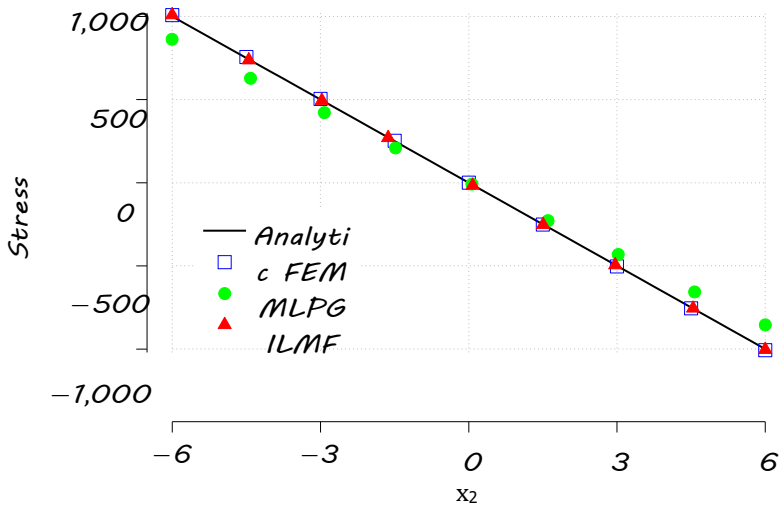

(b) stress ($\sigma 11$)

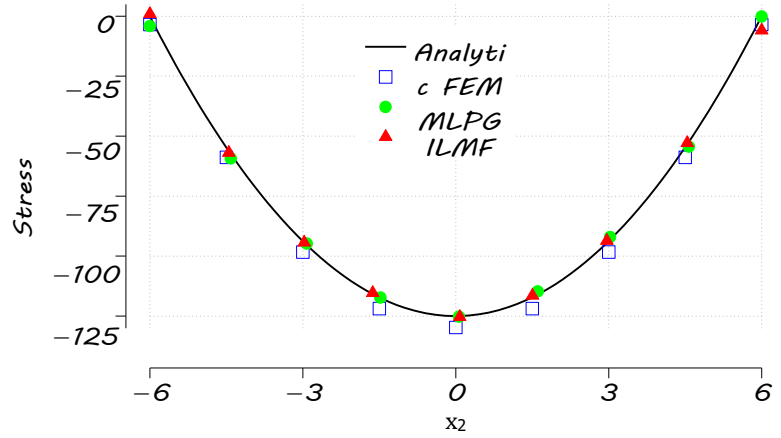

(c) stress ($\sigma 12$)

Figure B.2 – Principal displacement and stress for the cantilever beam with three different numerical methods.

B.2 - CIRCULAR CYLINDER WITH INTERNAL PRESSURE

Figure B.3 shown the discretization for the circular cylinder with internal pressure by evaluate the accuracy of this numerical methods.

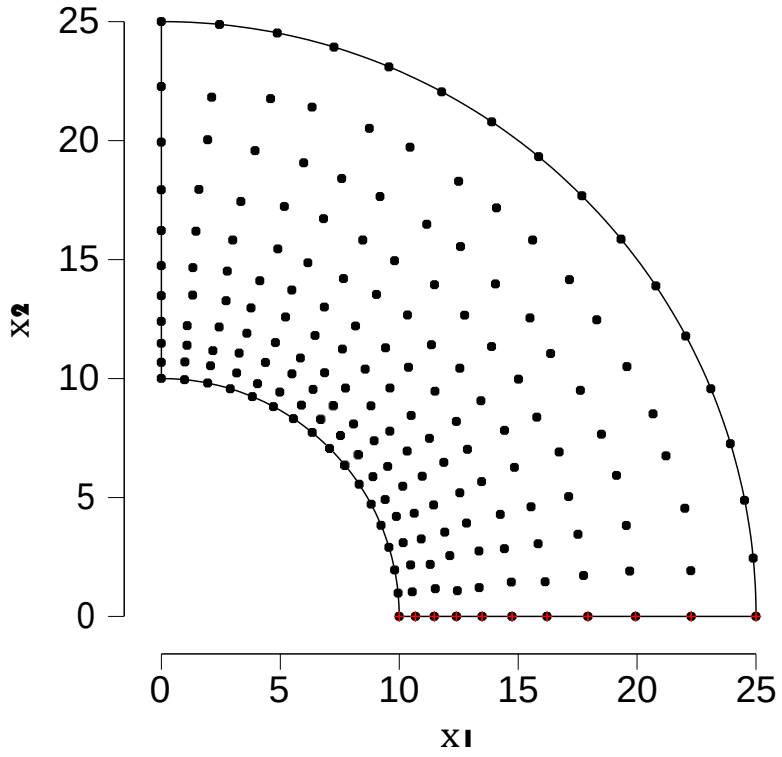

(a) *187* nodes

Figure B.3 – Nodal distributions of the circular cylinder with external pressure, discretization with 17×11 = 187 nodes and level-2 of irregularity; in configuration A.

In Figure B.4 are presented the principal numerical results for the radial displacement and stress in both directions, radial and angular for three discretizations. In addition, it contain its the analytical solution. It can be perceived that there is a good agreement for all methods, in general.

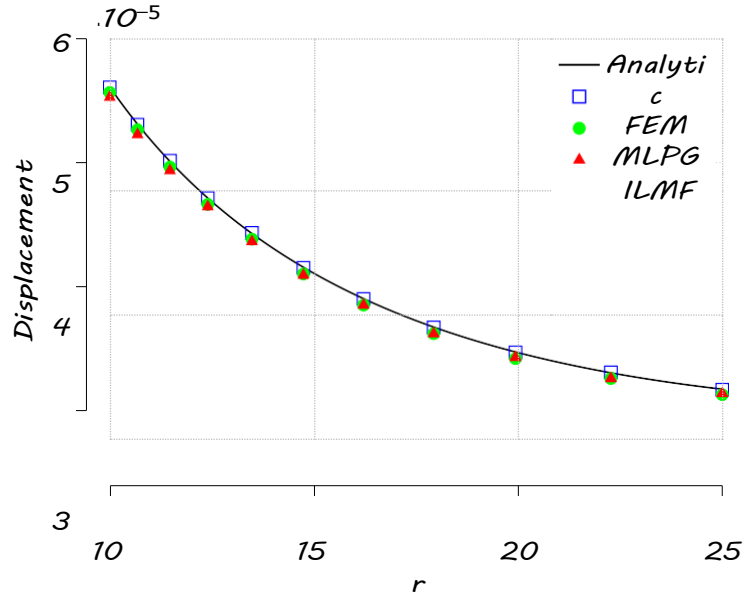

(a) Radial displacement

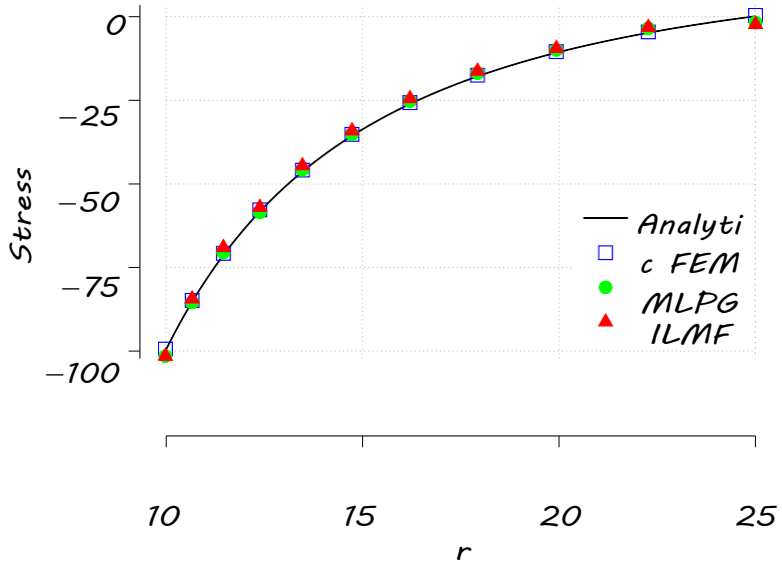

(b) Radial stress

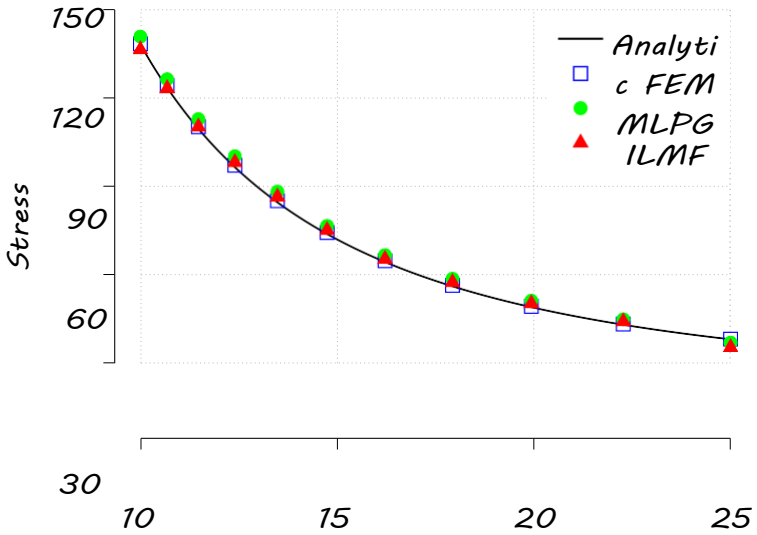

r

(c) Angular stress

Figure B.4 – Principal displacement and stress for the circular cylinder with internal pressure carried out for three different numerical methods.

B.3 - CIRCULAR CYLINDER WITH EXTERNAL PRESSURE

For evaluate the accuracy of the ILMF, MLPG and FEM in the circular cylinder with external pressure will be made the modelation with the discretization shown in Figure B.5.

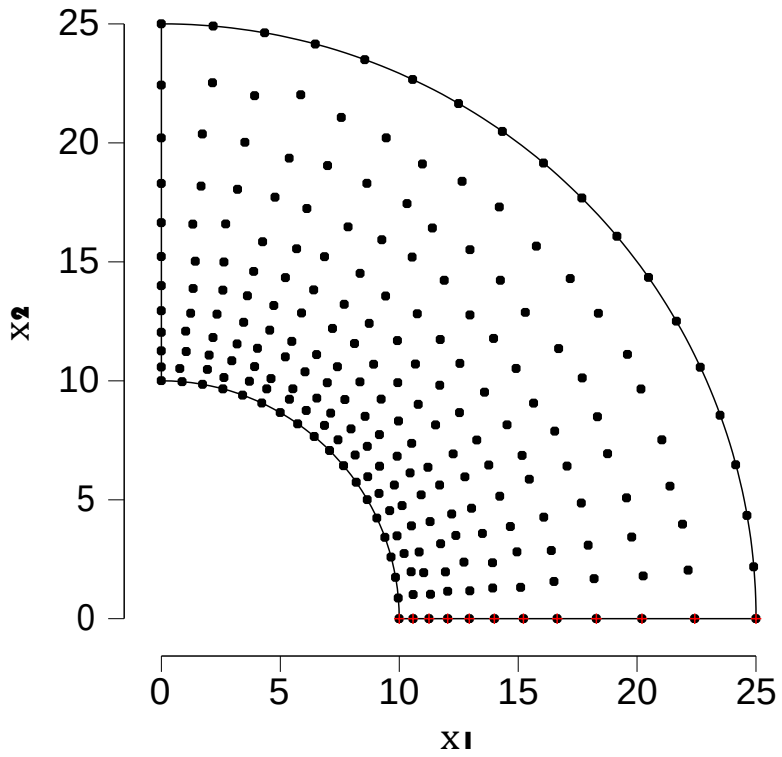

Figure B.5 – Nodal distributions of the circular cylinder with external pressure, discretization with 19×12 = 228 nodes and level-2 of irregularity; in configuration A.

Figure B.6 presented the principal results for the radial displacement, and radial and angular stresses. It can be perceived that there is a good agreement, in general.

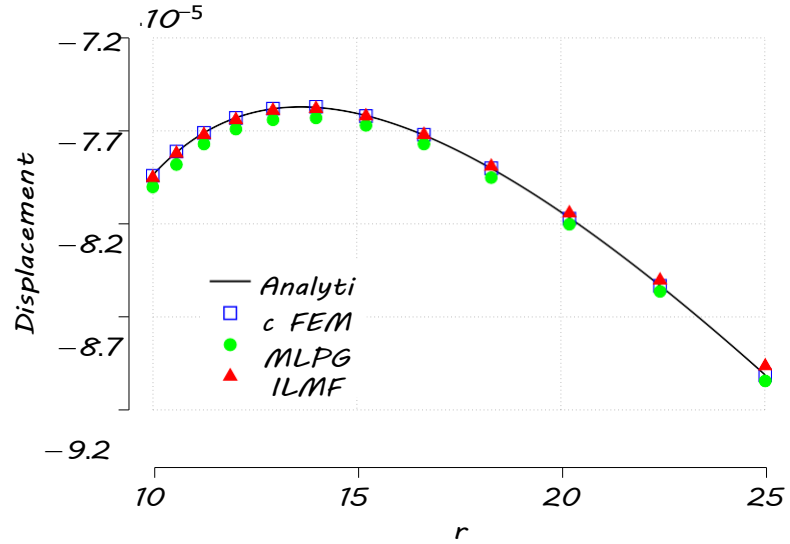

(a) Radial displacement

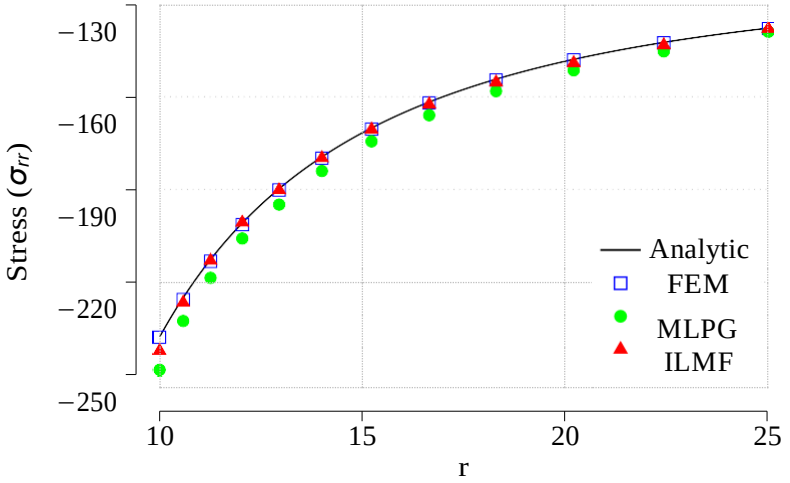

(b) Radial stress

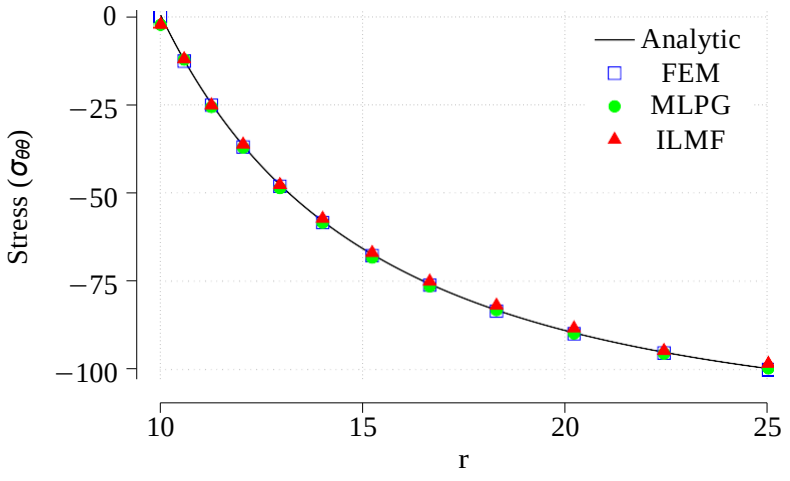

(c) Angular stress

Figure B.6 – Principal displacement and stress for the circular cylinder with external pressure carried out for three different irregular nodal discretization, obtained by the automatic optimization routine.

B.4 - PLATE WITH A CIRCULAR HOLE

The comparison for evaluate the accuracy of this numerical methods in the plate with a circular hole will be made with the discretization shown in Figure B.7.

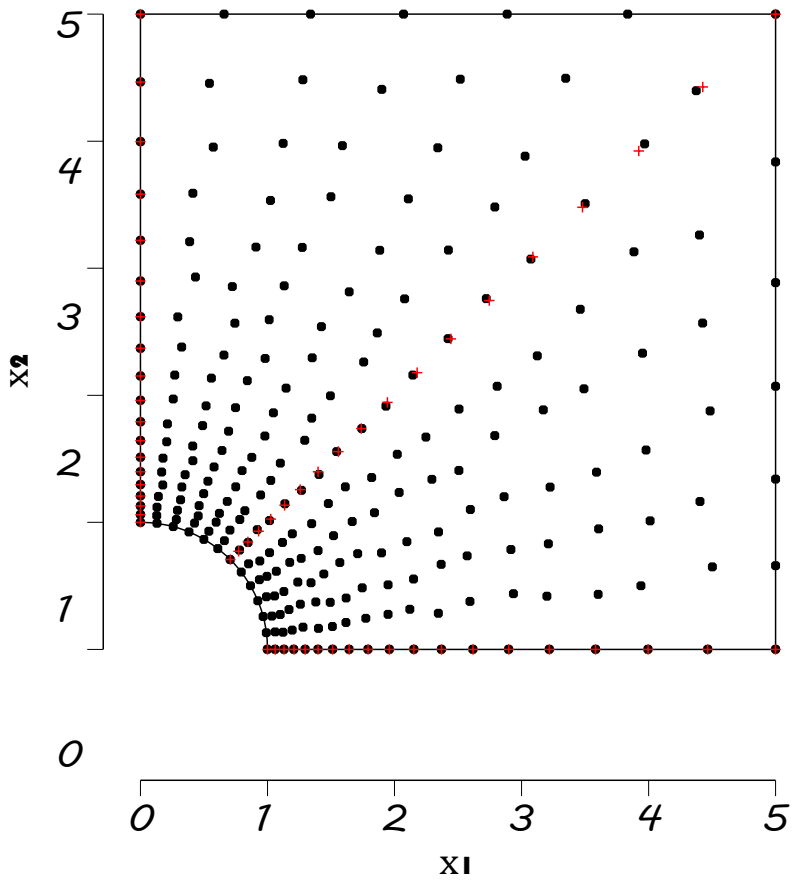

Figure B.7 – Nodal distributions of the plate with a circular hole, discretization 19×13 = 247 nodes and level-2 of irregularity; in configuration A.

In the figure B.8, there are presented the principal results for the displacement in the both directions, horizontal and vertical. All methods presented the same behavior as the analytical solution, however the results for the FEM have a smaller accuracy.

In the figure B.9, there are presented the principal results for the stress in three directions ($\theta = 0, \pi/4, \pi/2$). It can be perceived that there is a good agreement, in general. But, the results for the FEM have a smaller accuracy comparated with other methods.

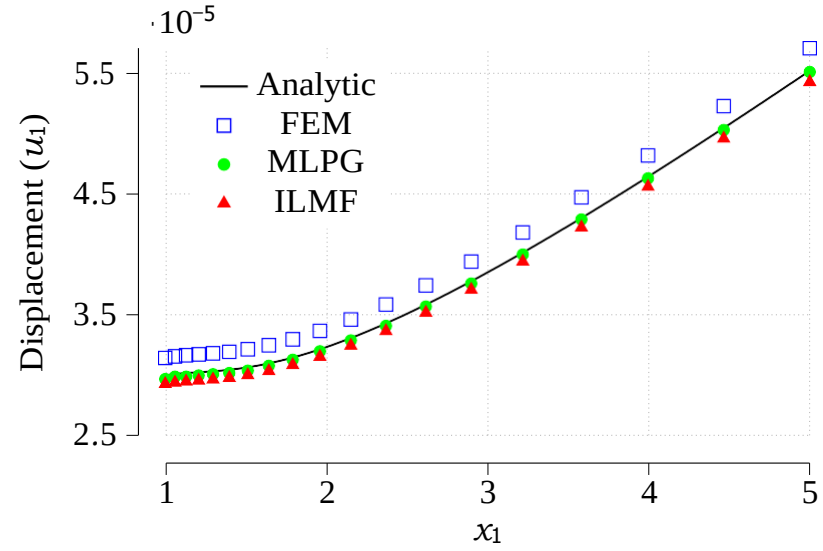

(a) $x_2 = 0$

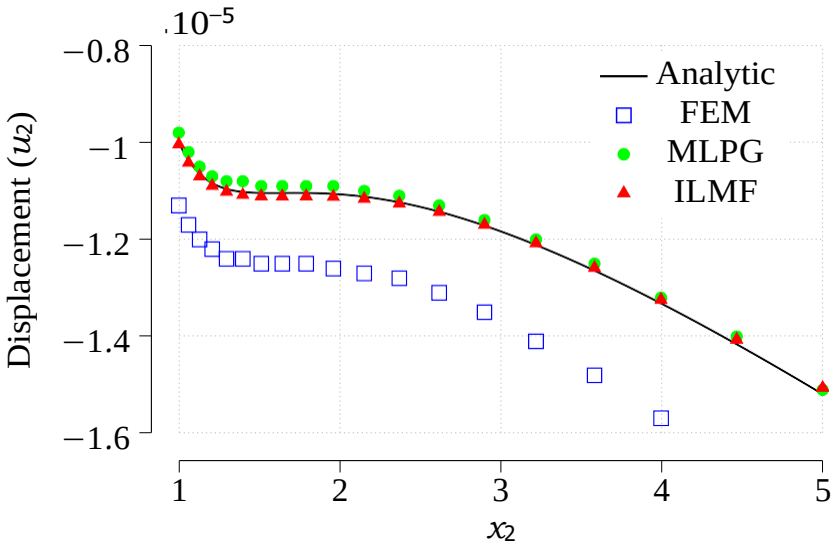

(b) for $x_1 = 0$

Figure B.8 – Horizontal and vertical displacement of the plate with a circular hole, carried out for three different numerical methods.

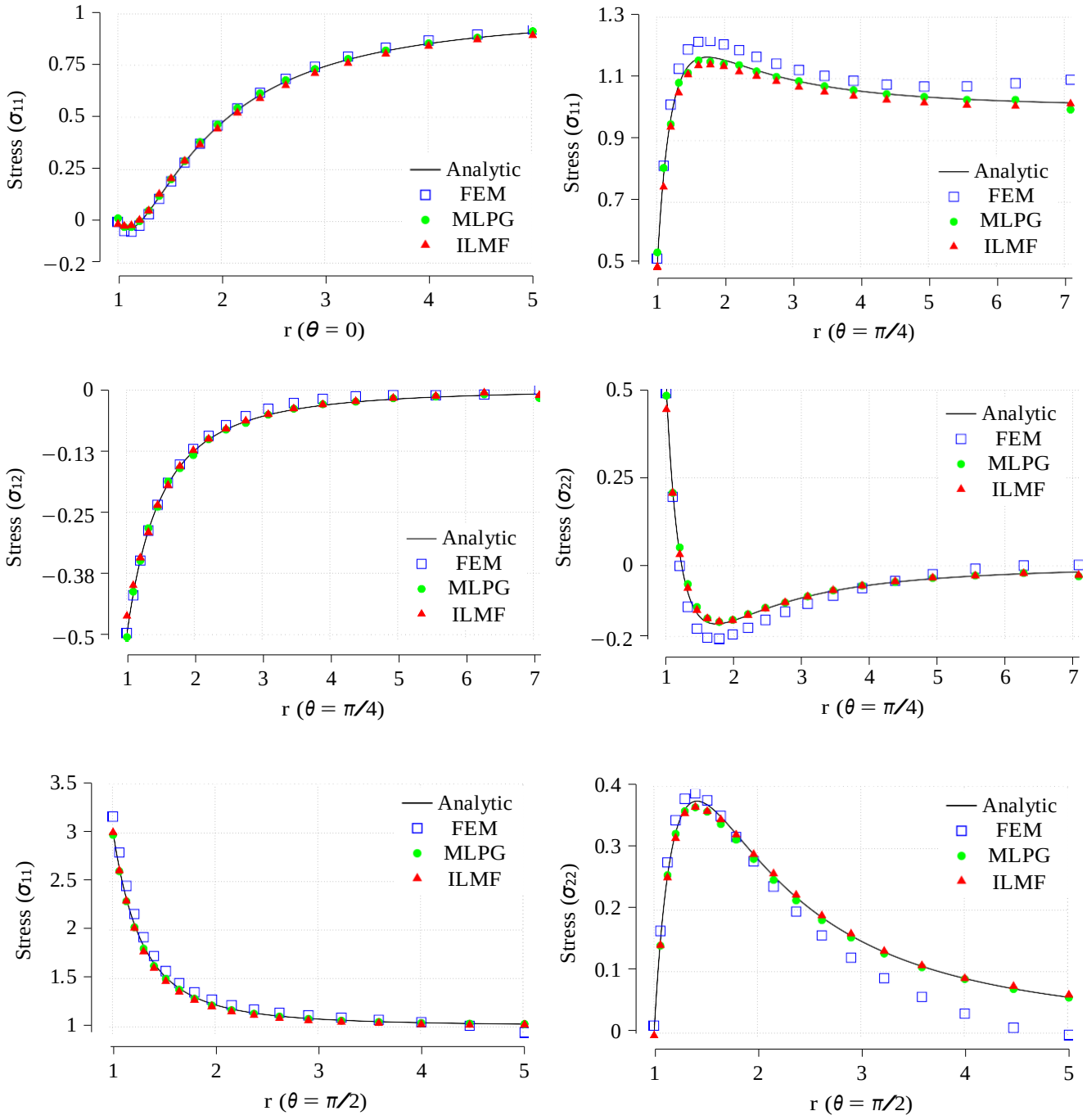

Figure B.9 – Stress distribution of the plate with circular hole for $\theta = 0, \pi/4, \pi/2$, carried out for three different numerical methods.

C - MATLAB

This section contained details about the computational implementation of optimization routine using genetic algorithms of Matlab 2015a software, in this case is applied for determine of discretization parameters of local mesh-free method, the Matlab Optimization Toolbox. In case, of the mono-objective optimization is possible use the platform with graphic interface. All routines were done in a computer with Intel Core I5 vPro, CPU of 2.4 GHz and 4 GB of RAM.

The genetic algorithm can be called by ga function in MATLAB, for mono-objective optimizations, that is, when it has only one objective function, according to the syntax:

$$[x \; fval] = ga(@fitnessfun, nvars, options) \tag{C.1}$$

For multi-objective optimizations, the genetic algorithm can be called by gamultiobj function:

$$[x \; fval] = gamultiobj(@fitnessfun, nvars, options) \tag{C.2}$$

C.1 - SPECIFYING GA OPTIONS

Population size (PopulationSize) specifies how many individuals there are in each generation. With a large population size, the genetic algorithm searches the solution space more thoroughly, thereby reducing the chance that the algorithm returns a local minimum that is not a global minimum. However, a large population size also causes the algorithm to run more slowly. For this modelation the Population size is 200.

Population initial rage (PopInitRange): Specifies the range of vectors in the initial population that is generated.

Generations: Specifies the maximum number of interactions that will be performed by the genetic algorithm. For this work the number of the generation is 7 for the stability.

The hybrid functionality in multi-objective function gamultiobj is slightly different from that of the single objective function GA. In single objective GA the hybrid function starts at the best point returned by GA. However, in gamultiobj the hybrid solver will start at all the points on the Pareto front returned by gamultiobj. The new individuals returned by the hybrid solver are combined with the existing population and a new Pareto front is obtained. It may be useful

to see the syntax of fgoalattain function to better understand how the output from gamultiobj is internally converted to the input of fgoalattain function. gamultiobj estimates the pseudo weights (required input for fgoalattain) for each point on the Pareto front and runs the hybrid solver starting from each point on the Pareto front. Another required input, goal, is a vector specifying the goal for each objective. gamultiobj provides this input as the extreme points from the Pareto front found so far. It is certain that using the hybrid function will result in a optimal Pareto front but we may lose the diversity of the solution (because fgoalattain does not try to preserve the diversity). This can be indicated by a higher value of the average distance measure and the spread of the front. We can further improve the average distance measure of the solutions and the spread of the Pareto front by running gamultiobj again with the final population returned in the last run. Here, the hybrid function is remove.

The Pareto fraction has a default value of 0.35 i.e., the solver will try to limit the number of individuals in the current population that are on the Pareto front to 35 percent of the population size. For this work the Pareto fraction used is 0.43.

Gamultiobj uses three different criteria to determine when to stop the solver. The solver stops when any one of the stopping criteria is met. It stops when the maximum number of generations is reached; by default this number is '200*numberOfVariables'. gamultiobj also stops if the average change in the spread of the Pareto front over the MaxStallGenerations generations (default is 100) is less than tolerance specified in options.FunctionTolerance. The third criterion is the maximum time limit in seconds. Here we modify the stopping criteria to change the FunctionTolerance from 1e-6.

Scaling function (FitnessScalingFcn): Specifies the function responsible for scaling. The default rank function, rank (@fitscalingrank), it is used.

Selection function (SelectionFcn): Specifies how the genetic algorithm chooses parents for the next generation. In this research, @selectiontournament selection is considered.

Parallel processing (UseParallel): Calls the fitness function to be processed in parallel using the pre-established parallel environment in the MATLAB settings.

D - LOCAL MESH-FREE METHOD OPTIMIZATION WITH GENETIC ALGORITMS AND ARTIFICIAL NEURAL NETWORKS

The structure of an ANN is inspired by the structure of the nervous system of the human brain. Its function is based on a pre-defined structure of neurons, which are simple unities where calculations are processed, and the connections between them. A weight is initially attributed to each connection and they are adjusted during training until the output of the ANN is similar to the expected output. The basic ideas and terminology of this optimization are formally defined in.

One of the main characteristics of artificial neural networks is their ability to obtain results in a short time after being trained the network. The optimized data obtained with the genetic algorithms are those used to train the neural network, in this way it is proposed to have more accurate results in a shorter time.

The Figure D.1 show three different nodal arrangement($c_n = 0.1$, $c_n = 0.3$ and $c_n = 0.5$) for a discretization of 55 nodes, were used as an income to train the artificial neural networks. For that, it was utilized eighty one data.

Table D.1 – The multi-objective Pareto front principal results for the circular cylinder with internal pressure, obtained with the automatic optimization routine.

	C_n	a_q	a_s	r_s
ILMF	0.1	0.5013	3.7096	4.21×10^{-3}
MLPG	0.1	0.5140	3.1515	1.30×10^{-4}
ILMF	0.3	0.5001	3.7640	5.03×10^{-3}
MLPG	0.3	0.4668	3.2646	2.49×10^{-3}
ILMF	0.5	0.5016	3.7260	5.96×10^{-3}
MLPG	0.5	0.5117	3.3577	6.12×10^{-3}

Using the optimized with the Genetic Algorithms to train the Artificial Neural Networks to afford to have precise results in a shorter time for the same problem with a new nodal arrangement. This procedure is applicable only for one nodal configuration. However, for a nodal configuration with few nodes, it allows having quite precise solutions, instead of using a greater number of nodes to solve this type of problems as the other methods without optimization.

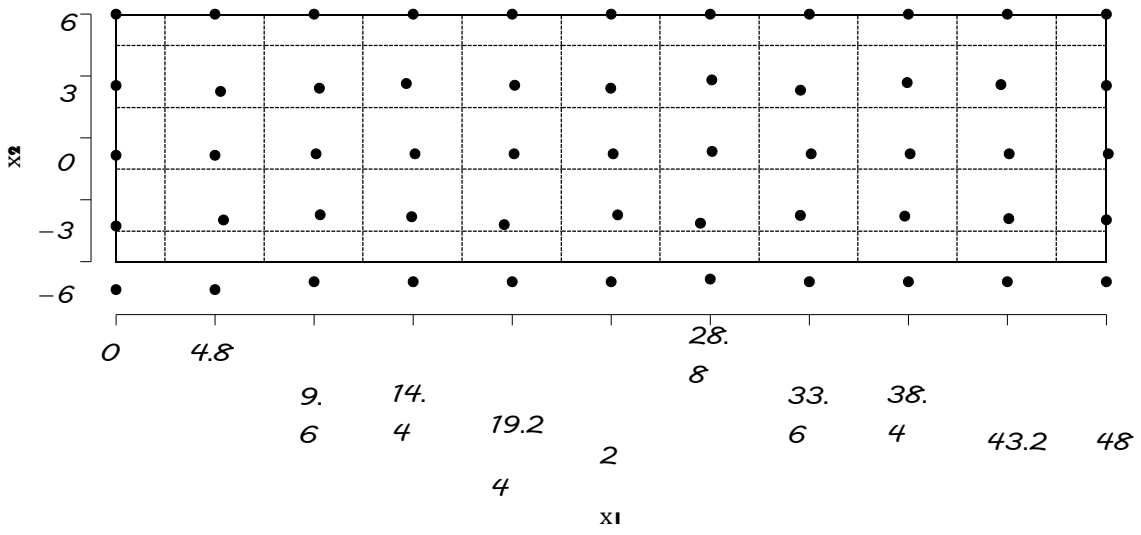

(a) $c_n = 0.0$

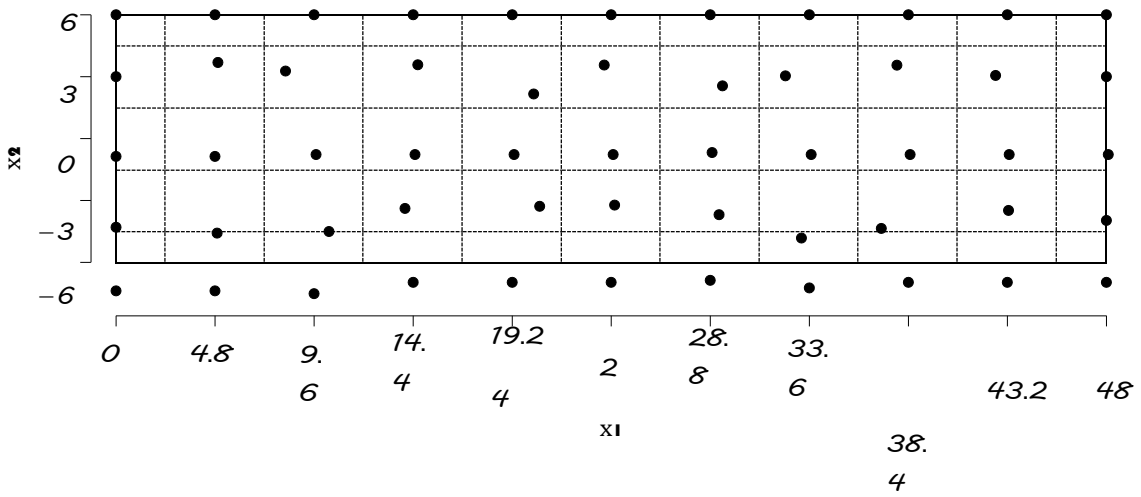

(b) $c_n = 0.4$, configuration A

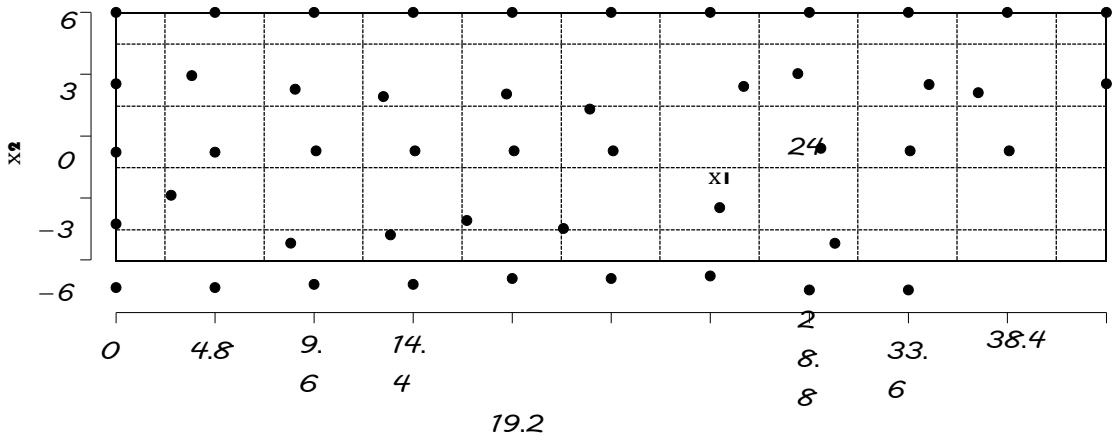

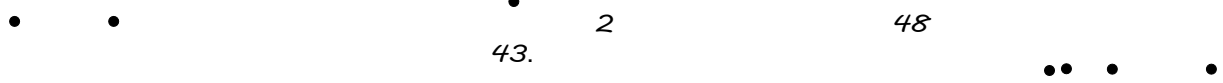

(c) $c_n = 0.4$, configuration B

Figure D.1 – Nodal distributions of the beam discretization with 189 nodes and level-1 of irregularity; in configuration A, only interior nodes have an irregular distribution, as presented by Liu (2003), while in configuration B all nodes are irregularly distributed.

E - PAPERS AND INTERNATIONAL CONFERENCES

E.1 - PAPERS

- A Local Mesh Free Method for Linear Elasticity and Fracture Mechanics.
  Journal name: Engineering Analysis with boundary elements.

  CAPES rating: A1.

  Publication date: April 2019(https://doi.org/10.1016/j.enganabound.2019.01.007)

- Formulation of Local Numerical Methods in Linear Elasticity.

  Journal name: Multidiscipline Modeling in Materials and Structures.

  CAPES rating: B2.

  State: Accepted for publication

- A Local Mesh Free Numerical Method with Automatic Parameter Optimization.
  Journal name: Engineering Analysis with boundary elements.

  CAPES rating: A1.

  Submission date: May 2019

E.2 - INTERNATIONAL CONFERENCES

- Behavior study of the generalized-strain mesh-free method (GSMF)
  Conferences name: The 8th International Conference on Computational Methods (ICCM 2017)

  Place: Guilin, Guangxi, China

  Date: July 2017

- Generalized-Strain - An Efficent Local Meshfree Method in Linear Elasticity
  Conferences name: The 8th International Conference on Computational Methods (ICCM 2017)

  Place: Guilin, Guangxi, China

  Date: July 2017

- Generalized-Strain Mesh-free Method (GSMF) for two-dimensional elasticity problems
  Conferences name: XXXVIII Ibero-Latin American Congress on Computational Methods in Engineering (CILAMCE 2017)

  Place: Florianopolis, Santa Catarina, Brazil

  Date: November 2017

- Meshless Method with reduced integration - high performance

  Conferences name: The 9th International Conference on Computational Methods (ICCM 2018)

  Place: Roma, Italy

  Date: August 2018

- High Performance of the Local Mesh-free Method with Reduced Integration

  Conferences name: 41st International Conference on Boundary Elements and other Mesh Reduction Methods (BEM/MRM 41)

  Place: New Forest, UK

  Date: September 2018

- Local Meshless Method with Reduced Integration for High Irregularity of the Nodal Arrangement

  Conferences name: XXXVIIII Ibero-Latin American Congress on Computational Methods in Engineering (CILAMCE 2018)

  Place: Compiègne, France

  Date: November 2018